



**UNIVERSIDADE ESTADUAL DE CAMPINAS  
INSTITUTO DE QUÍMICA**

**LUÍS ENRIQUE SANTA CRUZ HUAMANÍ**

**WATER SPLITTING-CATALYTIC PERFORMANCE OF RUTHENIUM(II)  
TERPYRIDINE AQUA COMPLEXES CONTAINING HETEROARYL-2-  
IMIDAZOLE LIGANDS**

**DESEMPENHO CATALÍTICO DE AQUA COMPLEXOS TERPIRIDINICOS DE  
RUTÊNIO(II) CONTENDO LIGANTES HETEROARILO-2-IMIDAZÓLICOS NA  
OXIDAÇÃO DA ÁGUA**

**CAMPINAS  
2022**

**LUÍS ENRIQUE SANTA CRUZ HUAMANÍ**

**WATER SPLITTING-CATALYTIC PERFORMANCE OF RUTHENIUM(II)  
TERPYRIDINE AQUA COMPLEXES CONTAINING HETEROARYL-2-IMIDAZOLE  
LIGANDS**

**DESEMPENHO CATALÍTICO DE AQUA COMPLEXOS TERPIRIDINICOS DE  
RUTÊNIO(II) CONTENDO LIGANTES HETEROARILO-2-IMIDAZÓLICOS NA  
OXIDAÇÃO DA ÁGUA**

Tese de Doutorado apresentada ao Instituto de Química da Universidade Estadual de Campinas como parte dos requisitos exigidos para a obtenção de título de Doutor em Ciências.

Doctor's Thesis presented to the Institute of Chemistry of the University of Campinas as part of the requirements to obtain the title of Doctor in Sciences.

**Supervisor: Dr. André Luiz Barboza Formiga**

**O arquivo digital corresponde à versão final da Tese defendida pelo aluno Luís Enrique Santa Cruz Huamaní e orientada pelo Prof. Dr. André Luiz Barboza Formiga.**

**CAMPINAS  
2022**

Ficha catalográfica  
Universidade Estadual de Campinas  
Biblioteca do Instituto de Química  
Simone Luiz Alves - CRB 8/9094

H86w Huamaní, Luís Enrique Santa Cruz, 1989-  
Water splitting-catalytic performance of ruthenium(II) terpyridine aqua complexes containing heteroaryl-2-imidazole ligands / Luís Enrique Santa Cruz Huamaní. – Campinas, SP : [s.n.], 2022.

Orientador: André Luiz Barboza Formiga.  
Tese (doutorado) – Universidade Estadual de Campinas, Instituto de Química.

1. Água - oxidação. 2. Catalisadores de rutênio. 3. Imidazóis. 4. Diagramas de Pourbaix. I. Formiga, André Luiz Barboza, 1978-. II. Universidade Estadual de Campinas. Instituto de Química. III. Título.

Informações Complementares

**Título em outro idioma:** Desempenho catalítico de aqua complexos terpiridínicos de rutênio(II) contendo ligantes heteroarilo-2-imidazólicos na oxidação da água

**Palavras-chave em inglês:**

Water oxidation

Ruthenium catalysts

Imidazoles

Pourbaix diagrams

**Área de concentração:** Química Inorgânica

**Titulação:** Doutor em Ciências

**Banca examinadora:**

André Luiz Barboza Formiga [Orientador]

Pedro Paulo Corbi

Raphael Nagao de Sousa

Izilda Aparecida Bagatin

André Sarto Polo

**Data de defesa:** 15-08-2022

**Programa de Pós-Graduação:** Química

**Identificação e informações acadêmicas do(a) aluno(a)**

- ORCID do autor: <https://orcid.org/0000-0002-8342-9069>

- Currículo Lattes do autor: <http://lattes.cnpq.br/1818250162353119>

## **BANCA EXAMINADORA**

Prof. Dr. André Luiz Barboza Formiga (Orientador)

Prof. Dr. Pedro Paulo Corbi (Universidade Estadual de Campinas)

Prof. Dr. Raphael Nagao de Sousa (Universidade Estadual de Campinas)

Profa. Dra. Izilda Aparecida Bagatin (Universidade Federal de São Paulo)

Prof. Dr. André Sarto Polo (Universidade Federal do ABC)

A ata da defesa assinada pelos membros da Comissão Examinadora, consta no SIGA/Sistema de Fluxo de Dissertação/Tese e na Secretaria do Programa da Unidade.

Este exemplar corresponde à redação final da Tese de Doutorado defendida pelo aluno **Luís Enrique Santa Cruz Huamaní**, aprovada pela Comissão Julgadora em 15 de agosto de 2022.

## **Acknowledgment**

Agradeço aos meus pais Santos Santa Cruz e Fortunata Huamaní pelo amor e suporte nos momentos difíceis, pelas palavras de apoio e conforto, pela confiança depositada em mim e, acima de tudo, pelo valioso esforço que realizaram para poder me ajudar nessa longa jornada de me tornar um profissional.

Ao meu irmão pelo carinho e apoio incondicional em todo momento.

A minha noiva Aline, pelo amor incondicional o tempo todo, pela companhia nos momentos tristes e alegres que foram cruciais para continuar firme nessa longa e sinuosa maratona, pela paciência e bom humor que tornam meus dias mais leves, pela sabedoria que me ajudaram a me tornar uma melhor pessoa.

Aos meus amigos e colegas do laboratório que sempre mantiveram um ambiente leve e agradável, muito obrigado por terem me acolhido. Ao Renan Guerra pela amizade, pelo incentivo, pelas dicas dentro e fora do laboratório, pela imensa parceria. À Naheed Bibi, uma excelente pessoa e uma bondade fora do comum, tornando nossos dias mais leves. À Júlia pela enorme ajuda e paciência em encarar as temidas cromatografias em coluna. Ao Gabriel por ter nos ajudado com os dados computacionais. Ao Marcos, Kalil, Vera, Pãmyla, Bruno, Douglas, Raphael, Carlos, Anna Karla, Julia, Crislaine, Juan, Marcelo, Marcus e Willian, muito obrigado pela valiosa parceria e colaboração.

Ao Professor André Formiga pela oportunidade de trabalhar em seu grupo de pesquisa, pela orientação, pelo conhecimento brindado, pelas excelentes aulas que presenciei, fatores que me tornaram um melhor profissional.

Aos Professores Juliano Bonacin, Pedro Corbi e Diego Pereira pelas valiosas dicas, palavras e aulas que levarei sempre comigo.

Agradeço ao Conselho Nacional de Desenvolvimento Científico e Tecnológico (CNPq), processo nº 142386/2016-2, pela bolsa concedida.

O presente trabalho foi realizado com apoio da Coordenação de Aperfeiçoamento de Pessoal de Nível Superior - Brasil (CAPES) - Código de Financiamento 001.

Agradeço à FAPESP (processo nº 2013/22127/2, Fundação de Amparo à Pesquisa do Estado de São Paulo – FAPESP) pelo auxílio financeiro.

## Resumo

Este projeto visa avaliar o desempenho catalítico de aqua complexos N-heterocíclicos de rutênio (II) para a oxidação da água, que é uma fonte alternativa de energia limpa e de baixo custo comparada aos atuais combustíveis fósseis poluentes fornecendo um combustível verde (H<sub>2</sub>) usando energia solar. Os aqua complexos polipiridínicos de rutênio (II) têm sido estudados para este fim porque participam de processos de transferência de prótons e elétrons, que são inerentes à oxidação da água, e são capazes de atingir altos estados de oxidação produzindo espécies altamente eletrofílicas propensas a reagir com uma molécula de água. Especificamente, quatro complexos de rutênio (II), [Ru(OH<sub>2</sub>)(Himpy)(tpy)]<sup>2+</sup>, [Ru(OH<sub>2</sub>)(Himpa)(tpy)]<sup>2+</sup>, [Ru(OH<sub>2</sub>)(Himpm)(tpy)]<sup>2+</sup> e [Ru(OH<sub>2</sub>)(Himpz)(tpy)]<sup>2+</sup>, contendo os ligantes heteroaril-2-imidazol que possuem propriedades eletrônicas doadoras σ-π, bem como um potencial redox dependente do próton ionizável do imidazol, foram avaliados. A rota sintética para a obtenção desses complexos iniciou-se com a síntese do complexo [Ru(tpy)Cl<sub>3</sub>] seguida de uma reação com o ligante heteroaril-2-imidazol para obtenção dos complexos [Ru(Cl)(Himp<sub>x</sub>)(tpy)]<sup>+</sup>. Finalmente, um composto de prata foi usado para remover o ligante cloreto e obter os aqua complexos de rutênio (II). Os quatro complexos foram bem caracterizados por meio de análise elementar, espectrometria de massas, espectroscopia <sup>1</sup>H-RMN e suas estruturas resolvidas por cristalografia de raios X. Os diagramas de Pourbaix dos aqua complexos foram obtidos a partir de medições eletroquímicas e usados para estudar suas propriedades eletrônicas em diferentes pH. Foram obtidos altos estados de oxidação em potenciais baixos à medida que o pH aumentava, diretamente influenciados pela capacidade doadora dos ligantes heteroaril-2-imidazol, o que por sua vez gerou um bom desempenho na oxidação catalítica da água. Além disso, foram realizados estudos cinéticos com os aqua complexos de rutênio (II) para desvendar um possível mecanismo para a oxidação da água.

## Abstract

This Thesis aims to assess the catalytic performance of ruthenium (II) N-heterocyclic aqua-complexes for water oxidation, which is a clean, low-cost energy source alternative to current pollutant fossil fuels providing a green fuel (H<sub>2</sub>) using solar energy. The ruthenium (II) polypyridine aqua-complexes have been studied for this purpose because they participate in proton-electron transfer processes, which are inherent in water oxidation, and achieve high oxidation states allowing them to be great electrophilic species which will further react with water molecules. Specifically, four ruthenium (II) complexes, [Ru(OH<sub>2</sub>)(Himpy)(tpy)]<sup>2+</sup>, [Ru(OH<sub>2</sub>)(Himpa)(tpy)]<sup>2+</sup>, [Ru(OH<sub>2</sub>)(Himpm)(tpy)]<sup>2+</sup> and [Ru(OH<sub>2</sub>)(Himpz)(tpy)]<sup>2+</sup>, containing the heteroaryl-2-imidazole ligands that have interesting  $\sigma$ - $\pi$  donor electronic properties as well as a ionizable imidazole proton-dependent redox potential, were evaluated. The synthetic route for obtaining these complexes started with the synthesis of the [Ru(tpy)Cl<sub>3</sub>] complex followed by a reaction with the heteroaryl-2-imidazole ligand to obtain the [Ru(Cl)(Himp<sub>x</sub>)(tpy)]<sup>+</sup> complexes. Finally, a silver compound was used to remove the chlorido ligand and obtain the ruthenium (II) aqua-complexes. The four complexes were well characterized by means of elemental analysis, mass spectrometry, <sup>1</sup>H-NMR spectroscopy and their structures solved by X-ray crystallography. The Pourbaix diagrams of the aqua complexes were obtained from electrochemical measurements and used to study their electronic properties in different pH media. High oxidation states were obtained at lower potentials as the pH medium increases, directly influenced by the donor capacity of the heteroaryl-2-imidazole ligands, which in turn generated a good performance in the catalytic water oxidation. Furthermore, kinetic studies on the ruthenium (II) aqua complexes were carried out to unravel a possible mechanism of water oxidation.

## List of Figures

<b>Figure 1.</b>	Cyclic voltammograms of Himpx ligands (2 mM) recorded in acetonitrile containing 0.1 M TBAPF6 under N2. Scan rate: 0.1 V s <sup>-1</sup> . (a) Himpy, (b) Himpm, (c) Himpa, (d) Himpz. ....	28
<b>Figure 2.</b>	Cyclic voltammograms and differential pulse voltammograms of the Himpy ligand (2 mM) in different pH media. 0.04 M Britton–Robinson buffer and 0.1 M KNO3 were used as the supporting electrolyte.....	30
<b>Figure 3.</b>	(a) Unsuccessful attempt to obtain one isomer exclusively. (b) TLC plates performed on the reaction products showing the formation of more than one compound. (c) Possible fast-running compound appearing in all reaction synthesis.....	37
<b>Figure 4.</b>	UV-visible spectra of Ru(tpy)Cl <sub>3</sub> and the unknown product in acetonitrile. ....	38
<b>Figure 5.</b>	<sup>1</sup> H-NMR spectrum of the unknown compound in DMSO-d <sub>6</sub> at 400 MHz. ....	39
<b>Figure 6.</b>	ORTEP diagram of the unknown compound at 150 K. The numbering is different from that used for <sup>1</sup> H-NMR assignments (next sections). Atoms are colored as follows: Carbon (soft gray), nitrogen (blue), hydrogen (white), oxygen (red), ruthenium (teal), chlorine (green).....	40
<b>Figure 7.</b>	(a) TLC plates showing the cis and trans isomers. (b) Column chromatography performed on the reaction products. (c) The cis and trans isomers isolated after performing column chromatography. ....	41
<b>Figure 8.</b>	<sup>1</sup> H-NMR spectra of (a) cis-[Ru <sup>II</sup> (Himpy)(tpy)(Cl)] <sup>+</sup> and (b) trans-[Ru <sup>II</sup> (Himpy)(tpy)(Cl)] <sup>+</sup> complexes recorded in CD <sub>3</sub> OD at 250 MHz.....	43
<b>Figure 9.</b>	<sup>1</sup> H-NMR spectra of (a) cis-[Ru <sup>II</sup> (Himpz)(tpy)(Cl)] <sup>+</sup> and (b) trans-[Ru <sup>II</sup> (Himpz)(tpy)(Cl)] <sup>+</sup> complexes recorded in DMSO-d <sub>6</sub> at 250 MHz. ....	45
<b>Figure 10.</b>	ORTEP view of the X-ray structure of cis-[Ru <sup>II</sup> (Himpy)(tpy)(Cl)](PF <sub>6</sub> )·H <sub>2</sub> O at 150K. Atoms are colored as follows: Carbon (gray), nitrogen (blue), hydrogen (soft gray), oxygen (red), ruthenium (teal), phosphorous (orange), chlorine (green), fluorine (yellow). ....	47
<b>Figure 11.</b>	ORTEP view of the X-ray structure of trans-[Ru <sup>II</sup> (Himpy)(tpy)(Cl)](PF <sub>6</sub> )·CHCl <sub>3</sub> at 150K. Atoms are colored as follows: Carbon (gray), nitrogen (blue), hydrogen (soft gray), ruthenium (teal), phosphorous (orange), chlorine (green), fluorine (yellow). ....	48
<b>Figure 12.</b>	UV-visible spectra of ruthenium(II) chlorido complexes in ethanol. ....	50
<b>Figure 13.</b>	MLCT region of the UV-visible spectra for [Ru <sup>II</sup> (Himpy)(tpy)(Cl)] <sup>+</sup> and [Ru <sup>II</sup> (Himpa)(tpy)(Cl)] <sup>+</sup> complexes in ethanol. The inset figure shows the energy transitions and the correlation with the ligands' reduction potentials. ....	51
<b>Figure 14.</b>	UV-visible spectra of cis- and trans-[Ru <sup>II</sup> (Himpy)(tpy)(Cl)] <sup>+</sup> complexes in ethanol. ....	52
<b>Figure 15.</b>	Absorption bands changes of cis-[Ru <sup>II</sup> (Himpy)(tpy)(Cl)] <sup>+</sup> (50 μM) in 0.04 M Britton–Robinson buffer after titrating with 4 M NaOH solution in pH range from 1.9 to 10.03. Inset: Plot of absorbances at 467 and 511 nm versus pH. ....	53

<b>Figure 16.</b> Dinuclear <b>(a)</b> “Blue dimer” <i>cis,cis</i> -[(bpy) <sub>2</sub> (OH <sub>2</sub> )RuORu(OH <sub>2</sub> )(bpy) <sub>2</sub> ] <sup>4+</sup> complex and <b>(b)</b> Ruthenium complex containing the 3,6-bis-[6'-(1'',8''-naphthyrid-2''-yl)-pyrid-2'-yl]pyridazine ligand. Adapted from Meyer <i>et al.</i> <sup>68</sup> and Thummel <i>et al.</i> , <sup>69</sup> respectively. ....	56
<b>Figure 17.</b> Mononuclear <b>(a)</b> [Ru <sup>II</sup> (bpm)(tpy)(OH <sub>2</sub> )] <sup>2+</sup> and [Ru <sup>II</sup> (bpz)(tpy)(OH <sub>2</sub> )] <sup>2+</sup> and <b>(b)</b> [Ru <sup>II</sup> (bpy)(tpy)(Cl)] <sup>+</sup> and [Ru <sup>II</sup> (bpy)(tpy)(OH <sub>2</sub> )] <sup>2+</sup> complexes. Adapted from Meyer <i>et al.</i> <sup>72</sup> and Sakai <i>et al.</i> , <sup>44</sup> respectively. ....	57
<b>Figure 18.</b> <sup>1</sup> H-NMR spectra of (a) [Ru <sup>II</sup> (Himpy)(tpy)(Cl)] <sup>+</sup> and (b) [Ru <sup>II</sup> (Himpy)(tpy)(OH <sub>2</sub> )] <sup>2+</sup> complexes recorded in DMSO-d <sub>6</sub> at 400 MHz. ....	65
<b>Figure 19.</b> <sup>1</sup> H-NMR spectra of fresh <i>cis</i> -[Ru <sup>II</sup> (Himpz)(tpy)(Cl)] <sup>+</sup> (black) and <i>cis</i> -[Ru <sup>II</sup> (Himpz)(tpy)(OH <sub>2</sub> )] <sup>2+</sup> (red) solutions, and the same aqua complex solution after standing one week (blue), all of them recorded in DMSO-d <sub>6</sub> at 500 MHz. ....	67
<b>Figure 20.</b> <sup>1</sup> H-NMR spectra of fresh <i>cis</i> -[Ru <sup>II</sup> (Himpm)(tpy)(Cl)] <sup>+</sup> solution (black) and the same solution after one week (red) recorded in DMSO-d <sub>6</sub> at 500 MHz. ....	67
<b>Figure 21.</b> <sup>1</sup> H-NMR spectra of (a) [Ru <sup>II</sup> (Himpa)(tpy)(Cl)] <sup>+</sup> and (b) [Ru <sup>II</sup> (Himpa)(tpy)(OH <sub>2</sub> )] <sup>2+</sup> complexes recorded in DMSO-d <sub>6</sub> at 400 MHz. ....	68
<b>Figure 22.</b> ORTEP view of the X-ray structure of <i>cis</i> -[Ru <sup>II</sup> (Himpy)(tpy)(OH <sub>2</sub> )](ClO <sub>4</sub> ) <sub>2</sub> and <i>trans</i> -[Ru <sup>II</sup> (Himpy)(tpy)(OH <sub>2</sub> )](PF <sub>6</sub> ) <sub>2</sub> at 150K. Atoms are colored as follows: Carbon (gray), nitrogen (blue), hydrogen (soft gray), oxygen (red), ruthenium (teal), phosphorous (orange), chlorine (green), fluorine (yellow). ....	71
<b>Figure 23.</b> UV-visible spectra of ruthenium(II) aqua complexes in water. ....	73
<b>Figure 24.</b> UV-visible spectra of [Ru <sup>II</sup> (Himpm)(tpy)(Cl)] <sup>+</sup> (black) and [Ru <sup>II</sup> (Himpm)(tpy)(OH <sub>2</sub> )] <sup>2+</sup> (blue) in water. ....	74
<b>Figure 25.</b> (a) Absorption bands changes of [Ru <sup>II</sup> (Himpy)(tpy)(OH <sub>2</sub> )] <sup>2+</sup> (160 μM) in 0.04 M Britton–Robinson buffer after titrating with 4 M NaOH solution in pH range from 4.4 to 11.94. Inset: Isosbestic points indicating protonated and deprotonated species in equilibrium along pH range. (b) Plot of absorbances at 405 and 500 nm versus pH. ....	75
<b>Figure 26.</b> Cyclic voltammograms displaying the better performance of the aqua complex (red) over the chlorido complex (blue) at pH 8. Blank cyclic voltammogram is also displayed (black). Scan rate: 0.1 V s <sup>-1</sup> . Inset plot: DPV showing the Ru <sup>II</sup> /Ru <sup>III</sup> redox potential for both complexes. ....	76
<b>Figure 27.</b> Cyclic voltammograms of [Ru <sup>II</sup> (Himpy)(tpy)(OH <sub>2</sub> )] <sup>2+</sup> (red) and [Ru <sup>II</sup> (Himpa)(tpy)(OH <sub>2</sub> )] <sup>2+</sup> (blue) at pH 8. Blank current was subtracted for both complexes. Dashed lines indicate the onset potential for water oxidation. Inset plot: DPV showing the Ru <sup>II</sup> /Ru <sup>III</sup> redox potential for both complexes. Scan rate 0.1 V s <sup>-1</sup> . ....	77
<b>Figure 28.</b> DPV of [Ru <sup>II</sup> (Himpy)(tpy)(OH <sub>2</sub> )] <sup>2+</sup> (black) and [Ru <sup>II</sup> (Himpa)(tpy)(OH <sub>2</sub> )] <sup>2+</sup> (red), and SWV of [Ru <sup>II</sup> (Himpm)(tpy)(OH <sub>2</sub> )] <sup>2+</sup> (blue) and [Ru <sup>II</sup> (Himpz)(tpy)(OH <sub>2</sub> )] <sup>2+</sup> (pink) at pH 2–10. Electrolyte: 0.04 M Britton–Robinson + 0.1 M KNO <sub>3</sub> . WE: GCE. RE: SCE. CE: Pt. ....	79
<b>Figure 29.</b> Pourbaix diagram of <b>(1)</b> (1 mM) in 0.04 M Britton–Robinson buffer + 0.1 M KNO <sub>3</sub> solution. ....	81

<b>Figure 30.</b> Pourbaix diagram of <b>(2)</b> (1 mM) in 0.04 M Britton–Robinson buffer + 0.1 M KNO <sub>3</sub> solution. ....	82
<b>Figure 31.</b> Pourbaix diagram of <b>(3)</b> (1 mM) in 0.04 M Britton–Robinson buffer + 0.1 M KNO <sub>3</sub> solution. ....	82
<b>Figure 32.</b> Pourbaix diagram of <b>(4)</b> (1 mM) in 0.04 M Britton–Robinson buffer + 0.1 M KNO <sub>3</sub> solution. ....	84
<b>Figure 33.</b> Pourbaix diagrams of [Ru <sup>II</sup> (Himpy)(tpy)(OH <sub>2</sub> )] <sup>2+</sup> , [Ru <sup>II</sup> (bpm)(tpy)(OH <sub>2</sub> )] <sup>2+</sup> , [Ru <sup>II</sup> (bpy)(tpy)(OH <sub>2</sub> )] <sup>2+</sup> (adapted from Concepcion <i>et al.</i> <sup>72</sup> ) and [Ru <sup>II</sup> (H <sub>2</sub> bim)(tpy)(OH <sub>2</sub> )] <sup>2+</sup> (adapted from Okamura <i>et al.</i> <sup>53</sup> ) complexes. ....	85
<b>Figure 34.</b> UV-visible spectral changes (10 s intervals) upon addition of 1, 2, and 3 equivalents of Ce <sup>IV</sup> to [Ru <sup>II</sup> (Himpy)(tpy)(OH <sub>2</sub> )] <sup>2+</sup> (25 μM) over 15 minutes. ....	87
<b>Figure 35.</b> Absorbance changes after reaction between (1) <sup>4+</sup> (blue) and 1 Eq of CAN. One isosbestic point is shown at 298 nm (inset). ....	88
<b>Figure 36.</b> Absorbance changes along time after successive reaction of (a) [Ru <sup>II</sup> (bpm)(tpy)(OH <sub>2</sub> )] <sup>2+</sup> and (b) <b>(1)</b> with 3 equivalents of CAN, monitored at 283 and 293 nm, respectively. Figure (a) was adapted from Concepcion <i>et al.</i> <sup>84</sup> ....	88
<b>Figure 37.</b> UV-visible spectral changes (30 s intervals) upon addition of 1, 2, and 3 equivalents of Ce <sup>IV</sup> to [Ru <sup>II</sup> (Himpm)(tpy)(OH <sub>2</sub> )] <sup>2+</sup> (15 μM). ....	89
<b>Figure 38.</b> Ce <sup>IV</sup> loss monitored at 360 nm upon addition of 30 equivalents of Ce <sup>IV</sup> to [Ru <sup>II</sup> (Himpm)(tpy)(OH <sub>2</sub> )] <sup>2+</sup> (15 μM). No data was collected during the first 10 s due to the time required for mixing complex and CAN. Each measurement was taken after 120 s. ....	90
<b>Figure 39.</b> Plot of k <sub>obs</sub> (values determined from plotting Abs(360 nm)/εb versus time) versus concentration of complex [Ru <sup>II</sup> (Himpm)(tpy)(OH <sub>2</sub> )] <sup>2+</sup> . It is shown that the graphic could be better represented by a parabolic function, i.e., a second order kinetic reaction. ....	91
<b>Figure 40.</b> Plot of k <sub>obs</sub> versus [complex] <sup>2</sup> . The reaction is second order with respect to [Ru <sup>II</sup> (Himpm)(tpy)(OH <sub>2</sub> )] <sup>2+</sup> . ....	92

## List of Tables

<b>Table 1.</b> Crystallographic data of neutral and protonated Himpx compounds.....	21
<b>Table 2.</b> Reduction and oxidation potentials of Himpx, bpy and tpy ligands in acetonitrile. ....	27
<b>Table 3.</b> <sup>1</sup> H-NMR data for <i>cis</i> -[Ru <sup>II</sup> (Himpy)(tpy)(Cl)] <sup>+</sup> and <i>trans</i> -[Ru <sup>II</sup> (Himpy)(tpy)(Cl)] <sup>+</sup> complexes recorded in CD <sub>3</sub> OD. ....	44
<b>Table 4.</b> <sup>1</sup> H-NMR data for <i>cis</i> -[Ru <sup>II</sup> (Himpz)(tpy)(Cl)] <sup>+</sup> and <i>trans</i> -[Ru <sup>II</sup> (Himpz)(tpy)(Cl)] <sup>+</sup> complexes recorded in DMSO-d <sub>6</sub> . ....	46
<b>Table 5.</b> Crystallographic data for the complex <i>cis</i> -[Ru <sup>II</sup> (Himpy)(tpy)(Cl)](PF <sub>6</sub> )·H <sub>2</sub> O. ....	47
<b>Table 6.</b> Crystallographic data for the complex <i>trans</i> -[Ru <sup>II</sup> (Himpy)(tpy)(Cl)](PF <sub>6</sub> )·CHCl <sub>3</sub> . ....	49
<b>Table 7.</b> <sup>1</sup> H-NMR data for [Ru <sup>II</sup> (Himpy)(tpy)(Cl)] <sup>+</sup> and [Ru <sup>II</sup> (Himpy)(tpy)(OH <sub>2</sub> )] <sup>2+</sup> complexes recorded in DMSO-d <sub>6</sub> . ....	65
<b>Table 8.</b> <sup>1</sup> H-NMR data for [Ru <sup>II</sup> (Himpa)(tpy)(Cl)] <sup>+</sup> and [Ru <sup>II</sup> (Himpa)(tpy)(OH <sub>2</sub> )] <sup>2+</sup> complexes recorded in DMSO-d <sub>6</sub> . ....	69
<b>Table 9.</b> Crystallographic data for the <i>cis</i> -[Ru <sup>II</sup> (Himpy)(tpy)(OH <sub>2</sub> )](ClO <sub>4</sub> ) <sub>2</sub> and <i>trans</i> -[Ru <sup>II</sup> (Himpy)(tpy)(OH <sub>2</sub> )](PF <sub>6</sub> ) <sub>2</sub> complexes. ....	70

## Summary

INTRODUCTION.....	15
CHAPTER 1 .....	16
N-HETEROARYL-2-IMIDAZOLE LIGANDS.....	16
1. INTRODUCTION.....	16
2. OBJECTIVES .....	18
3. EXPERIMENTAL SECTION.....	18
3.1 General.....	18
3.2 Synthesis and crystallization.....	19
3.3 Measurements .....	20
4. RESULTS AND DISCUSSION.....	22
4.1 Conformational Analysis .....	23
4.2 Supramolecular analysis.....	26
4.3 Electrochemistry .....	27
5. CONCLUSIONS .....	30
CHAPTER 2 .....	31
RUTHENIUM CHLORIDOCOMPLEXES.....	31
1. INTRODUCTION.....	31
2. OBJECTIVES .....	31
3. EXPERIMENTAL SECTION.....	32
3.1 General.....	32
3.2 Measurements .....	32
3.3 Synthesis of Ru <sup>III</sup> (tpy)Cl <sub>3</sub> .....	32
3.4 Synthesis of <i>cis</i> -[Ru <sup>II</sup> (Himpy)(tpy)(Cl)]PF <sub>6</sub> .....	33
3.5 Synthesis of <i>trans</i> -[Ru <sup>II</sup> (Himpy)(tpy)(Cl)]PF <sub>6</sub> .....	33
3.6 Synthesis of <i>cis</i> -[Ru <sup>II</sup> (Himpa)(tpy)(Cl)]PF <sub>6</sub> .....	34
3.7 Synthesis of <i>cis</i> -[Ru <sup>II</sup> (Himpz)(tpy)(Cl)]Cl.....	34

3.8 Synthesis of <i>trans</i> -[Ru <sup>II</sup> (Himpz)(tpy)(Cl)]Cl .....	35
3.9 Synthesis of <i>cis</i> -[Ru <sup>II</sup> (Himpm)(tpy)(Cl)]Cl .....	35
3.10 Synthesis of <i>trans</i> -[Ru <sup>II</sup> (Himpm)(tpy)(Cl)]Cl .....	36
4. RESULTS AND DISCUSSION .....	36
4.1 Synthesis and characterization of the ruthenium complexes .....	36
4.2 <sup>1</sup> H-NMR Spectroscopy .....	41
4.3 X-ray crystallography .....	46
4.4. UV-visible spectroscopy .....	49
4.5 pK <sub>a</sub> of Ru(II) chlorido complexes .....	52
CHAPTER 3 .....	54
WATER OXIDATION BY RUTHENIUM AQUA COMPLEXES .....	54
1. INTRODUCTION .....	54
1.1 General concepts .....	54
1.2 Water oxidation .....	54
1.3 Ruthenium polypyridyl complexes .....	55
2. OBJECTIVES .....	59
3. EXPERIMENTAL SECTION .....	59
3.1 General .....	59
3.2 Measurements .....	60
3.3 Synthesis of <i>cis</i> -[Ru <sup>II</sup> (Himpy)(tpy)(OH <sub>2</sub> )](PF <sub>6</sub> ) <sub>2</sub> .....	61
3.4 Synthesis of <i>cis</i> -[Ru <sup>II</sup> (Himpa)(tpy)(OH <sub>2</sub> )](PF <sub>6</sub> ) <sub>2</sub> .....	62
3.5 Synthesis of <i>cis</i> -[Ru <sup>II</sup> (Himpz)(tpy)(OH <sub>2</sub> )](PF <sub>6</sub> ) <sub>2</sub> .....	63
3.6 Synthesis of <i>cis</i> -[Ru <sup>II</sup> (Himpm)(tpy)(OH <sub>2</sub> )](PF <sub>6</sub> ) <sub>2</sub> .....	63
4. RESULTS AND DISCUSSION .....	64
4.1 Synthesis and characterization of the ruthenium complexes .....	64
4.2 <sup>1</sup> H-NMR spectroscopy .....	64
4.3 X-ray crystallography .....	69

4.4 UV-visible spectroscopy.....	72
4.5 $pK_a$ of Ru(II) aqua complexes .....	74
4.6 Electrochemistry of Ru(II) complexes .....	75
4.7 Kinetic studies.....	86
5. CONCLUSIONS .....	93
6. PERSPECTIVES.....	93
7. REFERENCES.....	94
8. APPENDIX.....	100

# INTRODUCTION

# CHAPTER 1

## N-HETEROARYL-2-IMIDAZOLE LIGANDS

This chapter is a summary of the published work about the detailed crystallographic study of changes in the supramolecular network among the isomers and their protonated forms.<sup>1</sup> Complete and detailed information of the work is available at <https://pubs.acs.org/doi/10.1021/acs.cgd.0c00320>. A brief discussion of the electrochemical properties of the ligands showing their electron donor-acceptor behavior is also presented.

### 1. INTRODUCTION

Nitrogen-containing heterocyclic compounds are found in nature as part of many living organisms. A plethora of investigations have been carried out because of their multiple properties, which are exploited in many applications as DNA cleavage agents,<sup>2</sup> FDA approved pharmaceuticals,<sup>3</sup> water oxidation catalysts,<sup>4</sup> proton-conducting MOF materials,<sup>5</sup> atom-transfer radical polymerization<sup>6</sup> as well as among other applications.

N-heterocyclic compounds are very interesting systems not only either biologically or industrially but also crystallographically because many non-covalent interactions occur among their high-diversity structures and other functional groups, which in turn give rise to many supramolecular networks.<sup>7-10</sup> Heteroaryl imidazole molecules are a good example because they feature both nitrogen hydrogen-bond acceptors in the heteroaryl moiety and imidazole N-H donor that can participate in intermolecular hydrogen bond interactions, resulting in scaffolds that serve as the basis for supramolecular assemblies.<sup>11-14</sup> Furthermore, the hydrogen donor-acceptor behavior of those compounds can be fine-tuned depending on their acid-base properties, which could give rise to a vastness of structural possibilities. One interesting example, reported by our group,<sup>15</sup> is the use of two structural isomers of 2-(1*H*-imidazol-2-yl)diazine on the modulation of electronic and magnetic properties of iron(II) complexes, where the isomers only differ in the position of a single nitrogen atom (pyrazine or pyrimidine groups). In this case, minor modifications on the

heteroaryl moiety led to a spin crossover for the pyrazine complex at 241 K, whereas the pyrimidine complex showed stable magnetic behavior. This strategy of ligand design to fine tune properties of coordination compounds were wide explored by our group<sup>6,16–18</sup>. Moreover, for the heteroaromatic compounds, pyridine ( $pK_a$  5.1) forms a 1:1 asymmetric unit in its protonated form with chloranilic acid whereas the pyridazine molecule ( $pK_a$  2.3) forms a 2:1 asymmetric unit in its protonated form with that acid.<sup>19</sup> When it comes to more ionizable acids such as pyrimidinium ( $pK_a$  1.3) or pyrazinium ( $pK_a$  0.7), they form 2:1 asymmetric units in their neutral form with the same acid.<sup>20</sup>

Several works explore intermolecular interactions of imidazolium-containing compounds with carboxylic acids,<sup>21</sup> halogens,<sup>22</sup> and metal ions,<sup>23</sup> providing a huge diversity of supramolecular assemblies for different purposes such as crystal engineering,<sup>24</sup> organic-inorganic hybrid ferroelectric materials,<sup>25</sup> ionic liquid compounds.<sup>26</sup> Systematic studies of crystal structures of neutral heteroaryl imidazole-containing compounds, as well as their protonated forms and their supramolecular arrangement patterns, are scarce in the literature<sup>27</sup> even in reputable databases such as the Cambridge Crystallographic Data Centre. One rare example is the work using heteroaryl-2-imidazole molecules which were co-crystallized along with halogen-containing molecules to assess the competition between halogen-bond interactions and hydrogen-bond interactions in the assembly of the supramolecular network.<sup>28</sup>

In this chapter, we present the systematic design of crystal structures of four neutral N-heterocyclic compounds bearing one imidazole ring (Him) along with their respective protonated species (**Chart 1**). Three of them are isomeric diazines differing in the position of one nitrogen in the six-membered ring named after their parent N-heterocycles: pyridazine (Himpa), pyrimidine (Himpm), and pyrazine (Himpz). In order to assess the changes in the supramolecular network induced by the absence of this second nitrogen atom, we have also studied the related molecule in which the six-membered ring is pyridine (Himpy). The detailed crystallographic study reveals that they are self-assembled through hydrogen bonding and other non-covalent bonding interactions resulting in quite different supramolecular networks when the isomers are compared as well as after the protonation.

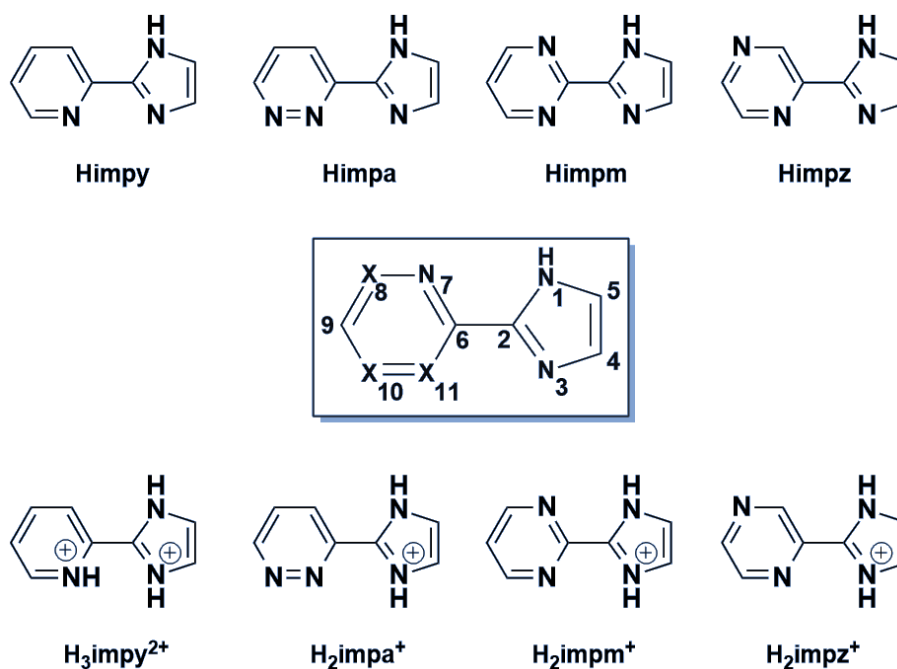


**Chart 1.** Molecular structures of the neutral and protonated N-heteroaryl-imidazole compounds (Himp<sub>x</sub>). The same numbering scheme is used for all molecules in both crystallographic and spectroscopic results.

## 2. OBJECTIVES

- Study the molecular structures of the Himp<sub>x</sub> ligands and the differences among them induced by their isomerism.
- Investigate the donor-acceptor behavior of the Himp<sub>x</sub> ligands through electrochemical measurements.

## 3. EXPERIMENTAL SECTION

### 3.1 General

Buffer solutions of 4.0, 7.0 and 10.0 (Labsynth), sodium hydroxide (97%, Dinâmica Química Contemporânea Ltda.) were received and used without further purification. Diethyl ether and hydrochloric acid were purchased from Labsynth. Acetonitrile (CHROMASOLV™, gradient grade, for HPLC, ≥ 99.9%) for electrochemical measurements was purchased from Honeywell Research Chemicals.

Molecular sieves (4Å, beads, 4-8 mesh, Sigma-Aldrich) were used for drying organic solvents for further measurements.

### 3.2 Synthesis and crystallization

The neutral 2-(1*H*-imidazol-2-yl)heteroaryl (Himpx) compounds were synthesized in a one-pot reaction, with minor modifications to the procedure described by Voss *et al.*<sup>29</sup>.

To a 50-mL round-bottom flask, 1.31 g (12.5 mmol) of 2-pyridinecarbonitrile in 15 mL of methanol and 0.60 mL of sodium methoxide solution were added and left under stirring at about 50 °C for 1 hour and a half. Then, 1.360 mL (12.5 mmol, 1 eq.) of aminoacetaldehyde dimethyl acetal and 1.375 mL (1 eq.) of glacial acetic acid were added to the solution, followed by refluxing for 50 minutes. After cooling to room temperature, methanol (5 mL) and hydrochloric acid (6.25 mL, 6 mol L<sup>-1</sup>) were added to the resulting yellow solution and heated to reflux for 5 hours. By the end, the solvent was removed, followed by the slow addition of 20 mL of a freshly prepared warm solution of potassium carbonate (1 g mL<sup>-1</sup>) until the solution reached a pH around 10, leading to the formation of a yellow dark suspension which was then filtered to obtain a yellowish solid. This solid was dissolved in dichloromethane resulting in a dark red solution, which was filtered, and the obtained product was dried under reduced pressure. The red solid obtained was dissolved in warm ethyl acetate and left to cool. The resulting solid was filtered and washed with cold ethyl acetate (3 × 5 mL). The final product was obtained as a slightly yellowish solid (off-white). Yield: 63%. Anal. Calcd for C<sub>8</sub>H<sub>7</sub>N<sub>3</sub>: C, 66.19; H, 4.86; N, 28.95. Found: C, 66.09; H, 4.69; N, 29.03. mp 134–135 °C. FTIR-ATR/cm<sup>-1</sup>: 3044 (m), 1594 (m), 1568 (m), 1478 (s), 1458 (s), 1374 (m), 1135 (m), 1107 (s), 992 (m), 954 (m), 787 (s), 706 (s), 621 (m), 503 (m), 462 (m). <sup>1</sup>H-NMR (600 MHz, DMSO-d<sub>6</sub>, 25 °C): δ/ppm 12.75 (s, 1H), 8.58 (ddd, 1H, J = 5.4, 1.8, 1.2 Hz), 8.02 (d, 1H, J = 9.6 Hz), 7.87 (td, 1H, J = 9.0, 1.8 Hz), 7.34 (ddd, 1H, J = 9.0, 6.0, 1.2 Hz), 7.14 (s, 2H). <sup>13</sup>C-NMR (125 MHz, DMSO-d<sub>6</sub>, 25 °C): δ/ppm 149.48, 149.41, 146.06, 137.67, 124.55, 123.42, 119.88. HR-ESI-(+)-MS (CH<sub>3</sub>OH) m/z: 146.0 [M+H]<sup>+</sup>.

The other ligands were synthesized similarly to the Himpy ligand. Single crystals suitable for diffraction analysis were obtained by slow recrystallization of a

methanolic solution (5 mL) containing 10 mg of neutral Himp<sub>x</sub>, that was placed in a 10 ml vial with a needle perforated lid at room temperature for 1 week, from where the crystals were collected. The protonated compounds were prepared by dissolving 30 mg (0.2 mmol) of the neutral Himp<sub>x</sub> in a 10-mL glass vial containing 5 mL of methanol, followed by addition of 167  $\mu\text{L}$  of a 1.2 mol L<sup>-1</sup> HCl aqueous solution. The reaction mixture was stirred for 5 minutes at room temperature and left to evaporate open to the atmosphere. Crystals were obtained after 2 weeks.

### 3.3 Measurements

#### X-ray diffraction

Single-crystal X-ray diffraction experiments were carried out on a Bruker APEX II duo CCD area detector diffractometer. For the single crystals Himp<sub>a</sub>, Himp<sub>m</sub>, H<sub>2</sub>imp<sub>m</sub>Cl, Himp<sub>z</sub> and H<sub>2</sub>imp<sub>z</sub>Cl, a Mo K $\alpha$  ( $\lambda = 0.71073 \text{ \AA}$ ) radiation was used from a fine-focus sealed tube with a curved graphite monochromator. For H<sub>2</sub>imp<sub>a</sub>Cl, Himp<sub>y</sub> and H<sub>3</sub>imp<sub>y</sub>Cl<sub>2</sub>, a Cu K $\alpha$  ( $\lambda = 0.71073 \text{ \AA}$ ) radiation was used from an INCOATEC®  $\mu\text{s}$  microsource. All measurements were carried out at 150.0 K using a low-temperature device (Oxford Cryosystems 700 series). Unit cell dimensions and orientation matrices were determined by the least-squares refinement of the reflections obtained by  $\varphi$  and  $\omega$  scans. For all data sets, SAINT software<sup>30</sup> implemented in the Bruker APEXII suite was used for integration and scaling.<sup>31</sup> Absorption correction was applied using SADABS.<sup>31</sup>

The crystal structures were solved using SHELXT<sup>32</sup> structure solution program using the intrinsic phasing method and refined on  $F^2$  by a full-matrix least-squares method with the SHELX program<sup>33</sup> into the Olex2 software suite.<sup>34</sup> For all the non-hydrogen atoms, anisotropic displacement parameters (ADP) were applied. The hydrogen atoms were observed in the Fourier maps, then placed at geometrically calculated positions and refined using an appropriated riding model regarding the parent atom. For the aromatic C–H bonds, the H atoms were restrained at 0.950  $\text{\AA}$  and  $U_{\text{iso}}(\text{H}) = 1.2U_{\text{eq}}(\text{C})$ ; for the N–H bonds, the H positions were fixed at 0.880  $\text{\AA}$  and  $U_{\text{iso}}(\text{H}) = 1.2U_{\text{eq}}(\text{N})$ ; and for the O–H bonds in water molecules, H atoms were treated with  $U_{\text{iso}}(\text{H}) = 1.5U_{\text{eq}}(\text{O})$ . The structures H<sub>2</sub>imp<sub>m</sub>Cl, Himp<sub>y</sub> and H<sub>2</sub>imp<sub>z</sub>Cl were refined

as a 2-component inversion twin using TWIN/BASF<sup>33</sup> with twin fractions of 0.57, 0.29 and 0.47, respectively. The molecular and crystallographic graphs were generated using the programs Olex2,<sup>34</sup> ORTEP-3<sup>35</sup> and Mercury.<sup>36</sup> Search on the Cambridge Structural Database (CSD)<sup>37</sup> were carried with the aim of the Conquest program.<sup>38</sup> The crystallographic data and structural refinement of all compounds are summarized in **Table 1**. The crystallographic information files of all structures were validated by the CheckCIF server and deposited in CSD with the code numbers: 1984150, 198451, 198452, 198453, 198454, 198455, 198456, and 198457. The CIF files can be obtained free of charge via [www.ccdc.cam.ac.uk](http://www.ccdc.cam.ac.uk).

**Table 1.** Crystallographic data of neutral and protonated Himp<sub>x</sub> compounds.

Crystal Id	Himpa	Himp <sub>m</sub>	Himp <sub>z</sub>	Himp <sub>y</sub>
Molecular formula	C <sub>7</sub> H <sub>6</sub> N <sub>4</sub>	C <sub>7</sub> H <sub>6</sub> N <sub>4</sub>	C <sub>7</sub> H <sub>6</sub> N <sub>4</sub>	C <sub>8</sub> H <sub>7</sub> N <sub>3</sub>
Formula weight	146.16	146.16	146.16	145.17
T (K)	150(2)	150(2)	100(2)	100(2)
λ (Å)	0.71073	0.71073	0.71073	1.54178
Crystal system	Orthorhombic	Monoclinic	Monoclinic	Orthorhombic
Space group	P b c a	I 2/a	P 21/c	C c c 2
a (Å)	10.7093(8)	22.5667(16)	7.2269(18)	19.457(2)
b (Å)	10.1180(8)	6.9805(4)	9.650(2)	29.518(2)
c (Å)	12.7040(10)	27.260(3)	9.864(3)	10.0753(8)
α (°), β (°), γ (°)	90	90, 107.9790(10), 90	90, 91.481(5), 90	90
V (Å <sup>3</sup> )	1376.56(18)	4084.5(5)	687.7(3)	5786.6(9)
Z	8	24	4	32
ρ <sub>calcd</sub> (g cm <sup>-3</sup> )	1.410	1.426	1.412	1.333
μ (mm <sup>-1</sup> )	0.095	0.096	0.095	0.687
F(000)	608	1824	304	2432
Crystal size (mm <sup>3</sup> )	0.330 x 0.190 x 0.132	0.532 x 0.285 x 0.160	0.158 x 0.148 x 0.096	0.460 x 0.264 x 0.244
θ range for data collection (°)	3.201 to 28.296	1.571 to 28.304	2.819 to 26.872	4.388 to 68.837
Index ranges	-14 ≤ h ≤ 14, -13 ≤ k ≤ 12, -16 ≤ l ≤ 16	-30 ≤ h ≤ 30, -8 ≤ k ≤ 9, -36 ≤ l ≤ 36	-9 ≤ h ≤ 8, -12 ≤ k ≤ 12 -12 ≤ l ≤ 12	-23 ≤ h ≤ 15, -35 ≤ k ≤ 35, -12 ≤ l ≤ 12
Reflections collected	16528	41410	7992	32608
Independent reflections	1710 [R(int) = 0.0314]	5081 [R(int) = 0.0236]	1486 [R(int) = 0.0314]	5152 [R(int) = 0.0646]
Completeness to θ <sub>max</sub> (%)	100.0	100.0	100.0	98.9
Data / restraints / parameters	1710 / 0 / 100	5081 / 0 / 299	1486 / 0 / 101	5152 / 1 / 399
Goodness-of-fit on F <sup>2</sup>	1.046	1.031	1.029	1.072
Final R indices (I > 2σ(I))	R <sub>1</sub> = 0.0361, wR <sub>2</sub> = 0.0986	R <sub>1</sub> = 0.0345, wR <sub>2</sub> = 0.0926	R <sub>1</sub> = 0.0357, wR <sub>2</sub> = 0.0839	R <sub>1</sub> = 0.0383, wR <sub>2</sub> = 0.0918

R indices (all data)	R <sub>1</sub> = 0.0432, wR <sub>2</sub> = 0.1044	R <sub>1</sub> = 0.0405, wR <sub>2</sub> = 0.0992	R <sub>1</sub> = 0.0508, wR <sub>2</sub> = 0.0922	R <sub>1</sub> = 0.0388, wR <sub>2</sub> = 0.0920
Extinction coefficient	n/a	0.00144(17)	0.016(3)	0.00081(9)
Largest diff. peak and hole (e Å <sup>-3</sup> )	0.315 and -0.252	0.345 and -0.178	0.256 and -0.224	0.267 and -0.223

Crystal Id	H <sub>2</sub> impaCl	H <sub>2</sub> impmCl	H <sub>2</sub> impzCl	H <sub>3</sub> impyCl <sub>2</sub>
Molecular formula	C <sub>7</sub> H <sub>9</sub> ClN <sub>4</sub> O	C <sub>7</sub> H <sub>9</sub> ClN <sub>4</sub> O	C <sub>7</sub> H <sub>9</sub> ClN <sub>4</sub> O	C <sub>8</sub> H <sub>9</sub> Cl <sub>1.99</sub> N <sub>3</sub>
Formula weight	200.63	200.63	200.63	217.82
T (K)	150(2)	150(2)	150(2)	150(2)
λ (Å)	1.54178	0.71073	0.71073	1.54178
Crystal system	Monoclinic	Monoclinic	Monoclinic	Orthorhombic
Space group	P 21/c	C 2	P c	P n m a
a (Å)	4.6771(2)	7.2712(12)	5.2021(5)	14.6699(8)
b (Å)	11.6787(6)	24.226(4)	11.4313(10)	6.4026(4)
c (Å)	16.7418(8)	10.6553(17)	7.8763(7)	10.5657(6)
α (°), β (°), γ (°)	90, 90.793(3), 90	90, 103.854(3), 90	90, 92.728(2), 90	90
V (Å <sup>3</sup> )	914.39(8)	1822.4(5)	467.85(7)	992.39(10)
Z	4	8	2	4
ρ <sub>calcd</sub> (g cm <sup>-3</sup> )	1.457	1.463	1.424	1.458
μ (mm <sup>-1</sup> )	3.443	0.384	0.374	5.513
F(000)	416	832	208	447
Crystal size (mm <sup>3</sup> )	0.225 x 0.091 x 0.065	0.389 x 0.118 x 0.051	0.226 x 0.100 x 0.095	0.365 x 0.163 x 0.064
θ range for data collection (°)	4.616 to 66.236	1.681 to 28.355	1.781 to 28.294	5.159 to 68.765
Index ranges	-5 ≤ h ≤ 4, -13 ≤ k ≤ 13, -18 ≤ l ≤ 19	-9 ≤ h ≤ 9, -29 ≤ k ≤ 32, -14 ≤ l ≤ 13	-6 ≤ h ≤ 6, -15 ≤ k ≤ 15, -10 ≤ l ≤ 10	-17 ≤ h ≤ 17, -7 ≤ k ≤ 7, -8 ≤ l ≤ 12
Reflections collected	5938	11154	8944	7540
Independent reflections	1551 [R(int) = 0.0257]	4367 [R(int) = 0.0276]	2308 [R(int) = 0.0229]	991 [R(int) = 0.0438]
Completeness to θ <sub>max</sub> (%)	96.8	99.9	100.0	99.5
Data / restraints / parameters	1551 / 0 / 127	4367 / 82 / 196	2308 / 2 / 125	991 / 0 / 86
Goodness-of-fit on F <sup>2</sup>	1.065	1.120	1.074	1.123
Final R indices (I > 2σ(I))	R <sub>1</sub> = 0.0313, wR <sub>2</sub> = 0.0806	R <sub>1</sub> = 0.0669, wR <sub>2</sub> = 0.1651	R <sub>1</sub> = 0.0241, wR <sub>2</sub> = 0.0561	R <sub>1</sub> = 0.0468, wR <sub>2</sub> = 0.1180
R indices (all data)	R <sub>1</sub> = 0.0329, wR <sub>2</sub> = 0.0820	R <sub>1</sub> = 0.0833, wR <sub>2</sub> = 0.1830	R <sub>1</sub> = 0.0261, wR <sub>2</sub> = 0.0571	R <sub>1</sub> = 0.0481, wR <sub>2</sub> = 0.1202
Extinction coefficient	n/a	0.013(2)	n/a	n/a
Largest diff. peak and hole (e Å <sup>-3</sup> )	0.227 and -0.251	0.636 and -2.449	0.195 and -0.162	0.551 and -0.616

## 4. RESULTS AND DISCUSSION

## 4.1 Conformational Analysis

### Himpa & H<sub>2</sub>impaCl

The Himpa compound crystallizes in the orthorhombic space group *Pbca* with one molecule per asymmetric unit. The conformational structure is characterized mainly by a dihedral angle between the imidazole-ring (imi) and the pyridazine-ring (pyra) planes of 7.74(4)°, which reveals a very slight distortion in the planarity of this molecule. Conversely, the bond length C2–C6, which defines the separation between the rings, is 1.4619(15) Å. The bond angles C2–N1–C5 and C2–N3–C4 of the imi-ring are 107.36(9)° and 104.92(9)°, respectively. Therefore, the ring relaxation and a conspicuous residual electron density observed in the Fourier map confirm the presence of the H-atom attached in N1. The azo group shows a bond length N7–N8 of 1.3436(13) Å.

The chloride salt H<sub>2</sub>impaCl crystallizes in the monoclinic space group *P21/c* with one ionic pair and one water molecule per asymmetric unit. The protonated H<sub>2</sub>impa<sup>+</sup> unit exhibits planarity of 4.65(5)° because of the dihedral angle between the imi- and pyra-rings when compared to neutral Himpa. The separation between the rings C2–C6 is 1.4661(21) Å, quite similar to the observed one in the neutral form. The protonation is evident over imi because of the observed ring relaxation, since the bond angles C2–N1–C5 and C2–N3–C4 are 108.92(13)° and 109.00(13)°, respectively. In H<sub>2</sub>impaCl, the azo group has a bond length N7–N8 of 1.3387(18) Å which is not a meaningful difference regarding the neutral form.

### Himp<sub>m</sub> & H<sub>2</sub>imp<sub>m</sub>Cl

Himp<sub>m</sub> crystallizes in the non-standard monoclinic space group *I2/a*, with the presence of three Himp<sub>m</sub> conformers per asymmetric unit. The bond angles C2–N1–C5 and C2–N3–C4 of the imi-rings for each conformer are A:107.12(6)°, B:106.90(3)°, C:107.21(6)° and A:104.77(5)°, B:104.56(3)°, C:105.19(7)°, respectively, demonstrating the neutrality of these molecules. On the other hand, the pyrimidine (pym) ring shows the bond angles C6–N7–C8 (A: 115.85(6)°, B: 116.22(3)° and C:115.89(8)°) and C6–N11–C10 (A: 115.46(6)°, B: 116.08(3)° and C: 115.44(6)°), which indicate a more constrained ring and π-character, common for neutral conformations. The dihedral angle between the mean planes of the imi and pym rings

range from A: 20.21°, B: 15.39° and C: 5.81°, revealing a significant variation of conformations for each conformers of Himp<sub>m</sub> in which the planarity is more distorted than the analogous compounds Him<sub>p</sub>a and Him<sub>p</sub>y (as described in the next section). That could be possibly explained by a strong electronic repulsion between the lone pair electrons of the N-pyrm and N-imi atoms, as well as by crystal packing effects. The separation between the rings is defined by the C2–C6 bond lengths A: 1.4648(1) Å, B: 1.4585(1) Å and C: 1.4615(1) Å.

H<sub>2</sub>imp<sub>m</sub>Cl is a multicomponent hemihydrate hydrochloride salt with partial protonation, which crystallized in the monoclinic space group C2. The structure is made up of three ionic pairs and consequently of three different conformers H<sub>2</sub>imp<sub>m</sub><sup>+</sup>:xCl<sup>-</sup> (two of them with partial protonation), and disordered water molecules per asymmetric unit. The partially protonated ionic pairs lie in a special position over the 2-fold axis, which intercepts half of the corresponding symmetric H<sub>2</sub>imp<sub>m</sub><sup>+</sup> units. That features a partial protonation because a substitutional disorder is observed over the same occupation site of the corresponding Cl<sup>-</sup> ions attached to these molecules, with water molecules present in the crystal lattice. A priori, the protonation of the Himp<sub>m</sub> molecules can be estimated by the corresponding higher C–N–C bond angles of imi-rings, observed only for the conformer A (C2A–N1A–C5A: 110.83(1)°, C2A–N3A–C4A: 110.09(1)°), whereas it was not so evident for the other conformers which are in special positions (C2B–N1B–C5B: 107.25(9)° and C2C–N1C–C5C: 109.00(9)°). The C–N–C bond angles of the pyrm rings reveal a normal behavior for resonant aromatic rings (C6A–N7A–C8A: 114.90(4)°, C6A–N11A–C10A: 115.29(6)°, C6B–N7B–C8B: 113.97(5)° and C6C–N7C–C8C: 114.95(5)°). An important structural feature is regarding the differences in the dihedral angles of the mean planes of imi and pyrm rings (A: 3.06(6)°, B: 1.56(3)° and C: 3.95(8)°). Thus, there is a small difference between each of these dihedral angles ca. 1.0°, so that a preferential planar conformation is maintained in all cases. Therefore, the main structural feature that distinguishes the conformations among these molecules is the C–N–C bond angle of imi-rings, which suggests that there is a partial protonation in conformers B and C because of the intermediate values of these angles along with the evident substitutional disorder in the Cl<sup>-</sup> ions as observed during the structural refinement. The separation between the rings, corresponding to bond lengths C2–C6 (A: 1.4557(2) Å,

B: 1.4619(2) Å and C: 1.4768(2) Å) have no meaningful differences among the conformers as well, despite a slight shortening in conformer A.

### Himpy & H<sub>3</sub>impyCl<sub>2</sub>

Himpy crystallizes in the orthorhombic space group Ccc2, with 4 molecules per asymmetric unit, corresponding therefore to four different conformers (A, B, C and D) of Himpy molecules. The most important structural features in Himpy are mainly related to bond angles of the imi-rings C2–N1–C5 (A:107.21(4)°, B:106.81(7)°, C:107.25(4)°, D:106.98(7)°) and C2–N3–C4 (A:105.27(4)°, B:105.01(7)°, C:104.95(4)°, D:104.90(7)°). The dihedral angles between the mean planes of the imi and pyridine (py) rings for each of the conformers show values of A:8.633°, B: 7.196°, C: 6.887° and D: 6.656°. Regarding the py-ring, the angles C6–N7–C8 show values for each conformers of A: 117.16(5)°, B: 117.21(7)°, C: 117.38(5)° and D: 117.53(8)°. In this manner, one can see that all these structural parameters agree with expected values for neutral conformations.

H<sub>3</sub>impyCl<sub>2</sub> crystallizes in the orthorhombic space group Pnma, in which there are one di-protonated Himpy molecule and two chloride ions per asymmetric unit. We were not able to isolate the monoprotonated crystal structure (H<sub>2</sub>impyCl). Contrary to what was observed for a similar molecule 2,6-bis(1H-imidazol-2-yl)-pyridine,<sup>27</sup> our results for Himpy showed that the p*K*<sub>a</sub> for the imidazolium species (5.50) was much higher than for the pyridinium one (second protonation takes place below pH 1) so the best possible reason for the lack of success in the crystallization is the instability of this species and not the difference between p*K*<sub>a</sub> values in this case. The geometric parameters of the imi-ring features for the bond angle values of C2–N1–C5: 107.70(2)° and C2–N3–C4:108.87(2)°, which clearly depicts the protonation of this ring. Additionally, the py ring exhibits a meaningful high bond angle C6–N7–C8 of 123.94(3)° when compared with the neutral Himpy conformers, displaying the protonation over the N-pyridine atoms as well. The separation between the imi and py rings is defined by the bond length C2–C6 at 1.4588(1) Å, whereas the high planarity of this conformation is defined by the dihedral angle between the mean planes which corresponds to 0°. A static positional disorder was observed for the Cl<sup>–</sup> anions, which were refined each into two positions with site occupation factors of Cl1A:Cl1B (0.65:0.35) and Cl2A:Cl2B (0.9:0.1).

### Himpz & H<sub>2</sub>impzCl

Himpz crystallizes in the monoclinic space group P21/c with one molecule per asymmetric unit. The structural conformation is featured by the bond angles C2–N1–C5 and C2–N3–C4 of the imi-rings with values of 107.42(1)° and 105.25(2)° respectively, which justifies the presence of the H atom attached in N1. The pyrazine (pyrz) ring shows the two bond angles C6–N7–C8 and C9–N10–C11 at 115.90(9)° and 116.07(9)°, respectively. These bond angles combined with an inspection of the residual electron density maps show the presence of the lone pair electrons over the sp<sup>2</sup>-hybridized N7 and N10 atoms. The dihedral angle between the mean planes imi and pyrz rings is 7.37(2)°, whereas the separation between the rings (bond length C2–C6) is 1.4608 (3) Å.

H<sub>2</sub>impzCl is the monohydrate hydrochloride salt derivative that crystallizes in the Pc space group with one H<sub>2</sub>impz<sup>+</sup>Cl<sup>-</sup> ionic pair and one water molecule per asymmetric unit. The protonation over the N atoms in the imi-ring is identified by the bond angles C2–N1–C5 and C2–N3–C4 (108.90(1)° and 108.93(1)°, respectively), which reveals a more relaxed ring. The bond angles C6–N7–C8 and C9–N10–C11 of pyrz-ring are 115.84(2)° and 116.55(2)°, respectively, showing like in Himpz the presence of the lone pair electrons in the pyrazine N-atoms. The dihedral angle of the mean planes imi and pyrz rings is 7.89(5)°, very close to the observed in the neutral species. The Cl<sup>-</sup> ion is localized at 0.256(3) Å regarding the mean plane that passes through the non-hydrogen atoms of the imi-ring and at 4.1738(7) Å regarding the centroid. The bond length C2–C6 is 1.456(2) Å, which evidences a small shortening in the separation between the rings after the protonation.

### 4.2 Supramolecular analysis

The supramolecular behavior of this group of molecules is mainly characterized by the hydrogen bond (HB) pattern adopted among the Himp<sub>x</sub> molecules, and specifically in the relative orientation between them along the crystal packing, wherein the pattern is mainly affected as a consequence of the protonation. In that point, we can observe a recurrence of the HB pattern in all the neutral species that is defined by an infinite chain of  $C_1^1(4)$  descriptor type,<sup>39</sup> according to the graph-

set theory, and adopts a butterfly shape form, resulting in a herringbone pattern for the whole crystal close packing, a common pattern in imidazole derivatives.<sup>40</sup>

A quite different situation is observed in all the protonated structures, where the crystal packing is recurring and characterized by layer  $\pi$ -stacking. The presence of water molecules that contributes to the stabilization of this layering pattern is also observed for protonated diazines. Therefore, the protonation effect breaks down the herringbone pattern observed in the neutral species. The layer stacking results in a better distribution of the charges, allowing minimum repulsion and maximum attraction, respectively.

### 4.3 Electrochemistry

Cyclic voltammetry measurements were performed on the Himp $x$  ligands solutions to study their donor-acceptor properties. The cyclic voltammograms show slightly different oxidation potentials among them whereas their reduction potentials are fairly different (**Figure 1**). The graphic consists of blue cyclic voltammograms scanned in the potential region -0.25 – 1.25 V to observe the oxidation potentials, which arise when the potential is swept positively, and red cyclic voltammograms scanned in the potential region -2.75 – -0.25 V to observe the reduction potentials, which arise when potential is swept negatively).

Reduction peaks are observed at negative potentials ranging from -2.054 to -2.543 V whereas only one oxidation peak is observed in the region +0.952 – +1.094 V. All these potential waves are related to irreversible redox processes, which could be a consequence of the pyrrole proton involved in subsequent reactions after redox events.<sup>41</sup> **Table 2** summarizes the electrochemical data obtained for the Himp $x$  ligands.

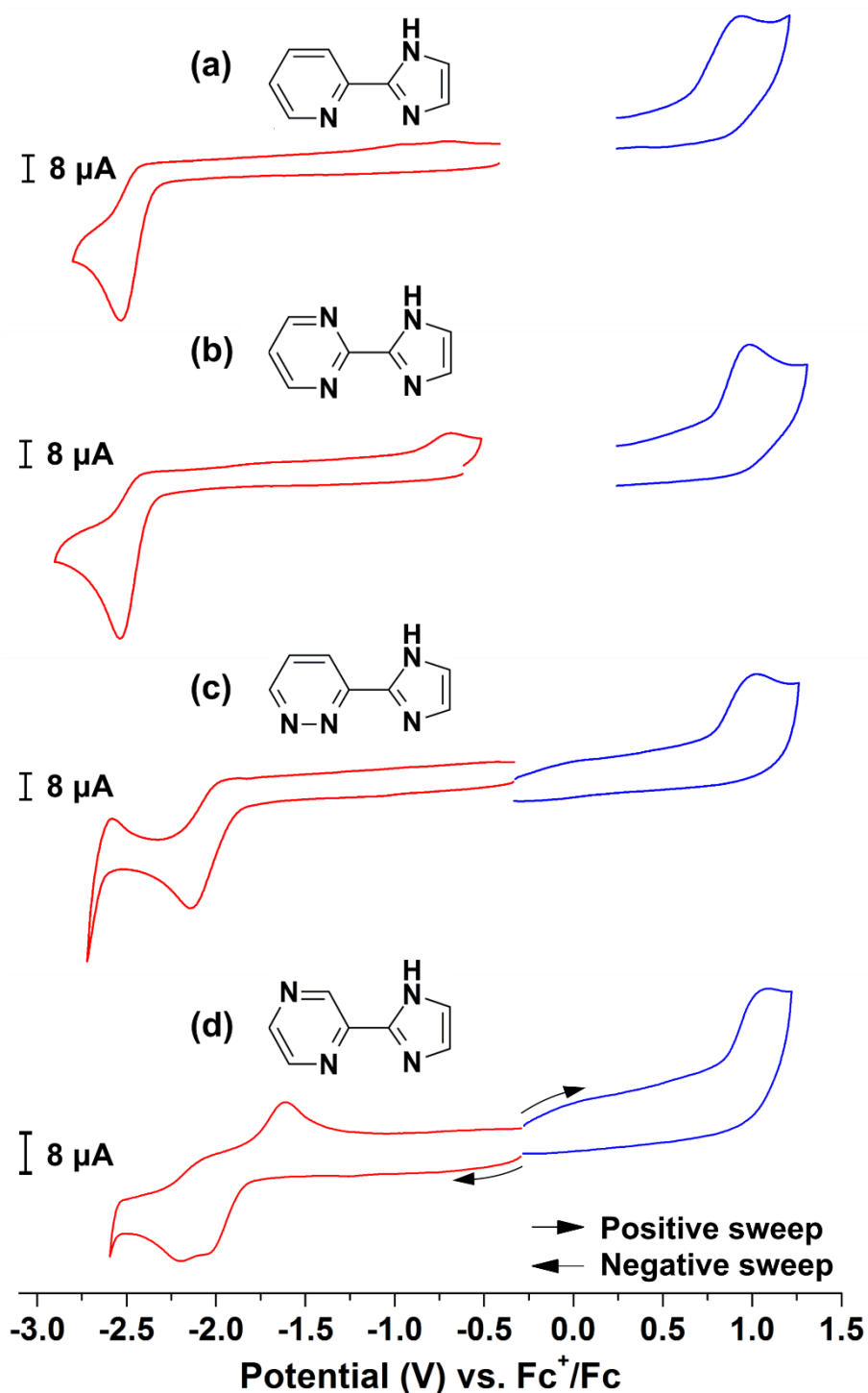


**Figure 1.** Cyclic voltammograms of Himpx ligands (2 mM) recorded in acetonitrile containing 0.1 M TBAPF<sub>6</sub> under N<sub>2</sub>. Scan rate: 0.1 V s<sup>-1</sup>. (a) Himpy, (b) Himpm, (c) Himpa, (d) Himpz. WE: Glassy carbon electrode; RE: AgCl/Ag; CE: Pt wire. The potentials were referenced against Fc<sup>+</sup>/Fc couple and obtained by performing the cyclic voltammetry along with the Fc<sup>+</sup>/Fc in solution and then subtracting the Himpx potential from the potential of the Fc<sup>+</sup>/Fc couple.

**Table 2.** Reduction and oxidation potentials of Himpx, bpy and tpy ligands in acetonitrile.

Ligand	$E_{red}$ (V)	$E_{ox}$ (V)
Himpy	-2.537	+0.952
Himpm	-2.543	+1.002
Himpa	-2.145	+1.039
Himpz	-2.054 -2.195	+1.094
bpy	-2.537 -2.819	a
tpy	-2.512 -2.940	a

<sup>a</sup> No oxidation peaks were observed in the swept potential window.

According to **Table 2**, Himpa and Himpz exhibit outstanding acceptor properties in the Himpx ligands series and compared to bpy and tpy ligands. Furthermore, all of the Himpx ligands display oxidation potentials which are not accessible by the bpy and tpy ligands in the swept potential window, which is important for our purpose to improve the catalytic performance for water oxidation because such lower oxidation potentials can influence on the electronic properties of the Ru(II) complexes.<sup>4,42</sup> Among the Himpx series, we note that Himpy displays the lowest oxidation potential which could be associated with greater donor behavior. Such properties are quite interesting and important for the aim of the Thesis because they exhibit better donor-acceptor behavior compared to the traditional ligands bipyridine (bpy) and terpyridine (tpy) (their reduction potentials are listed in **Table 2**) used in water oxidation catalysis.

The electronic properties of the ligands at different pH media were studied through cyclic and differential pulse voltammetry measurements. The oxidation potential in the cyclic and differential pulse voltammograms of the Himpy ligand (**Figure 2**) are shifted to negative values as the pH increases, which is related to the

deprotonation of the N–H proton and hence an increased electronic density. All the Himp<sub>x</sub> ligands showed this pH-dependence oxidation potential. This outstanding behavior shows the interesting versatility of the Himp<sub>x</sub> ligands as it can be exploited in applications requiring proton-electron transfer reactions such as water oxidation.

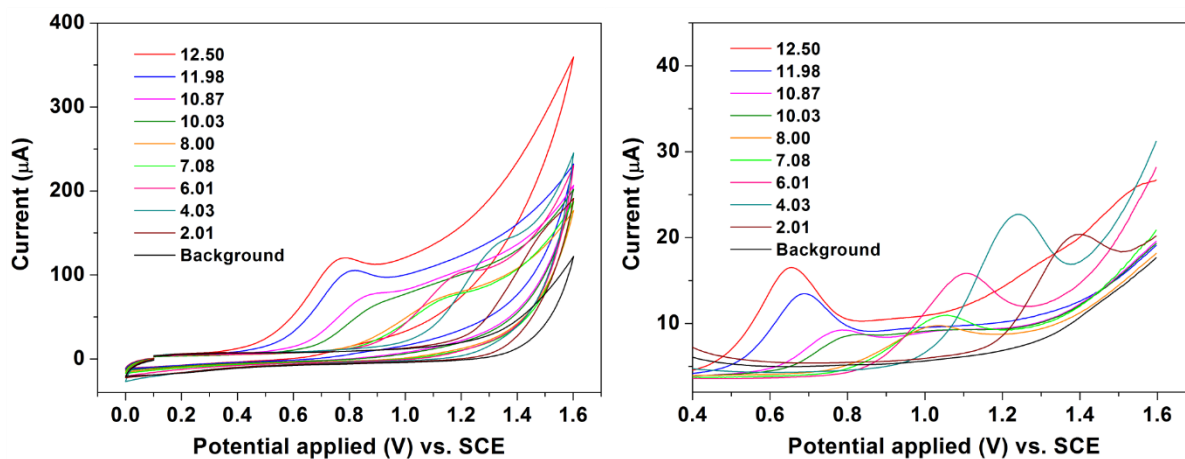


**Figure 2.** Cyclic voltammograms and differential pulse voltammograms of the Himp<sub>y</sub> ligand (2 mM) in different pH media. 0.04 M Britton–Robinson buffer and 0.1 M KNO<sub>3</sub> were used as the supporting electrolyte. WE: GCE. RE: SCE. CE: Pt.

## 5. CONCLUSIONS

We have analyzed the intermolecular interaction landscape and hence the most recurrent crystal packing patterns in different solid forms derived from N-heteroaryl-imidazole molecules (Himp<sub>x</sub>). We have identified two predominant types: the characteristic herringbone pattern in neutral compounds and the  $\pi$ -stacking layering adopted by protonated forms. In this manner, it was possible to observe that the framework of herringbone pattern is mainly characterized by the presence of C–H $\cdots\pi$  interactions whereas the layering is favored by  $\pi\cdots\pi$  and anion- $\pi$  interactions. Himp<sub>y</sub> featured the most differentiated crystal packing among the structures herein studied, because of possessing only one N-atom in the aryl group.

Himpa and Himp<sub>z</sub> are the best acceptor ligands among the Himp<sub>x</sub> ligands series and bpy and tpy ligands, whereas Himp<sub>y</sub> is the best donor ligands evidenced by its lowest oxidation potential.

# CHAPTER 2

## RUTHENIUM CHLORIDOCOMPLEXES

### 1. INTRODUCTION

Traditionally, most of the works related to the preparation of ruthenium aqua complexes use the ruthenium chlorido complexes as precursors because of the simple synthetic procedure. However, in some cases their use has not been limited to being merely intermediates, but also proving to be catalysts for water oxidation. For example, in 2008, Thummel and coworkers<sup>43</sup> reported the catalytic activity for water oxidation of seven ruthenium chlorido compounds containing polypyridine-type ligands, where the chlorido ligand was part of the proposed seven-coordinated intermediate involved in the possible mechanism of the water oxidation process. In other cases, the chlorido complexes proved to be not suitable catalysts for water oxidation and were used to provide the *in situ*-generated aqua complexes to perform the oxidation of water.<sup>44,45</sup>

In this Thesis, in all cases the key step was to obtain the purified chlorido complexes because of the side reactions induced by the presence of electron donor-nitrogen atoms in both aromatic pyridyl and imidazole rings which produced isomers compounds and lowered the efficiency of the synthesis.

In this chapter, the synthesis and characterization of the ruthenium(II) chlorido complexes containing the heteroaryl-2-imidazole ligands and the study of their electronic properties will be described to further compare them with the ruthenium(II) aqua complexes.

### 2. OBJECTIVES

Synthesis and characterization of the ruthenium chlorido complexes, and further evaluation of their properties for comparison with the ruthenium aqua complexes.

### 3. EXPERIMENTAL SECTION

#### 3.1 General

Ammonium hexafluorophosphate ( $\text{NH}_4\text{PF}_6$ , 99.98%, Sigma Aldrich), ascorbic acid (99%, Sigma Aldrich), buffer solutions of 4.0, 7.0 and 10.0 (Labsynth), lithium chloride (98%, Synth), ruthenium(III) chloride trihydrate ( $\text{RuCl}_3 \cdot 3\text{H}_2\text{O}$ , technical grade, Sigma-Aldrich), silica gel (pore size  $60\text{\AA}$ , 220–440 mesh particle size, 35–75  $\mu\text{m}$  particle size, for flash chromatography, Sigma-Aldrich), sodium hydroxide (97%, Dinâmica Química Contemporânea Ltda.), 2,2':6',2''-terpyridine (tpy, 98%, Sigma Aldrich) were received and used without further purification. Acetonitrile, chloroform, diethyl ether, hydrochloric acid and methanol were purchased from Labsynth. TLC plates (ALUGRAM XTRA SIL G, Macherey-Nagel) were used to assess the best eluent for column chromatography. Absolute ethanol was purchased from Merck and stored in molecular sieves. N,N'-dimethylformamide (DMF, HPLC grade,  $\geq 99.9\%$ ) for synthesis was purchased from Sigma-Aldrich. Methanol (HPLC/Spectrophotometric grade,  $\geq 99.9\%$ ) for mass spectrometry measurements was purchased from Tedia Brazil. Molecular sieves ( $4\text{\AA}$ , beads, 4–8 mesh, Sigma-Aldrich) were used for drying organic solvents for further measurements. The Ru(II) chlorido complexes were synthesized by using an alternative route to a synthetic procedure reported in literature.<sup>46</sup>

#### 3.2 Measurements

#### 3.3 Synthesis of $\text{Ru}^{\text{III}}(\text{tpy})\text{Cl}_3$

The complex  $\text{Ru}^{\text{III}}(\text{tpy})\text{Cl}_3$  was prepared according to the reported procedure with minor modifications.<sup>47</sup> To a 250 mL round-bottom flask containing 60 mL of boiling ethanol was added  $\text{RuCl}_3 \cdot 3\text{H}_2\text{O}$  (260 mg, 1 mmol) and refluxed under stirring for 5 minutes. After that, 60 mL of an ethanol solution of tpy (233 mg, 1 mmol) was added dropwise during 3 hours under reflux and vigorous stirring. Once finished, the reaction mixture was left to cool to 25 °C and kept in a refrigerator overnight. The fine dark brown powder appearing was filtered from the brown solution. The product was

washed with ethanol (3 × 15 mL) followed by diethyl ether (3 × 15 mL) and then air-dried until constant mass. Yield: 374 mg, 85%. **Elemental analysis** for  $C_{15}H_{11}N_3Cl_3Ru \cdot H_2O$ , Calculated (%): C, 39.28; H, 2.85; N, 9.16. Found (%): C, 38.71; H, 2.81; N, 8.93. **ESI-MS (CH<sub>3</sub>CN)** m/z: 404.9 [M-Cl]<sup>+</sup>.

### 3.4 Synthesis of *cis*-[Ru<sup>II</sup>(Himpy)(tpy)(Cl)]PF<sub>6</sub>

To a 250 mL round-bottom flask containing Ru(tpy)Cl<sub>3</sub> (440 mg, 1.0 mmol) dissolved in DMF (75 mL), lithium chloride (210 mg, 5.0 mmol), ascorbic acid (180 mg, 1.0 mmol), and a DMF solution (75 mL) of Himpy (150 mg, 1.03 mmol) were added. The reaction was heated at 140 °C and kept under stirring for 1 hour. After the completion of the reaction, the solvent was removed under reduced pressure on a rotary-evaporator. Then ethanol (40 mL) was used to dissolve the solid remaining in the round-bottom flask and added to an aqueous solution of NH<sub>4</sub>PF<sub>6</sub> (2 g, 20 mL). Ethanol was removed under reduced pressure giving a dark red solution, which was then filtered affording a dark brown solid and washed with cold water to remove the remaining NH<sub>4</sub>PF<sub>6</sub>. The major product (R<sub>f</sub> = 0.60) was obtained from column chromatography by using silica gel as stationary phase and methanol/chloroform (1:5) as eluent. Finally, the solid was placed in a vacuum oven at 60 °C for 6 hours and then kept in a desiccator. Mass yield: 160 mg (24 %). **Elemental analysis** for  $C_{23}H_{18}N_6ClPF_6Ru \cdot H_2O$ , Calculated (%): C, 40.73; H, 2.95; N, 12.40. Found (%): C, 40.79; H, 3.48; N, 12.76. **<sup>1</sup>H-NMR (400 MHz, DMSO-d<sub>6</sub>)**: δ/ppm 14.41 (s, 1H), 8.77 (d, 2H, J = 7.8 Hz), 8.66 (d, 2H, J = 8.0 Hz), 8.16 (d, 1H, J = 1.2 Hz), 8.12 (d, 1H, J = 8.0 Hz), 8.11 (t, 1H, J = 8 Hz), 8.04 (d, 1H, J = 1.2 Hz), 7.96 (td, 2H, J = 7.8, 1.4 Hz), 7.72 (d, 2H, J = 4.8 Hz), 7.71 (td, 1H, J = 7.8, 1.2 Hz), 7.43 (ddd, 2H, J = 7.7, 5.6, 1.2 Hz), 7.04 (d, 1H, J = 5.6 Hz), 6.89 (ddd, 1H, J = 7.9, 5.8, 1.2 Hz). **ESI-MS (MeOH)** m/z: 515.0 [Ru(Himpy)(tpy)(Cl)]<sup>+</sup>. **UV-Vis [(λ<sub>max</sub>, nm (ε, 10<sup>3</sup> M<sup>-1</sup> cm<sup>-1</sup>) in EtOH]**: 233 (17,5), 278 (14,9), 319 (22,7), 404 (4,1), 508 (3,8).

### 3.5 Synthesis of *trans*-[Ru<sup>II</sup>(Himpy)(tpy)(Cl)]PF<sub>6</sub>

The minor product (R<sub>f</sub> = 0.67) was obtained from column chromatography by using silica gel as stationary phase and methanol/chloroform (1:5) as eluent. The

solid was placed in a vacuum oven at 60 °C for 6 hours and then kept in a desiccator. Mass yield: 10 mg (1.5 %). **<sup>1</sup>H-NMR (250 MHz, CD<sub>3</sub>OD)**: δ/ppm 10.07 (d, 1H, J = 5.6 Hz), 8.58 (d, 2H, J = 8.1 Hz), 8.48 (d, 2H, J = 7.9 Hz), 8.28 (m, 1H), 8.27 (m, 1H), 8.06 (t, 1H, J = 8 Hz), 7.90 (m, 3H), 7.78 (d, 2H, J = 5.3 Hz), 7.34 (t, 2H, J = 6.6 Hz), 7.10 (s, 1H), 6.07 (s, 1H). **UV-Vis [(λ<sub>max</sub>, nm (ε, 10<sup>3</sup> M<sup>-1</sup> cm<sup>-1</sup>) in EtOH]**: 235 (38,5), 278 (32,3), 322 (42,6), 379 (9,3), 514 (8,4).

### 3.6 Synthesis of *cis*-[Ru<sup>II</sup>(Himpa)(tpy)(Cl)]PF<sub>6</sub>

The procedure followed for this reaction was like that described for the *cis*-[Ru<sup>II</sup>(Himpy)(tpy)(Cl)]PF<sub>6</sub> complex. Ru(tpy)Cl<sub>3</sub> (286 mg, 0.65 mmol) dissolved in DMF (50 mL), lithium chloride (136 mg, 3.25 mmol), ascorbic acid (118 mg, 0.65 mmol), and a DMF solution (50 mL) of Himpa (98.6 mg, 0.67 mmol) were used. The pure product (R<sub>f</sub> = 0.67) was obtained from column chromatography by using silica gel as stationary phase and methanol/chloroform (1:4) as eluent. Mass yield: 165 mg (38 %). **Elemental analysis** for C<sub>22</sub>H<sub>17</sub>N<sub>7</sub>ClPF<sub>6</sub>Ru, Calculated (%): C, 39.98; H, 2.59; N, 14.84. Found (%): C, 40.23; H, 2.51; N, 14.5. **<sup>1</sup>H-NMR (400 MHz, DMSO-d<sub>6</sub>)**: δ/ppm 14.68 (s, 1H), 8.70 (d, 2H, J = 8.0 Hz), 8.62 (d, 2H, J = 8.0 Hz), 8.45 (dd, 1H, J = 5.0, 1.8 Hz), 8.29 (dd, 1H, J = 8.4, 1.8 Hz), 8.24 (d, 1H, J = 1.2 Hz), 8.12 (t, 1H, J = 8.0 Hz), 8.06 (d, 1H, J = 1.2 Hz), 7.98 (td, 2H, J = 7.8, 1.4 Hz), 7.71 (dd, 2H, J = 5.4, 0.7 Hz), 7.47 (dd, 1H, J = 8.5, 5.0 Hz), 7.43 (ddd, 2H, J = 7.9, 5.6, 1.2 Hz). **ESI-MS (MeOH) m/z**: 515.8 [Ru(Himpa)(tpy)(Cl)]<sup>+</sup>. **UV-Vis [(λ<sub>max</sub>, nm (ε, 10<sup>3</sup> M<sup>-1</sup> cm<sup>-1</sup>) in EtOH]**: 229 (12,8), 279 (9,5), 317 (15,8), 370 (sh, 3,0), 442 (3,2), 498 (3,7), 528 (sh, 3,5).

### 3.7 Synthesis of *cis*-[Ru<sup>II</sup>(Himpz)(tpy)(Cl)]Cl

The procedure followed for this reaction was slightly different from that described for the *cis*-[Ru<sup>II</sup>(Himpy)(tpy)(Cl)]PF<sub>6</sub> complex. Ru(tpy)Cl<sub>3</sub> (100 mg, 0.22 mmol), lithium chloride (48 mg, 1.1 mmol), Himpz (66.0 mg, 0.44 mmol), and ascorbic acid (20 mg, 0.11 mmol), in that order, were added to a 50 mL round-bottom flask containing 15 mL of DMF and left at 110 °C under stirring. After 3 h, the mixture reaction was placed in a rotary evaporator to remove the solvent, followed by dissolving the solid in 10 mL of methanol. The resulting mixture was filtered and washed three times

with hot methanol. The filtrate was further used for purification and isolation of the components. The major product ( $R_f = 0.37$ ) was obtained from column chromatography by using silica gel as stationary phase and methanol/chloroform (1:3) as eluent. Height and diameter of silica used for column chromatography: 15 and 3 cm. Mass yield: 58 mg (47 %).  **$^1\text{H-NMR}$  (250 MHz,  $\text{DMSO-d}_6$ ):**  $\delta$ /ppm 9.16 (s, 1H), 8.78 (d, 2H,  $J = 8.1$  Hz), 8.67 (d, 2H,  $J = 8.0$  Hz), 8.24 (s, 1H), 8.18 (t, 1H,  $J = 8.2$  Hz), 8.04 (s, 1H), 8.01 (t, 2H,  $J = 7.9$  Hz), 7.93 (d, 1H,  $J = 3.4$  Hz), 7.65 (d, 2H,  $J = 5.1$  Hz), 7.44 (t, 2H,  $J = 6.6$  Hz), 7.36 (d, 1H,  $J = 3.2$  Hz). **UV-Vis** [ $\lambda_{\text{max}}$ , nm ( $\epsilon$ ,  $10^3 \text{ M}^{-1} \text{ cm}^{-1}$ ) in EtOH]: 232 (26,6), 277 (19,5), 316 (30,2), 353 (9,8), 447 (5,5), 513 (7,8).

### 3.8 Synthesis of *trans*-[Ru<sup>II</sup>(Himpz)(tpy)(Cl)]Cl

The minor product ( $R_f = 0.53$ ) was obtained from column chromatography by using silica gel as stationary phase and methanol/chloroform (1:3) as eluent. The solid was placed in a vacuum oven at 60 °C for 6 hours and then kept in a desiccator. Mass yield: 19 mg (15 %).  **$^1\text{H-NMR}$  (250 MHz,  $\text{DMSO-d}_6$ ):**  $\delta$ /ppm 9.89 (dd, 1H,  $J = 3.5$ , 1.1 Hz), 9.60 (s, 1H), 8.83 (d, 1H,  $J = 3.3$  Hz), 8.76 (d, 2H,  $J = 8.1$  Hz), 8.63 (d, 2H,  $J = 8.1$  Hz), 8.11 (t, 1H,  $J = 8.1$  Hz), 7.92 (td, 2H,  $J = 7.8$ , 1.2 Hz), 7.77 (dd, 2H,  $J = 5.6$ , 0.7 Hz), 7.34 (ddd, 2H,  $J = 7.4$ , 5.7, 1.0 Hz), 7.06 (s, 1H), 5.94 (s, 1H).

### 3.9 Synthesis of *cis*-[Ru<sup>II</sup>(Himpm)(tpy)(Cl)]Cl

The procedure followed for this reaction was like that described for the *cis*-[Ru<sup>II</sup>(Himpz)(tpy)(Cl)]Cl complex. Ru(tpy)Cl<sub>3</sub> (100 mg, 0.22 mmol), lithium chloride (48 mg, 1.1 mmol), Himpm (66.0 mg, 0.44 mmol), and ascorbic acid (20 mg, 0.11 mmol), in that order, were added to a 50 mL round-bottom flask containing 15 mL of DMF and left at 110 °C under stirring for 3 h. The major product ( $R_f = 0.37$ ) was obtained from column chromatography by using silica gel as stationary phase and methanol/chloroform (1:3) as eluent. Height and diameter of silica used for column chromatography: 15 and 3 cm. Mass yield: 75 mg (60 %).  **$^1\text{H-NMR}$  (500 MHz,  $\text{DMSO-d}_6$ ):**  $\delta$  14.92 (s, 1H), 8.80 (d, 2H,  $J = 8.1$  Hz), 8.69 (d, 2H,  $J = 8.1$  Hz), 8.62 (dd, 1H,  $J = 4.7$ , 1.9 Hz), 8.17 (d, 1H,  $J = 1.1$  Hz), 8.14 (t, 1H,  $J = 8.1$  Hz), 8.08 (d, 1H,  $J = 1.2$  Hz), 7.99 (td, 2H,  $J = 7.8$ , 1.4 Hz), 7.75 (dd, 2H,  $J = 5.4$ , 0.6 Hz), 7.48 (dd, 1H,  $J = 5.9$ ,

1.9 Hz), 7.45 (ddd, 2H,  $J = 7.4, 5.5, 1.2$  Hz), 6.96 (dd, 1H,  $J = 5.8, 4.8$  Hz). **UV-Vis** [ $\lambda_{\max}$ , nm ( $\epsilon$ ,  $10^3 \text{ M}^{-1} \text{ cm}^{-1}$ ) in EtOH]: 231 (26,7), 276 (22,6), 316 (35,3), 371 (9,8), 420 (6,0), 501 (6,5).

### 3.10 Synthesis of *trans*-[Ru<sup>II</sup>(Himp<sub>m</sub>)(tpy)(Cl)]Cl

The minor product ( $R_f = 0.53$ ) was obtained from column chromatography by using silica gel as stationary phase and methanol/chloroform (1:3) as eluent. The solid was placed in a vacuum oven at 60 °C for 6 hours and then kept in a desiccator. Mass yield: 18 mg (14 %). **<sup>1</sup>H-NMR (250 MHz, DMSO-*d*<sub>6</sub>)**:  $\delta$ /ppm 10.06 (dd, 1H,  $J = 5.7, 2.1$  Hz), 9.10 (dd, 1H,  $J = 4.7, 2.1$  Hz), 8.74 (d, 2H,  $J = 8.0$  Hz), 8.63 (d, 2H,  $J = 8.0$  Hz), 8.08 (t, 1H,  $J = 7.9$  Hz), 7.93 (td, 2H,  $J = 7.7, 1.2$  Hz), 7.85 (m, 3H), 7.38 (ddd, 2H,  $J = 7.2, 5.6, 1.2$  Hz), 7.07 (s, 1H), 5.96 (s, 1H). **UV-Vis** [ $\lambda_{\max}$ , nm ( $\epsilon$ ,  $10^3 \text{ M}^{-1} \text{ cm}^{-1}$ ) in EtOH]: 231 (18,6), 277 (15,6), 320 (22,3), 386 (5,4), 512 (4,7).

## 4. RESULTS AND DISCUSSION

### 4.1 Synthesis and characterization of the ruthenium complexes

Reaction of starting complex Ru(tpy)Cl<sub>3</sub> with heteroaryl-2-imidazole ligands (Himp<sub>x</sub> = Him<sub>p</sub>, Him<sub>a</sub>, Him<sub>m</sub> and Him<sub>p</sub>z), using ascorbic acid to reduce Ru<sup>III</sup> to Ru<sup>II</sup> and lithium chloride in excess to guarantee the chlorido as the axial ligand, did not afford exclusively one product (**Figure 3a**), as observed after performing a TLC (thin layer chromatography) test on the reaction products using methanol/chloroform (1:5) as eluent. Regarding the ruthenium complexes containing the Him<sub>p</sub> and Him<sub>p</sub>z ligands, three spots were observed in TLC plates whereas in Him<sub>a</sub>-ruthenium complex two spots were displayed. In all cases, a fast-running product appearing at  $R_f = 0.83$  was observed (**Figure 3b**), which led to think about the possibility of a ruthenium complex containing only the terpyridine ligand. A first attempt was to consider the precursor Ru(tpy)Cl<sub>3</sub> that could not react at all, and a conductivity measurement in acetonitrile was performed on that fast-running compound, obtained after performing column chromatography, giving a molar conductivity value of  $1.50 \text{ S cm}^2 \text{ mol}^{-1}$  which was assigned to be a neutral compound (**Figure 3c**).<sup>48</sup>

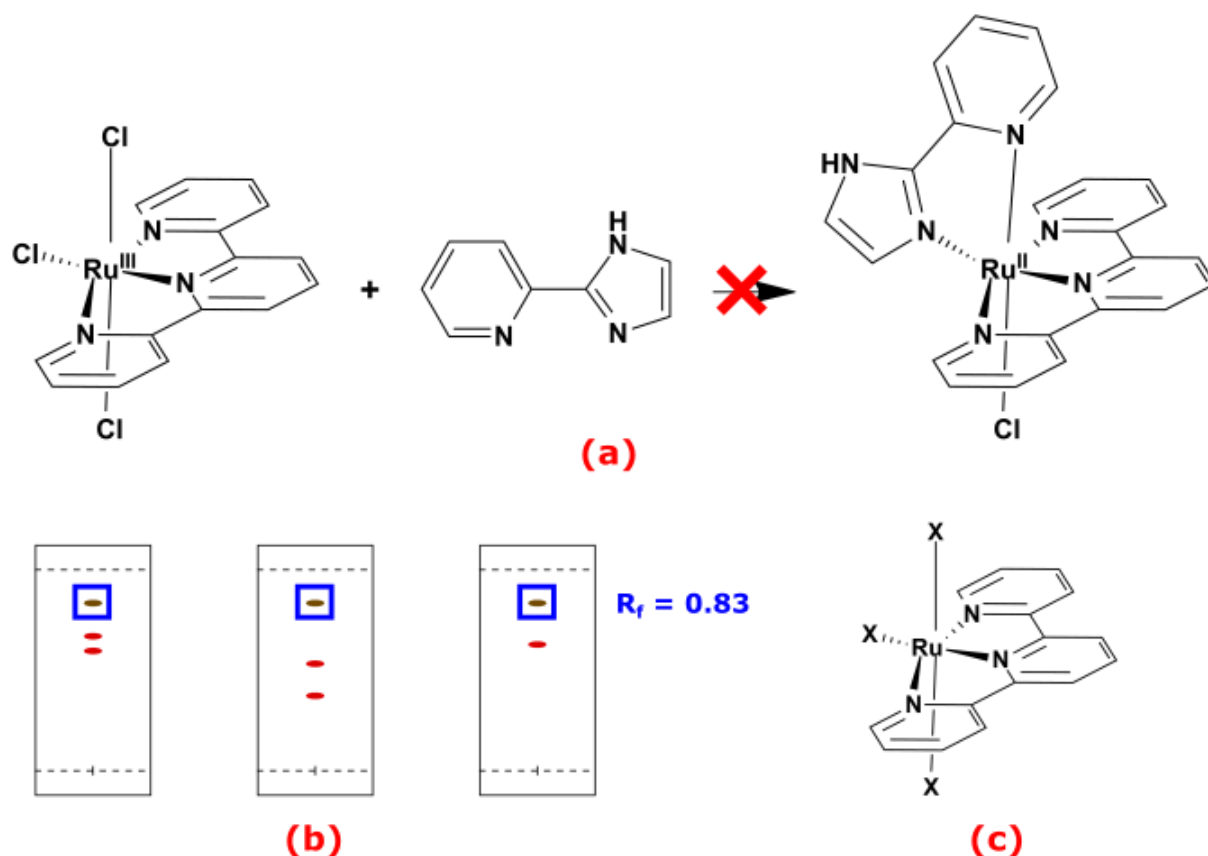


**Figure 3.** (a) Unsuccessful attempt to obtain one isomer exclusively. (b) TLC plates performed on the reaction products showing the formation of more than one compound. (c) Possible fast-running compound appearing in all reaction synthesis.

For comparison purposes, the molar conductivity in acetonitrile of neutral complex  $\text{Ru}(\text{tpy})\text{Cl}_3$  was found to be  $4.50 \text{ S cm}^2 \text{ mol}^{-1}$ . The next step was to acquire the UV-visible spectra of both samples to compare them and check if they were the same compound. **Figure 4** shows similarities in the region 200–350 nm but some differences in the visible region, which led to assume they were related but not the same compounds.

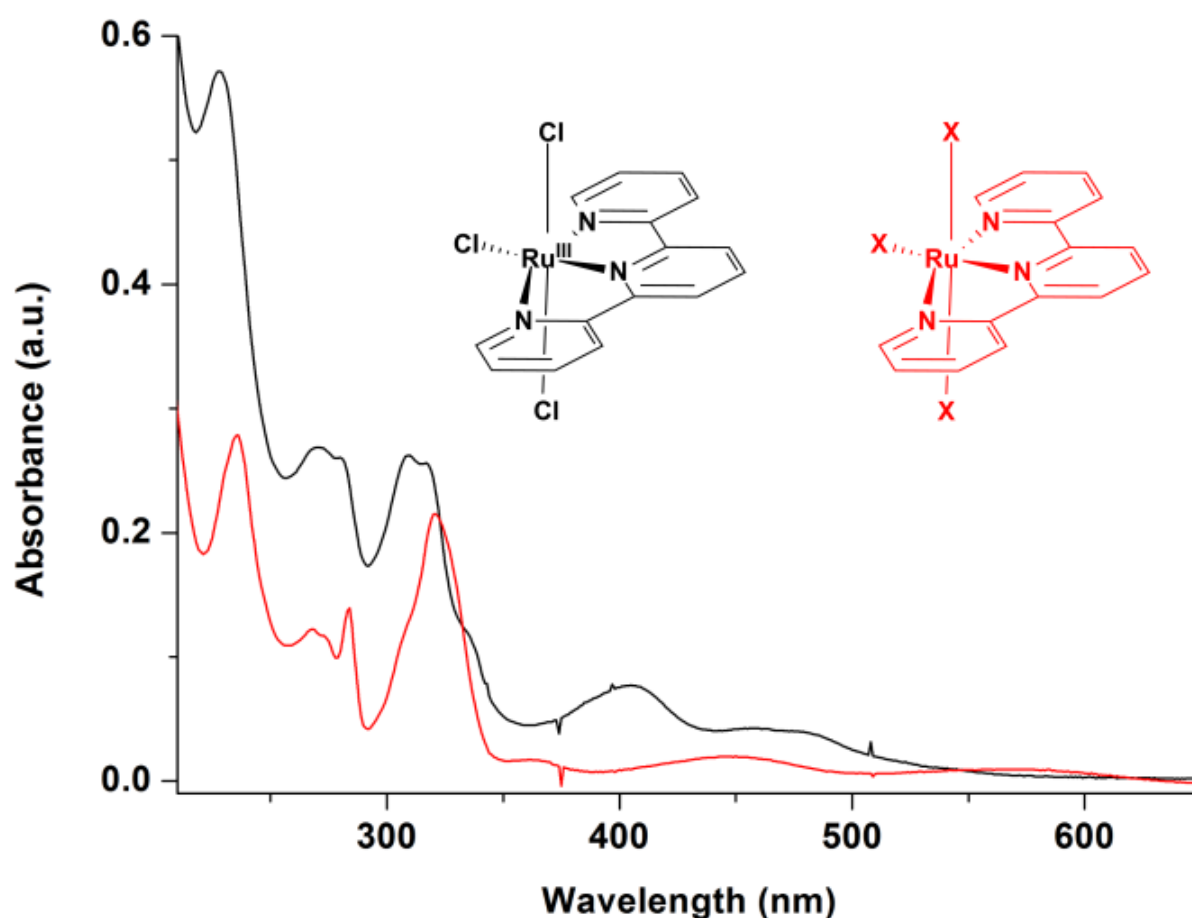


**Figure 4.** UV-visible spectra of Ru(tpy)Cl<sub>3</sub> and the unknown product in acetonitrile.

The <sup>1</sup>H-NMR spectrum of the unknown compound acquired in DMSO-d<sub>6</sub> (**Figure 5**) displays six signals which, after analysis of the coupling constants, multiplicities, and integrations, were attributed to the terpyridine protons. This was not the only information obtained from the spectrum, but also the shape of the narrow, well defined signals that were consistent with a diamagnetic nature of the compound which is related to the Ru(II) species. With all this information, the composition of the compound was found to be [Ru<sup>II</sup>(tpy)(Cl)<sub>2</sub>(X)], being X a neutral ligand.

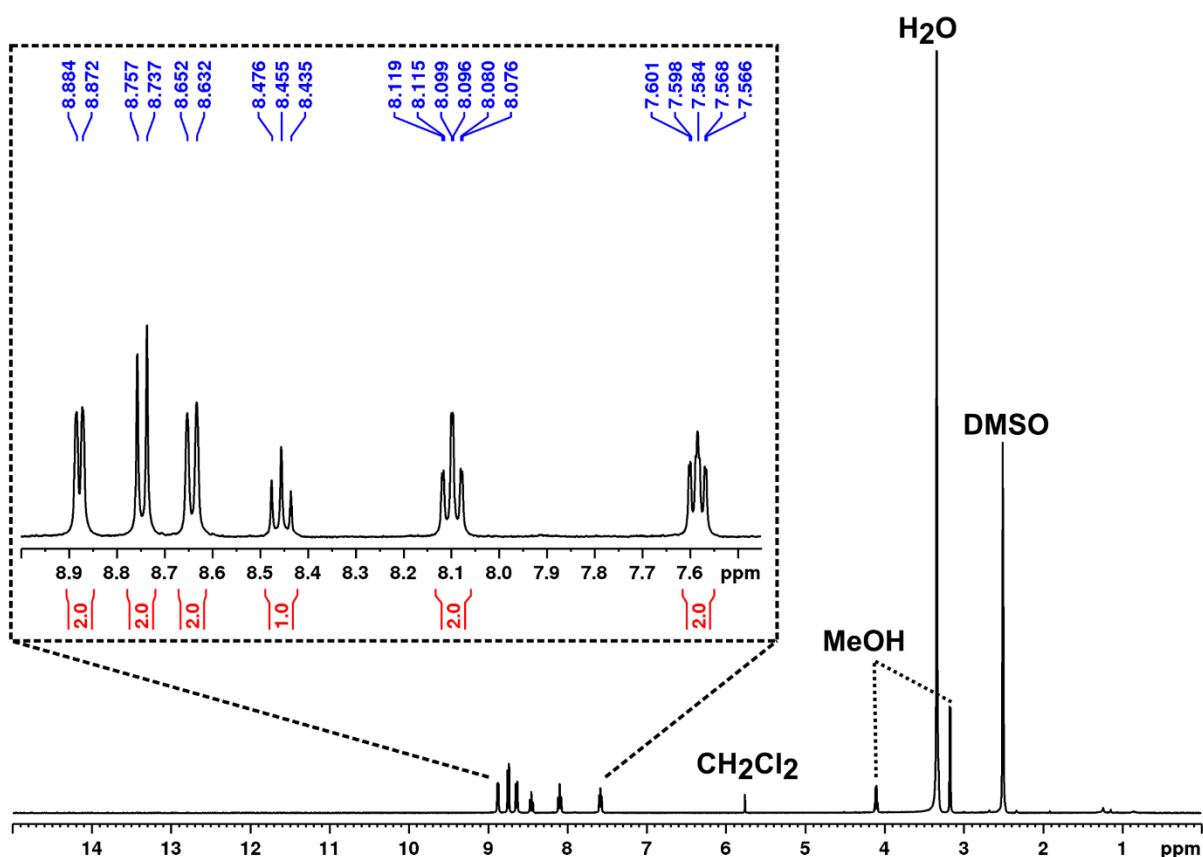


**Figure 5.**  $^1\text{H-NMR}$  spectrum of the unknown compound in  $\text{DMSO-d}_6$  at 400 MHz.

The structure of this unknown compound was finally elucidated by means of X-ray crystallography after analyzing some crystals obtained through slow evaporation from its acetonitrile solution which was kept at 298 K for several days. **Figure 6** shows a ruthenium complex containing a terpyridine moiety in a meridional fashion, with two chloridos in *trans* position to each other and a carbonyl ligand in *trans* position to the terpyridine ring, which could probably arise from the decomposition of the dimethylformamide solvent used in the synthesis. This result was not unexpected as some works related the synthesis of carbonyl-containing complexes with DMF as a source of the carbonyl ligand.<sup>49,50</sup>

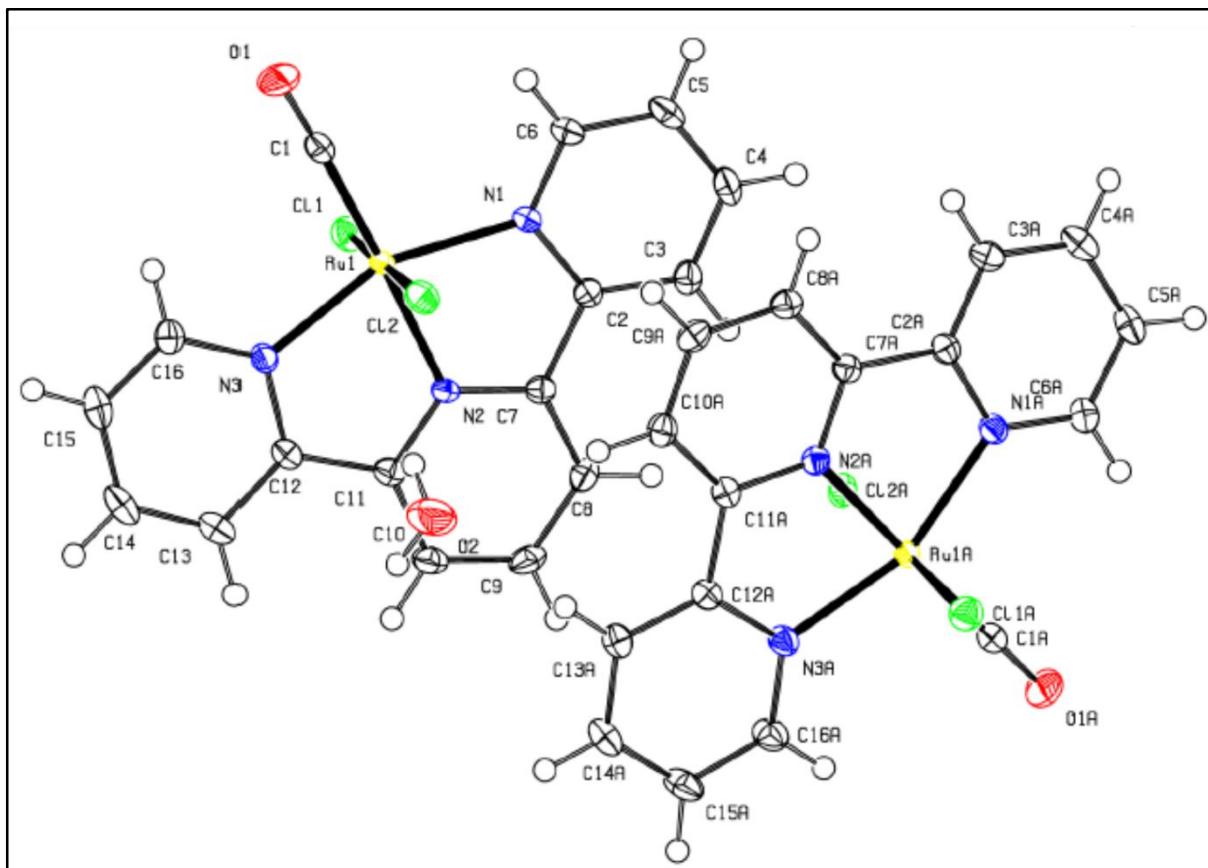


**Figure 6.** ORTEP diagram of the unknown compound at 150 K. The numbering is different from that used for  $^1\text{H-NMR}$  assignments (next sections). Atoms are colored as follows: Carbon (soft gray), nitrogen (blue), hydrogen (white), oxygen (red), ruthenium (teal), chlorine (green).

The other two compounds found in the TLC plates, after performing column chromatography and further characterization, were found to be the *cis* and *trans* isomers (**Figure 7**), with exception of the Himpa-bearing ruthenium complex, which will be described in the next sections. In general, all these complexes were soluble in dimethyl sulfoxide, N,N-dimethylformamide, acetonitrile, methanol, and ethanol, sparingly soluble in water, acetone, and dichloromethane, and practically insoluble in chloroform, ethyl acetate and diethyl ether.

Constable *et al.*<sup>51</sup> reported some mononuclear ruthenium complexes containing a terpyridine and derivatives of bipyridine ligand that were obtained in *cis* and *trans* conformations. The authors showed that one conformation could be preferentially formed by using a suitable solvent. In this Thesis, the synthesis was performed in ethanol, methanol, and water without any success in obtaining exclusively one isomer. Furthermore, the products were achieved in low yields because of the low solubility of the starting complex  $\text{Ru}(\text{tpy})\text{Cl}_3$  in these solvents. No attempt was made in

acetonitrile, despite it shows a good solubility, as this solvent is a potential ligand which could replace the chlorido ligand in the coordination sphere.<sup>52</sup>

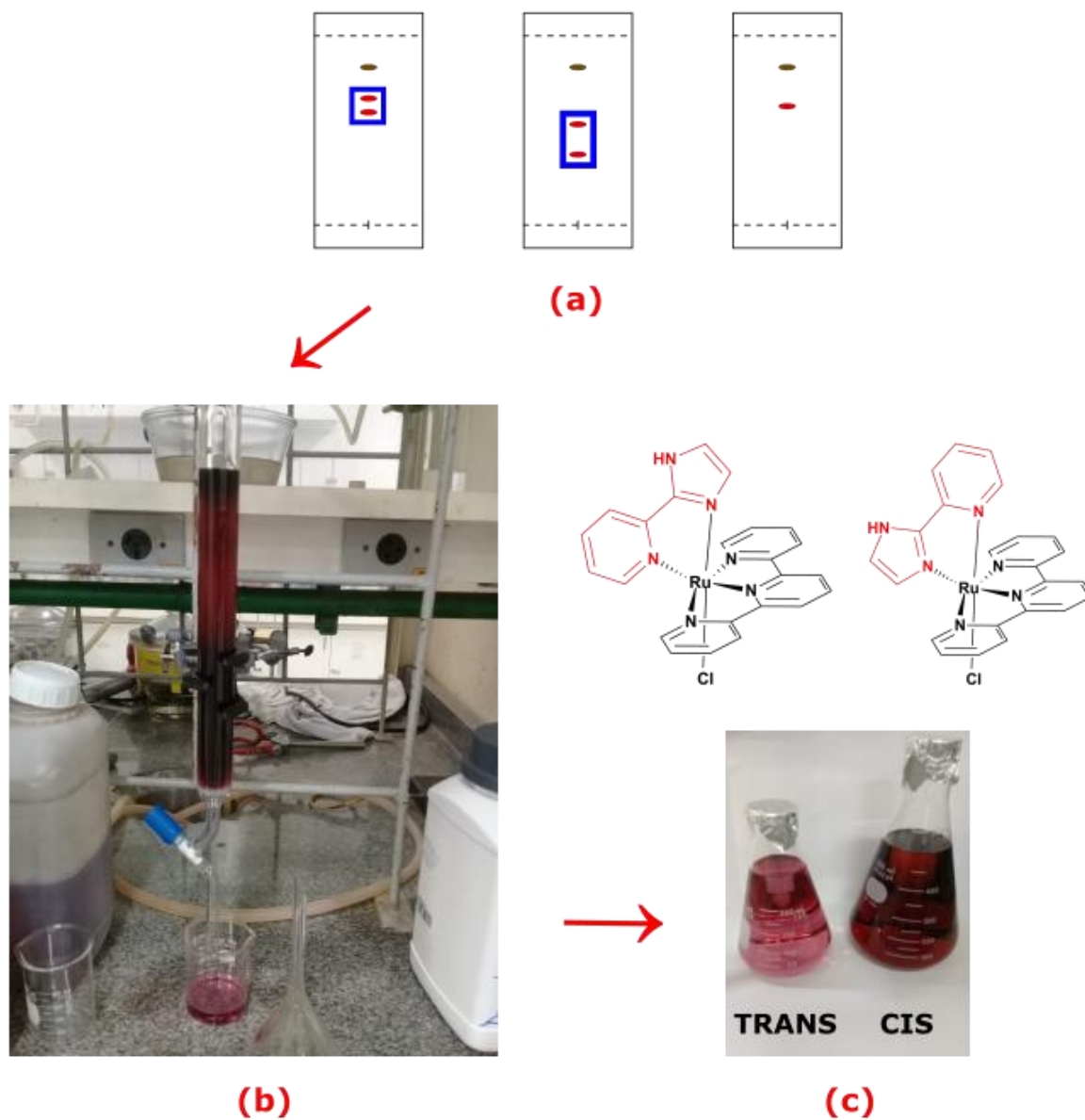


**Figure 7.** (a) TLC plates showing the cis and trans isomers. (b) Column chromatography performed on the reaction products. (c) The cis and trans isomers isolated after performing column chromatography.

#### 4.2 <sup>1</sup>H-NMR Spectroscopy

In the synthesis of the ruthenium chlorido complex bearing the Himpy ligand, two isomers (axial ligand in *cis* and *trans* position with respect to imidazole

moiety) were obtained despite the several attempts to obtain one of them selectively by means of different temperature, solvents, and reaction times. The  $^1\text{H-NMR}$  spectra of complex isomers  $\text{cis-}[\text{Ru}^{\text{II}}(\text{Himpy})(\text{tpy})(\text{Cl})]^+$  and  $\text{trans-}[\text{Ru}^{\text{II}}(\text{Himpy})(\text{tpy})(\text{Cl})]^+$  in  $\text{CD}_3\text{OD}$  are shown in **Figure 8**. The spectra display one set of six signals for the terpyridine moiety, evidencing its symmetry in the complex, four signals due to the pyridine group and 2 singlet signals arising from imidazole group, being the N–H proton signal absent in both spectra because of the fast chemical exchange with water from solvent. This phenomenon is also responsible for the characteristic singlet signal for imidazole protons.<sup>27</sup> Terpyridine protons chemical shifts remain almost constant in both complexes, but what makes their spectra different to each other is the downfield shift of the pyridine protons in the *cis*-complex and the upfield shift of the imidazole protons in the *trans*-complex that reflects the shielding effect of the diamagnetic anisotropy exerted by terpyridine ring, which is perpendicular and *trans*-positioned to the favored ring. Chemical shifts of the imidazole protons, which are *cis* and *trans* to the terpyridine ring, are in well agreement with literature data.<sup>53</sup> The assignments of all protons were made through use of characteristic chemical shifts and proton–proton coupling constants ( $J$ ) for heterocyclic aromatic compounds. Chemical shifts, coupling constants, multiplicities and integrations are summarized in **Table 3**.

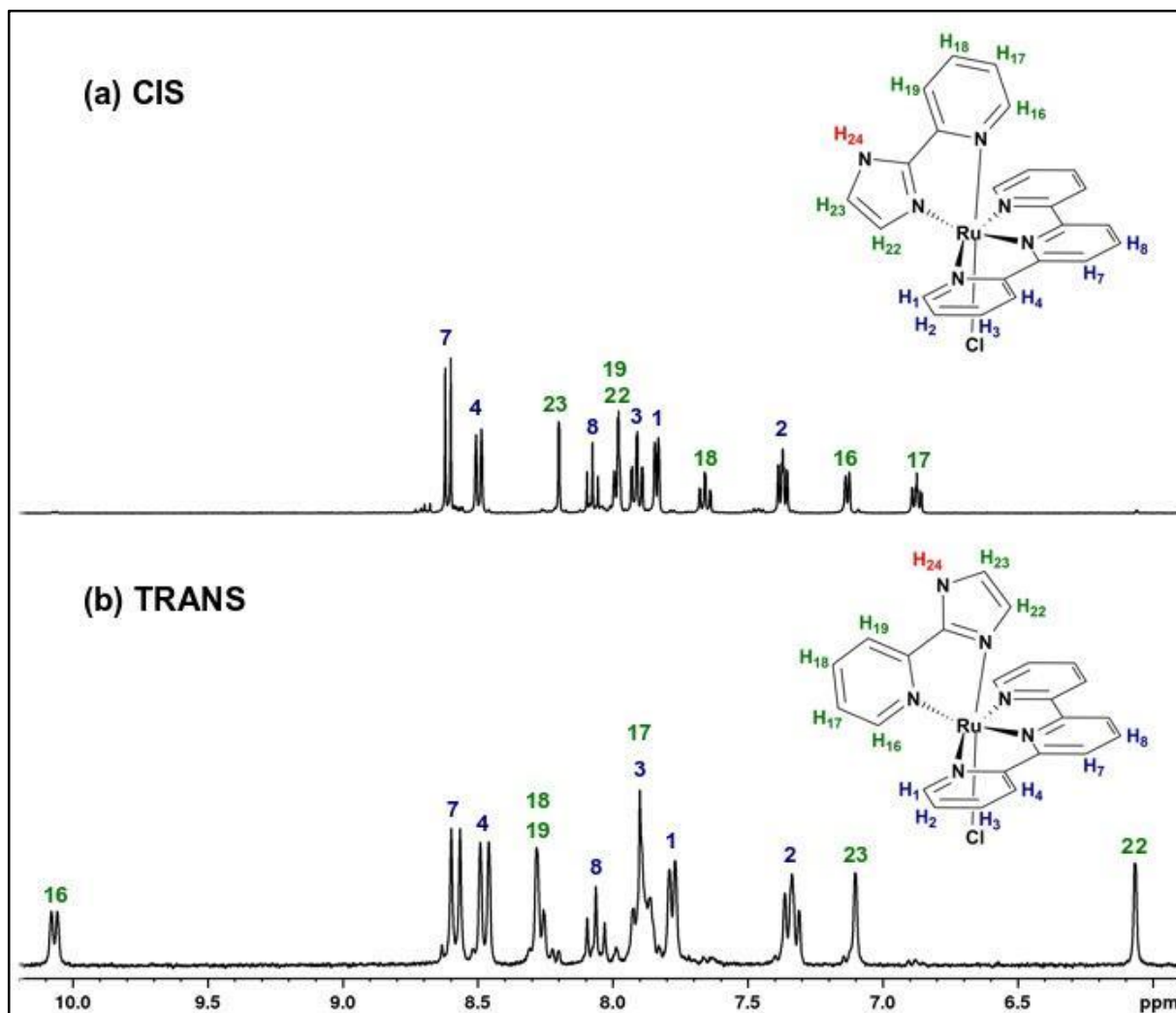


**Figure 8.**  $^1\text{H-NMR}$  spectra of (a)  $\text{cis-}[\text{Ru}^{\text{II}}(\text{Himpy})(\text{tpy})(\text{Cl})]^+$  and (b)  $\text{trans-}[\text{Ru}^{\text{II}}(\text{Himpy})(\text{tpy})(\text{Cl})]^+$  complexes recorded in  $\text{CD}_3\text{OD}$  at 250 MHz.

**Table 3.**  $^1\text{H-NMR}$  data for  $cis\text{-}[\text{Ru}^{\text{II}}(\text{Himpy})(\text{tpy})(\text{Cl})]^+$  and  $trans\text{-}[\text{Ru}^{\text{II}}(\text{Himpy})(\text{tpy})(\text{Cl})]^+$  complexes recorded in  $\text{CD}_3\text{OD}$ .

Compound	Hydrogen	Splitting pattern	Integration	Chemical shift (ppm)	Coupling constant (Hz)
CIS	7	d	2	8.61	8.1
	4	d	2	8.49	8.1
	23	d	1	8.20	1.4
	8	t	1	8.08	8.1
	19	d	1	7.99	6.4
	22	d	1	7.98	1.4
	3	td	2	7.91	7.8, 1.5
	1	d	2	7.84	5.5
	18	td	1	7.66	7.8, 1.4
	2	ddd	2	7.37	7.6, 5.6, 1.2
	16	d	1	7.13	5.6
	17	ddd	1	6.87	7.7, 5.8, 1.4
TRANS	16	d	1	10.07	5.6
	7	d	2	8.58	8.1
	4	d	2	8.48	7.9
	18	m	1	8.28	-
	19	m	1	8.27	-
	8	t	1	8.06	8.0
	17	m	1	7.90	-
	3	m	2	7.90	-
	1	d	2	7.78	5.3
	2	t	2	7.34	6.6
	23	s	1	7.10	-
	22	s	1	6.07	-

Similar to the synthesis of  $[\text{Ru}^{\text{II}}(\text{Himpy})(\text{tpy})(\text{Cl})]\text{PF}_6$ , two isomers were obtained in the synthesis of the ruthenium chlorido complex containing the Himpz ligand. The  $^1\text{H-NMR}$  spectra of complex isomers  $cis\text{-}[\text{Ru}^{\text{II}}(\text{Himpz})(\text{tpy})(\text{Cl})]^+$  and  $trans\text{-}[\text{Ru}^{\text{II}}(\text{Himpz})(\text{tpy})(\text{Cl})]^+$  in  $\text{DMSO-d}_6$  are shown in **Figure 9**. Both spectra show six signals for the terpyridine moiety, three signals related to the pyrazine group, and two singlet signals arising from the imidazole group. The N–H proton signal was absent in both spectra because of the fast chemical exchange with water arising from the deuterated solvent. Again, the significant difference between these spectra is the downfield shift of the pyrazine protons in the *cis*-complex and the large upfield shift of the imidazole protons in the *trans*-complex that reflects the shielding effect of the diamagnetic anisotropy exerted by terpyridine ring. Chemical shifts, coupling constants, multiplicities, and integrations are summarized in **Table 4**.

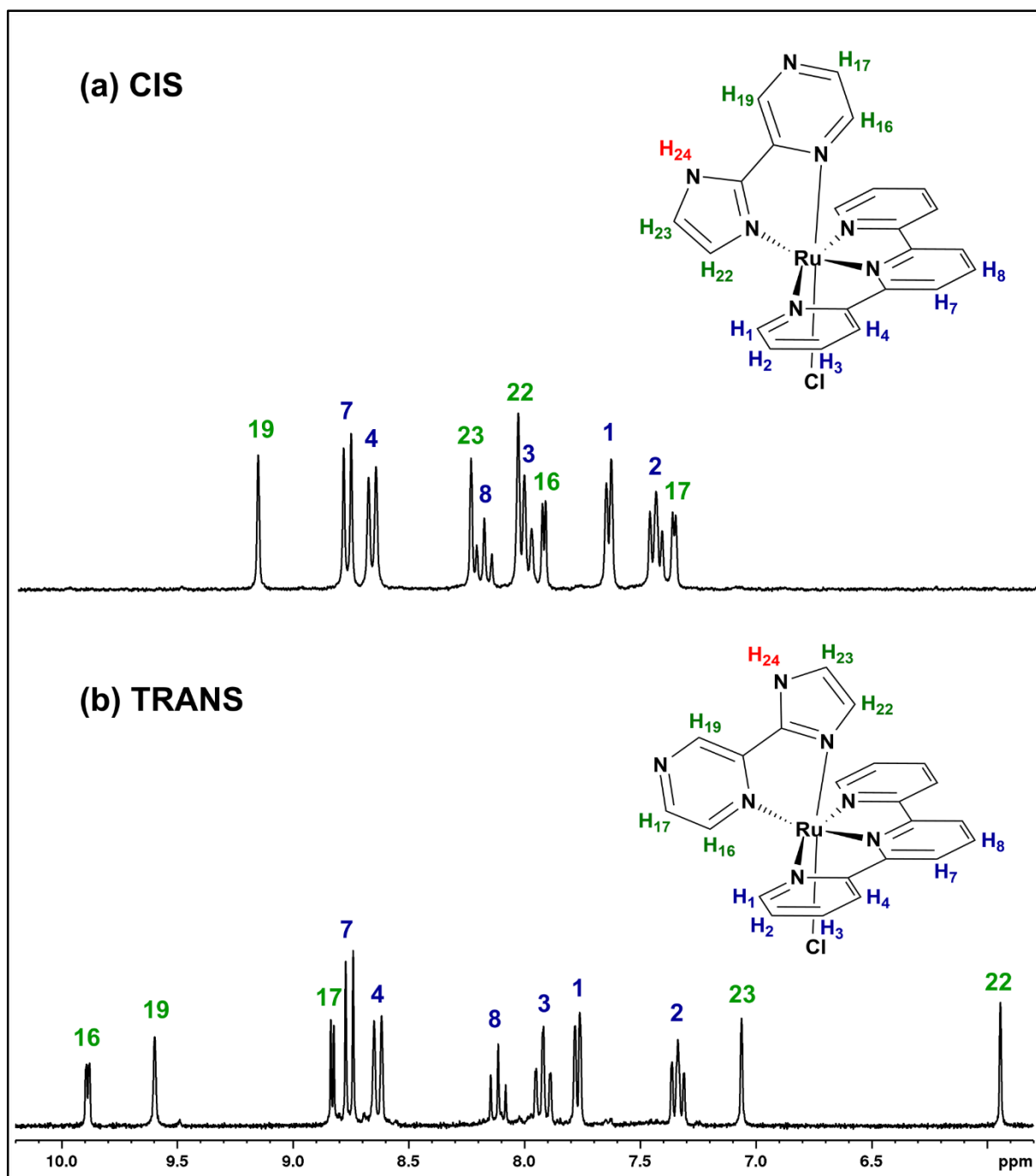


**Figure 9.**  $^1\text{H-NMR}$  spectra of (a)  $\text{cis-}[\text{Ru}^{\text{II}}(\text{Himpz})(\text{tpy})(\text{Cl})]^+$  and (b)  $\text{trans-}[\text{Ru}^{\text{II}}(\text{Himpz})(\text{tpy})(\text{Cl})]^+$  complexes recorded in  $\text{DMSO-d}_6$  at 250 MHz.

**Table 4.**  $^1\text{H-NMR}$  data for  $\text{cis-}[\text{Ru}^{\text{II}}(\text{Himpz})(\text{tpy})(\text{Cl})]^+$  and  $\text{trans-}[\text{Ru}^{\text{II}}(\text{Himpz})(\text{tpy})(\text{Cl})]^+$  complexes recorded in  $\text{DMSO-d}_6$ .

Compound	Hydrogen	Splitting pattern	Integration	Chemical shift (ppm)	Coupling constant (Hz)
CIS	19	S	1	9.16	-
	7	D	2	8.78	8.1
	4	D	2	8.67	8.0
	23	S	1	8.24	-
	8	T	1	8.18	8.2
	22	S	1	8.04	-
	3	T	2	8.01	7.9
	16	D	1	7.93	3.4
	1	D	2	7.65	5.1
	2	T	2	7.44	6.6
	17	D	1	7.36	3.2
TRANS	16	Dd	1	9.89	3.5, 1.1
	19	S	1	9.60	-
	17	D	1	8.83	3.3
	7	D	2	8.76	8.1
	4	D	2	8.63	8.1
	8	T	1	8.11	8.1
	3	Td	2	7.92	7.8, 1.2
	1	Dd	2	7.77	5.6, 0.7
	2	Ddd	2	7.34	7.4, 5.7, 1.0
	23	S	1	7.06	-
22	S	1	5.94	-	

### 4.3 X-ray crystallography

X-ray suitable crystals of  $\text{cis-}[\text{Ru}^{\text{II}}(\text{Himpz})(\text{tpy})(\text{Cl})]\text{PF}_6$  complex were obtained after filtration of its isolated product from column chromatography and kept in an  $\text{NH}_4\text{PF}_6$  aqueous solution, and further analysis confirmed the proposed structure (**Figure 10**). In this structure,  $\text{Ru}(\text{II})$  ion is coordinated to Himpz, tpy, and chlorido ligands in a distorted octahedral geometry. The chlorido ligand is in *cis* position to the imidazole ring of the Himpz ligand, which in turn coordinates in an almost perpendicular fashion ( $95.95^\circ$ ) to the relative planar tpy ring. Crystallographic data for the complex is listed in **Table 5**.

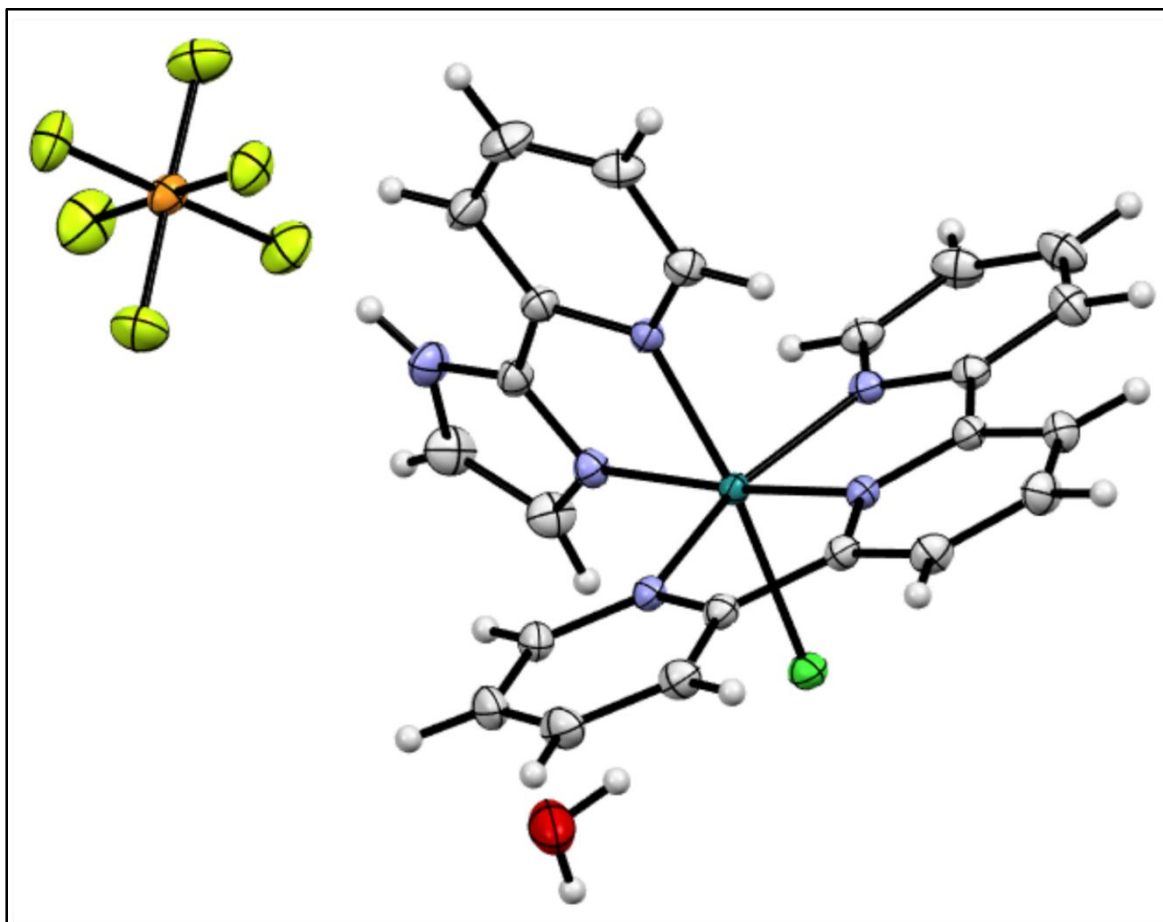


**Figure 10.** ORTEP view of the X-ray structure of *cis*-[Ru<sup>II</sup>(Himpy)(tpy)(Cl)](PF<sub>6</sub>)·H<sub>2</sub>O at 150K. Atoms are colored as follows: Carbon (gray), nitrogen (blue), hydrogen (soft gray), oxygen (red), ruthenium (teal), phosphorous (orange), chlorine (green), fluorine (yellow).

**Table 5.** Crystallographic data for the complex *cis*-[Ru<sup>II</sup>(Himpy)(tpy)(Cl)](PF<sub>6</sub>)·H<sub>2</sub>O.

Parameter	Complex
<b>Empirical formula</b>	C <sub>23</sub> H <sub>20</sub> N <sub>6</sub> ClPF <sub>6</sub> ORu
<b>Fw</b>	677.94
<b>Crystal symmetry</b>	Triclinic
<b>Space group</b>	P -1
<b>a (Å)</b>	8.844(2)
<b>b (Å)</b>	10.040(3)
<b>c (Å)</b>	15.920(4)
<b>α (°)</b>	78.168(5)
<b>β (°)</b>	77.112(5)
<b>γ (°)</b>	64.995(5)
<b>V (Å<sup>3</sup>)</b>	1239.0(7)
<b>Z</b>	2
<b>T (K)</b>	150

After isolating the *trans*-[Ru<sup>II</sup>(Himpy)(tpy)(Cl)]PF<sub>6</sub> isomer and analyzing it employing <sup>1</sup>H-NMR spectroscopy, the next step was trying to confirm its proposed structure. Crystals were obtained from slow evaporation of the fractions collected from column chromatography. **Figure 11** shows a distorted octahedral complex with the terpyridine in the meridional position and the imidazole ring in *trans* position to the chlorido ligand, confirming the previously proposed conformation. There is also a chloroform molecule present in the structure which arose from the methanol/chloroform mixture used for eluting the fractions of column chromatography. Crystallographic data for the complex is listed in **Table 6**.

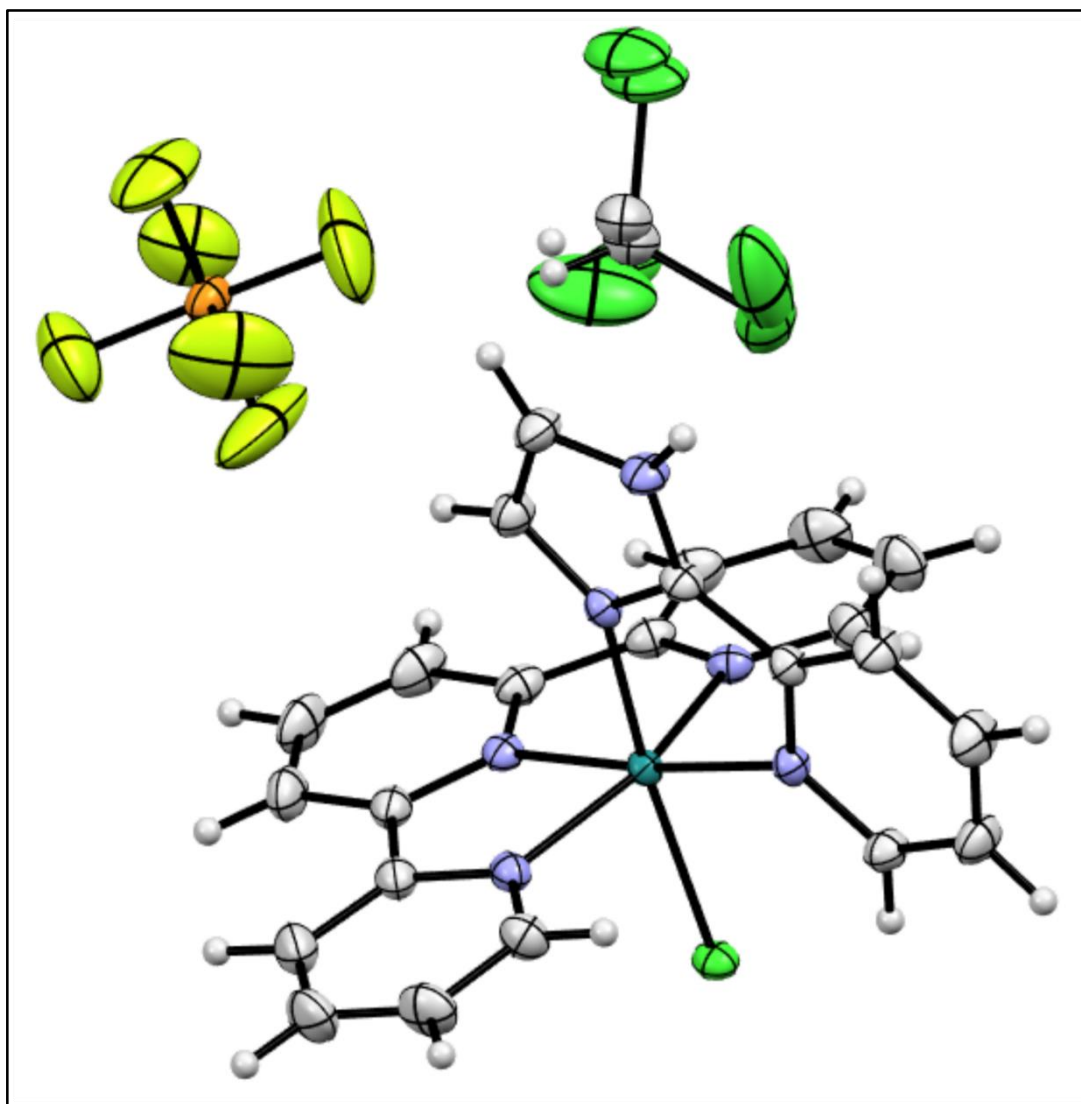


**Figure 11.** ORTEP view of the X-ray structure of *trans*-[Ru<sup>II</sup>(Himpy)(tpy)(Cl)](PF<sub>6</sub>)·CHCl<sub>3</sub> at 150K. Atoms are colored as follows: Carbon (gray), nitrogen (blue), hydrogen (soft gray), ruthenium (teal), phosphorous (orange), chlorine (green), fluorine (yellow).

**Table 6.** Crystallographic data for the complex *trans*-[Ru<sup>II</sup>(Himpy)(tpy)(Cl)](PF<sub>6</sub>)·CHCl<sub>3</sub>.

Parameter	Complex
<b>Empirical formula</b>	C <sub>25</sub> H <sub>20</sub> N <sub>6</sub> Cl <sub>7</sub> PF <sub>6</sub> Ru
<b>Fw</b>	898.66
<b>Crystal symmetry</b>	Orthorhombic
<b>Space group</b>	P n m a
<b>a (Å)</b>	24.6447(19)
<b>b (Å)</b>	15.2207(12)
<b>c (Å)</b>	8.9651(7)
<b>α (°)</b>	90
<b>β (°)</b>	90
<b>γ (°)</b>	90
<b>V (Å<sup>3</sup>)</b>	3362.9(5)
<b>Z</b>	4
<b>T (K)</b>	150

#### 4.4. UV-visible spectroscopy

The electronic properties of all the ruthenium(II) chlorido complexes were studied by UV-vis spectroscopy and their absorption spectra in ethanolic solution are shown in **Figure 12**. All complexes show narrow, strong absorption bands in the UV region assigned to  $\pi \rightarrow \pi^*$  ligand transitions. The visible region is characterized by broad, weak absorption bands attributed to MLCT transitions from the  $d\pi(\text{Ru})$  orbital to the  $\pi^*$  orbital of either terpyridine or Himpx ligands.<sup>53</sup> The transitions assignments of the absorption bands in the visible region were performed on the basis of previous TD-DFT calculated electronic spectra for [Ru<sup>II</sup>(H<sub>2</sub>bim)(tpy)(OH<sub>2</sub>)]<sup>2+</sup> and [Ru<sup>II</sup>(bpy)(tpy)(OH<sub>2</sub>)]<sup>2+</sup> complexes. In both complexes, the LUMO and LUMO + 1 orbitals were mostly located on the tpy group, whereas the next antibonding orbital was spread over the H<sub>2</sub>bim and bpy ligands, respectively.<sup>53,54</sup> In all the ruthenium complexes of this Thesis, the lowest energetic-visible region (450–600 nm) was characterized by transitions from  $d\pi(\text{Ru})$  orbital to  $\pi^*(\text{tpy})$  orbitals. On the other hand, the highest energetic-visible region showed absorption bands at 350–450 nm region, which were assigned to transitions from  $d\pi(\text{Ru})$  to  $\pi^*(\text{Himpx})$  orbitals.

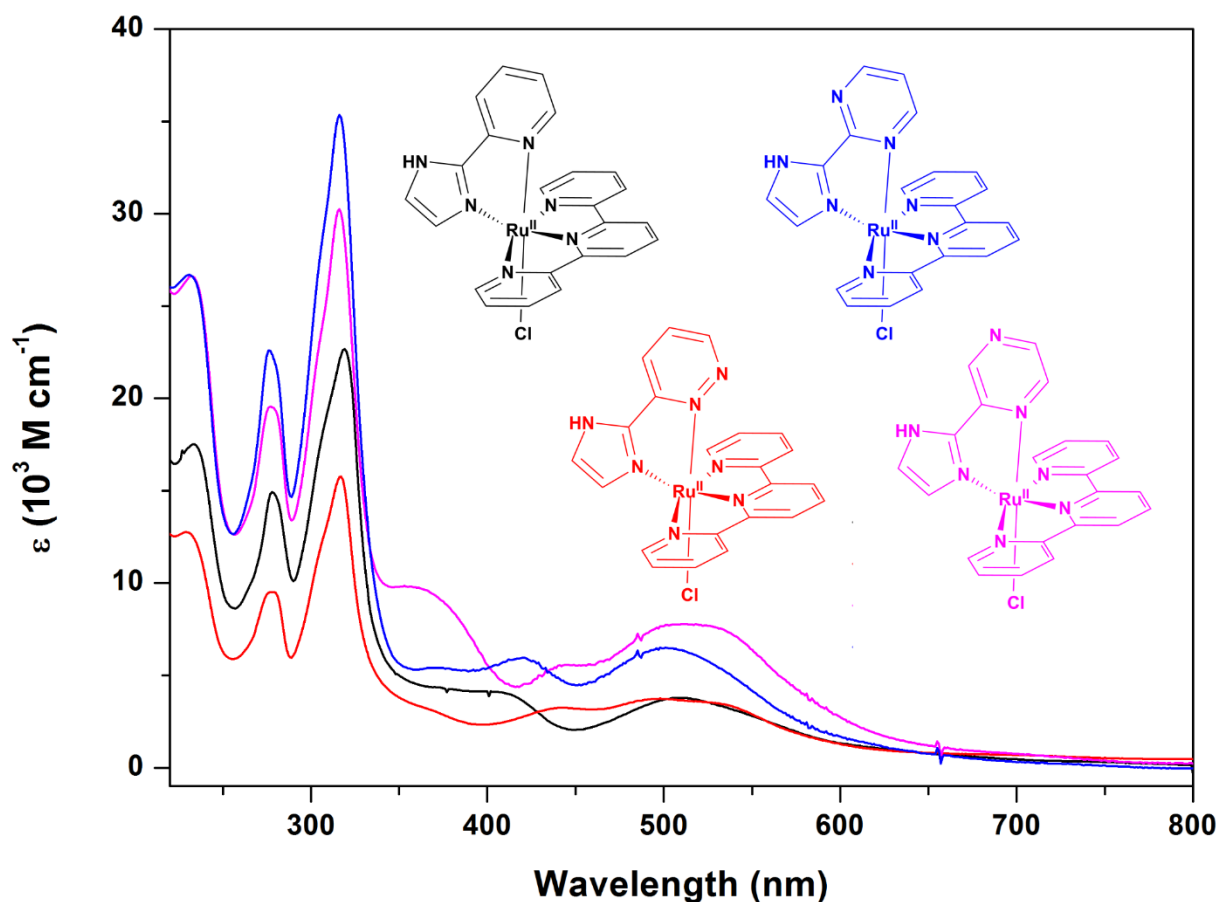


**Figure 12.** UV-visible spectra of ruthenium(II) chlorido complexes in ethanol.

The most energetic absorption bands among them belong to the complexes containing the Himpy and Himpm ligands, with transitions at 408 and 420 nm, respectively. The other two complexes containing the Himpa and Himpz ligands display the lowest energetic absorption bands at 442 and 447 nm, respectively. These transitions assignments were supported by cyclic voltammetry measurements in the ligands which displayed a better acceptor behavior (lower reduction potentials) of the Himpa and Himpz compared with Himpy and Himpm (**Figure 13**).

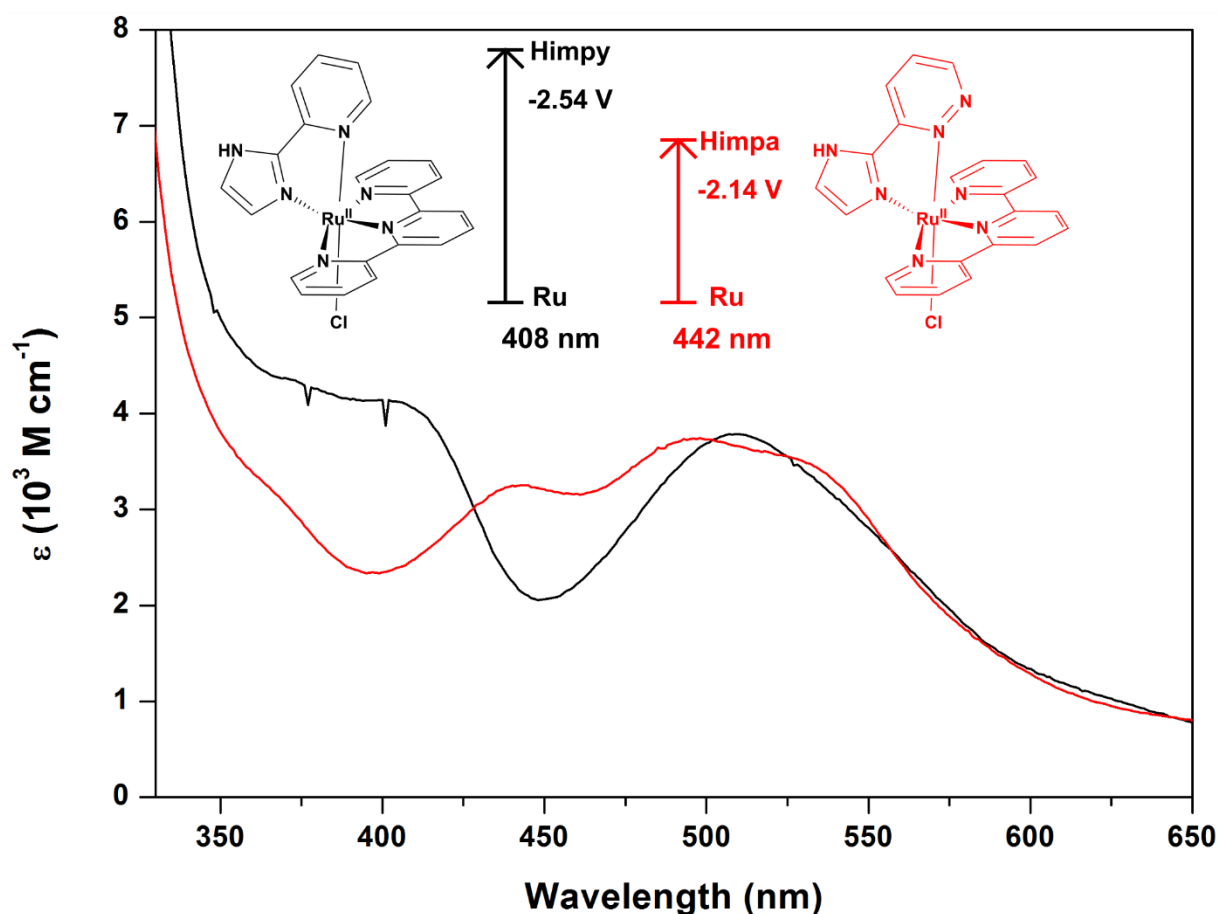


**Figure 13.** MLCT region of the UV-visible spectra for  $[\text{Ru}^{\text{II}}(\text{Himpy})(\text{tpy})(\text{Cl})]^+$  and  $[\text{Ru}^{\text{II}}(\text{Himpa})(\text{tpy})(\text{Cl})]^+$  complexes in ethanol. The inset figure shows the energy transitions and the correlation with the ligands' reduction potentials.

The electronic properties of the *cis* and *trans* isomers of the ruthenium chlorido complexes were studied by using the UV-visible spectroscopy. **Figure 14** shows similar absorption bands for both *cis*- and *trans*- $[\text{Ru}^{\text{II}}(\text{Himpy})(\text{tpy})(\text{Cl})]^+$  complexes but with different molar absorption coefficients. There is also a slightly noticeable but at the same time important difference between them in the 350–400 nm region. The absorption band at 379 nm corresponding to the *trans* isomer belongs to the transition involving the ruthenium and imidazole orbitals, as in the case for the complex  $[\text{Ru}^{\text{II}}(\text{H}_2\text{bim})(\text{tpy})(\text{Cl})]^+$  ( $\text{Ru} \rightarrow$  imidazole transition at 364 nm in water).<sup>53</sup>

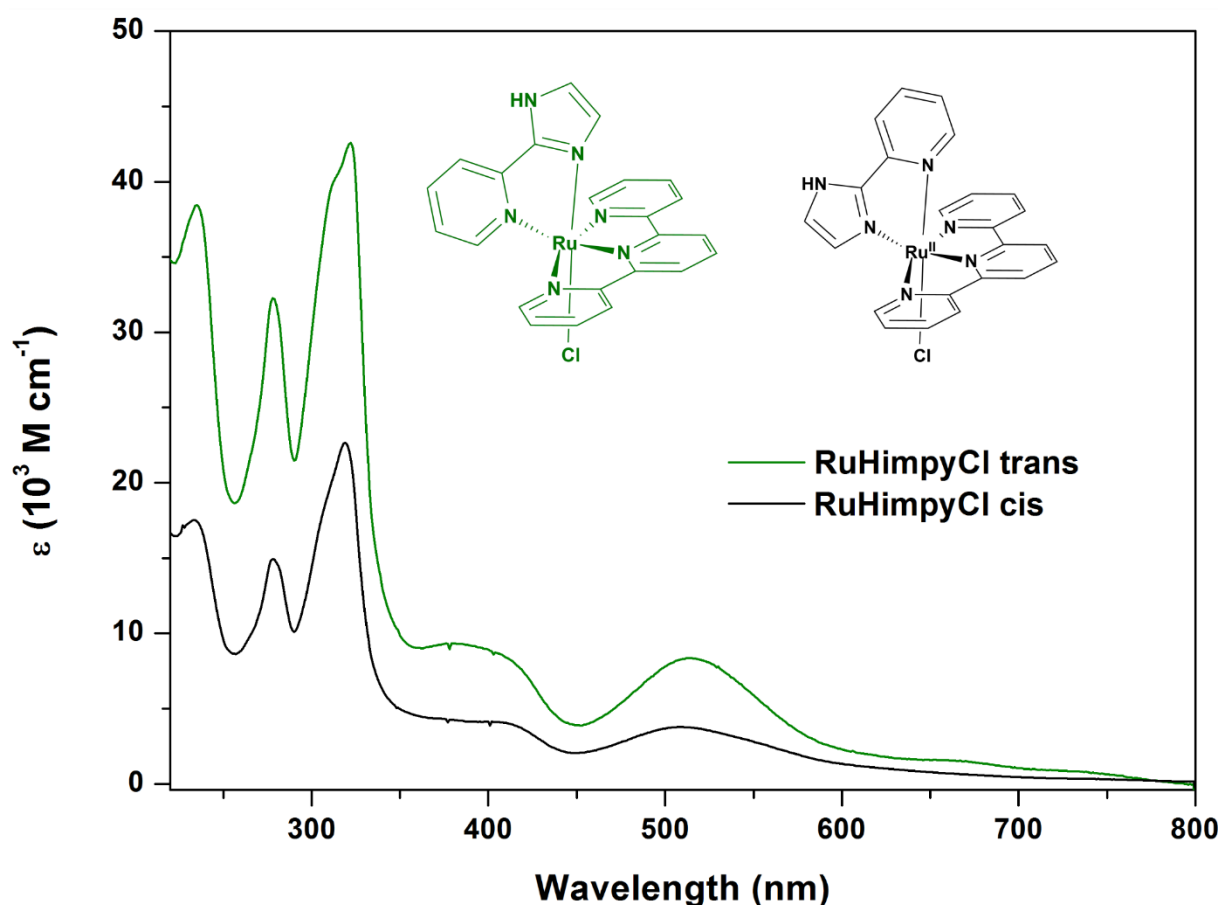


**Figure 14.** UV-visible spectra of cis- and trans-[Ru<sup>II</sup>(Himpy)(tpy)(Cl)]<sup>+</sup> complexes in ethanol.

#### 4.5 pK<sub>a</sub> of Ru(II) chlorido complexes

To get insight into the acid–base properties of the complexes, their pK<sub>a</sub> values were obtained using spectrophotometric titration in a broad pH range. **Figure 15** illustrates the spectrophotometric curves at different pH for the *cis*-[Ru<sup>II</sup>(Himpy)(tpy)(Cl)]<sup>+</sup> complex featuring two isosbestic points at 414 and 498 nm which indicate an equilibrium between protonated and deprotonated species, consistent with the monoprotic acid behavior expected for the deprotonation of N–H proton of the Himpy ligand. The plot of absorbances versus pH gave a pK<sub>a</sub> value of 8.96, which is higher than the pK<sub>a</sub> of 13.4 for the free ligand,<sup>55</sup> as expected after coordination due to electronic density donation from imidazole nitrogen to the metal center making the pyrrole-like hydrogen more acidic. It is also observed that deprotonation causes a red shift of the MLCT absorption bands from 465 to 485 nm, which should be ascribed to an enhanced  $\pi$ -donor ability of the imidazole after

deprotonation of the N–H proton that raises the energy of the  $d\pi(\text{Ru})$  orbital and consequently decreases the energy for MLCT transition.<sup>56,57</sup>

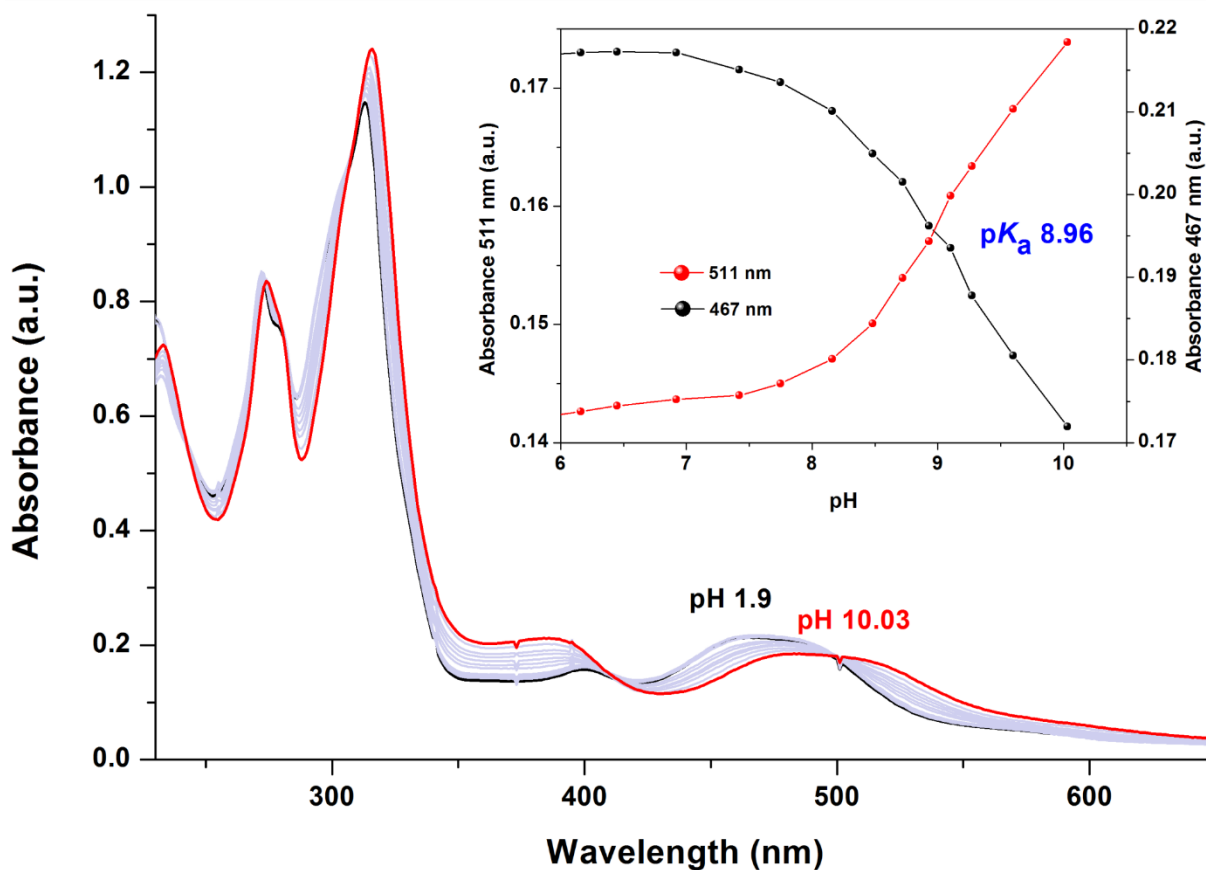


**Figure 15.** Absorption bands changes of  $\text{cis-}[\text{Ru}^{\text{II}}(\text{Himpy})(\text{tpy})(\text{Cl})]^+$  ( $50 \mu\text{M}$ ) in  $0.04 \text{ M}$  Britton–Robinson buffer after titrating with  $4 \text{ M}$   $\text{NaOH}$  solution in pH range from 1.9 to 10.03. Inset: Plot of absorbances at 467 and 511 nm versus pH.

# CHAPTER 3

## WATER OXIDATION BY RUTHENIUM AQUA COMPLEXES

### 1. INTRODUCTION

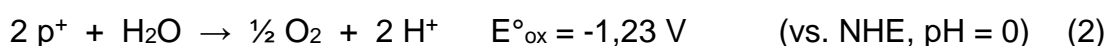
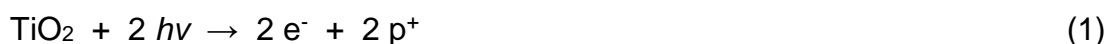
#### 1.1 General concepts

In the last decades, so much have been talked about the problems related to the use of products derived from carbon fossils such as petroleum, gasoline, kerosene, and other fossil fuels. The high worldwide level of consumption for energetic demands has led to serious environmental issues induced by high levels of CO<sub>2</sub> production. Another problem is regarding the growth of consumption of those energy sources for the next decades which will increase in such a way that those sources will not be enough to supply the entire world population. Given this scenario, various alternative sources of energy that are economical, clean, cheap, and renewable are necessary.

#### 1.2 Water oxidation

Water splitting (breaking of a water molecule into hydrogen H<sub>2</sub> and oxygen O<sub>2</sub>) is an outstanding choice of energy source using solar energy that meets those requirements because a green fuel can be generated in the reduction process (hydrogen, H<sub>2</sub>), contrary to fossil fuels, the major source of energy so far that release CO<sub>2</sub> and other environment-polluting side products. The oxidation process, called water oxidation reaction, is the bottleneck of the whole process because it implies the loss of protons and electrons ( $2\text{H}_2\text{O} \rightleftharpoons \text{O}_2 + 4\text{H}^+ + 4\text{e}^-$ ),<sup>58</sup> which means that an efficient catalyst is required like in photosynthesis process,<sup>59</sup> where the oxygen-evolving complex (OEC) mediates the water oxidation dealing with several electrons transfer as well as protons transfer processes,<sup>60</sup> to reduce the activation energy for improving the rate and efficiency of the reaction.

The possibility of obtaining oxygen and hydrogen from water using sunlight was demonstrated by Fujishima and Honda in 1972.<sup>61</sup> They used the TiO<sub>2</sub> semiconductor as an electrode (photoanode) for the oxidation of water and Pt as the auxiliary electrode for the reduction of protons generated in water oxidation. They suggested that water could be decomposed by light into oxygen and hydrogen, according to the following reactions:

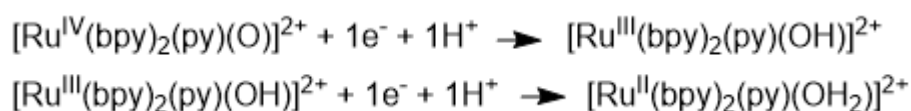


The overall reaction is given by:



### 1.3 Ruthenium polypyridyl complexes

Since then, several studies were carried out concerning the use of molecules being capable to catalyze the water oxidation. Among various catalysts used, ruthenium polypyridyl aqua complexes have been widely studied to achieve that purpose, since those complexes meet the demands to carry out the water oxidation reaction such as proton-coupled electron transfer process reaching high oxidation states which can be stabilized by strong electronic  $\sigma$ - and  $\pi$ -donating character of polypyridyl ligands allowing to achieve the higher oxidation state species at moderated half-wave potentials<sup>58,62</sup> featuring redox reversible behavior.<sup>63–65</sup>



**Scheme 1.** Proton-coupled electron transfer reactions of a ruthenium(II) polypyridyl complex. Adapted from Meyer *et al.*<sup>58</sup>

One of the first examples regarding ruthenium complexes using light energy to modify their oxidant properties was reported by Young *et al.*<sup>66</sup> They performed a

reaction between a previous light-excited  $\text{Ru}(\text{bpy})_3^{2+}$  molecule and a methylviologen dication resulting in an electron transfer which gives two products capable of performing water splitting based on their redox potentials.<sup>67</sup>

The first successful attempt to oxidize water with a well-defined ruthenium aqua complex was carried out by Meyer *et al.*<sup>68</sup> who showed the chemical oxidation of water after using 4 equivalents of Ce(IV) with the oxo-bridged ruthenium dimer  $\text{cis},\text{cis}-[(\text{bpy})_2(\text{H}_2\text{O})\text{RuORu}(\text{OH}_2)(\text{bpy})_2]^{4+}$  as the catalyst, giving rise to four proton-four electron transfer processes which led the catalyst to a high oxidation state which then could rapidly oxidize the water molecule. After that seminal work, many other studies involving dinuclear ruthenium complexes for water oxidation were performed, where different factors such as steric effects of ligands,<sup>69</sup> introduction of rigid bridge ligands,<sup>70</sup> negatively charged ligands<sup>71</sup> were assessed to understand the mechanistic pathway of water oxidation and performance on the catalysis.

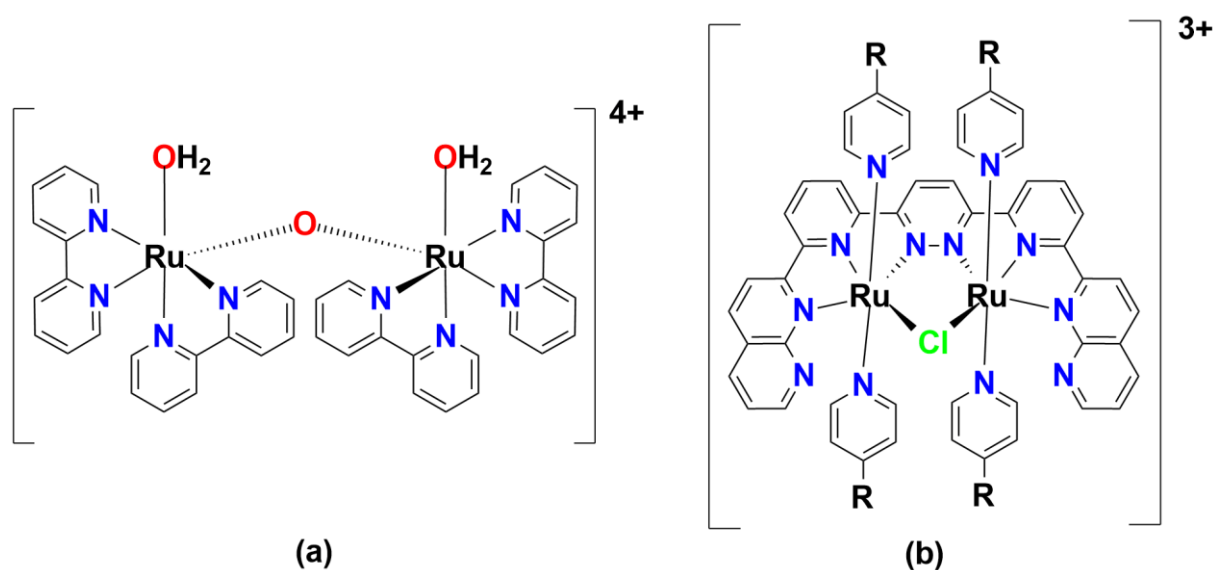


**Figure 16.** Dinuclear (a) “Blue dimer”  $\text{cis},\text{cis}-[(\text{bpy})_2(\text{OH}_2)\text{RuORu}(\text{OH}_2)(\text{bpy})_2]^{4+}$  complex and (b) Ruthenium complex containing the 3,6-bis-[6'-(1'',8''-naphthyrid-2''-yl)-pyrid-2'-yl]pyridazine ligand. Adapted from Meyer *et al.*<sup>68</sup> and Thummel *et al.*,<sup>69</sup> respectively.

After many years focusing on dinuclear compounds because of the belief that two metal centers were necessary to oxidize water, and the lack of work related to mononuclear ruthenium complexes, many authors claimed if using a single-site compound could be effective in the catalysis of water oxidation. In 2008, Meyer *et al.*<sup>72</sup> reported the synthesis of  $[\text{Ru}^{\text{II}}(\text{bpz})(\text{tpy})(\text{OH}_2)]^{2+}$  and  $[\text{Ru}^{\text{II}}(\text{bpm})(\text{tpy})(\text{OH}_2)]^{2+}$

complexes and proved that these single-site complexes were able to perform the water oxidation catalysis, discarding the assumption that at least two metal center should be present in the complexes. They also proposed a mechanism based on their results to show how changes in the structure of the ligand can make a difference in the catalytic activity. To show the importance of the presence of a water molecule in the structure of the ruthenium catalyst, Sakai and Masaoka<sup>44</sup> investigated the performance of chlorido and aqua complexes toward oxidation of water, concluding that the water molecule in the complex plays a crucial role to effective catalysis.

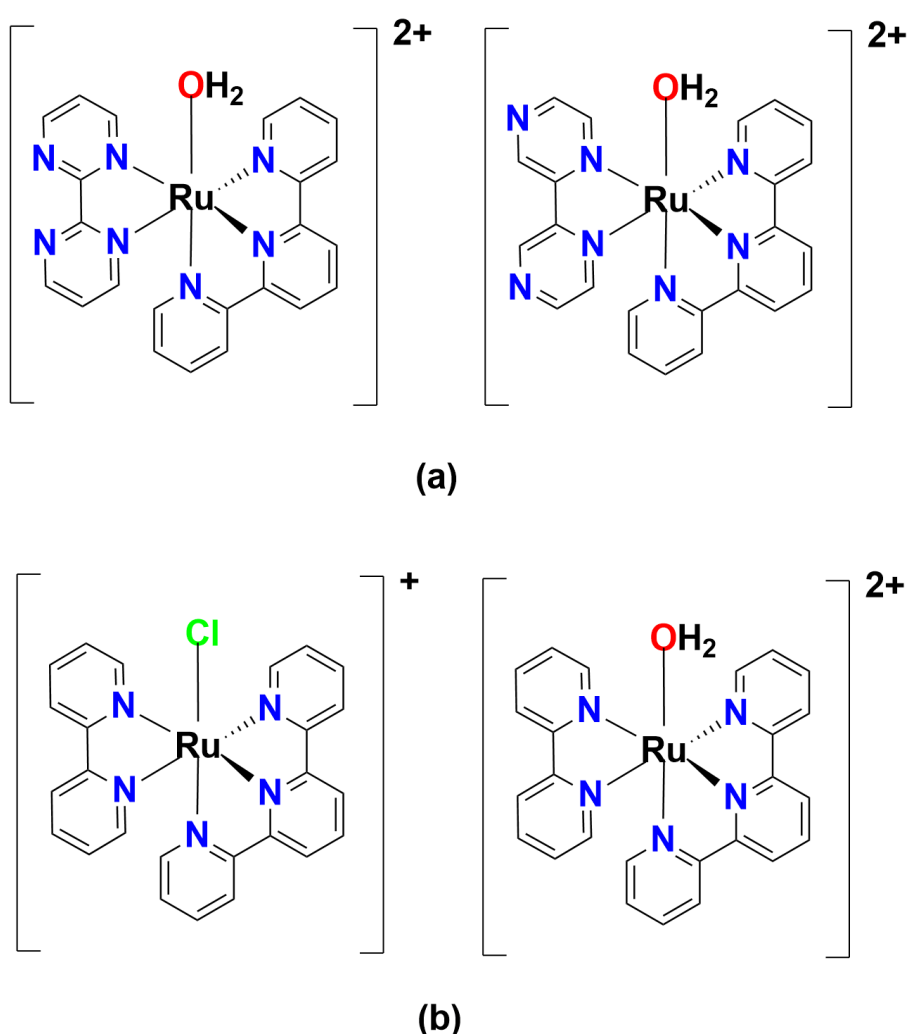


**Figure 17.** Mononuclear (a)  $[\text{Ru}^{\text{II}}(\text{bpm})(\text{tpy})(\text{OH}_2)]^{2+}$  and  $[\text{Ru}^{\text{II}}(\text{bpz})(\text{tpy})(\text{OH}_2)]^{2+}$  and (b)  $[\text{Ru}^{\text{II}}(\text{bpy})(\text{tpy})(\text{Cl})]^+$  and  $[\text{Ru}^{\text{II}}(\text{bpy})(\text{tpy})(\text{OH}_2)]^{2+}$  complexes. Adapted from Meyer *et al.*<sup>72</sup> and Sakai *et al.*,<sup>44</sup> respectively.

This Thesis is based on substituting one pyridine molecule by an imidazole in the  $[\text{Ru}^{\text{II}}(\text{bpy})(\text{tpy})(\text{OH}_2)]^{2+}$  complex and changing the other pyridine moiety by a

diazine ring to evaluate the catalytic performance of the water oxidation by changing the electron donor–acceptor properties of the ligand. The ligands to be used in this Thesis are the terpyridine ring, whose ruthenium complexes are widely known to exhibit remarkable electronic and redox properties,<sup>73–76</sup> and the heteroaryl-2-imidazole ligands combining excellent  $\pi$ -acceptors six-membered nitrogen heteroaryl rings as well as five-membered imidazole with better  $\pi$ - and  $\sigma$ -donating properties, which in turn can modify the physical and electronic properties of their ruthenium complexes.<sup>77–80</sup> We are also interested in understanding how changes in the position of the nitrogen atom in the heteroaryl rings could influence the electronic and redox properties of the ruthenium aqua complexes and consequently in their catalytic performance. The choice of the imidazole moiety to substitute the pyridine ring was also made considering the ionizable acidic NH proton and the higher basicity of the imidazole which can increase the catalytic performance.<sup>53,81</sup>

In this chapter, four ruthenium(II) complexes,  $[\text{Ru}^{\text{II}}(\text{Himpy})(\text{tpy})(\text{OH}_2)](\text{PF}_6)_2$  (**1**),  $[\text{Ru}^{\text{II}}(\text{Himpa})(\text{tpy})(\text{OH}_2)](\text{PF}_6)_2$  (**2**),  $[\text{Ru}^{\text{II}}(\text{Himpm})(\text{tpy})(\text{OH}_2)](\text{PF}_6)_2$  (**3**), and  $[\text{Ru}^{\text{II}}(\text{Himpz})(\text{tpy})(\text{OH}_2)](\text{PF}_6)_2$  (**4**), were synthesized according to the literature,<sup>52</sup> to evaluate the influence of the heteroaryl-2-imidazole ligands on their catalytic performance. The complexes were characterized by conductivity measurements, <sup>1</sup>H-NMR spectroscopy, UV-vis spectroscopy, mass spectrometry, and X-ray crystallography. Cyclic, differential pulse, and square wave voltammetry measurements were carried out for all the complexes to evaluate the influence of donor–acceptor properties of the Himp<sub>x</sub> ligands in the electronic properties of those complexes. Pourbaix diagrams obtained through electrochemical measurements were accomplished for complexes to assess the influence of Himp<sub>x</sub> ligands on mechanism pathway for water oxidation reaction. **Chart 2** displays the four expected Ru(II) aqua complexes to be studied in this Thesis.

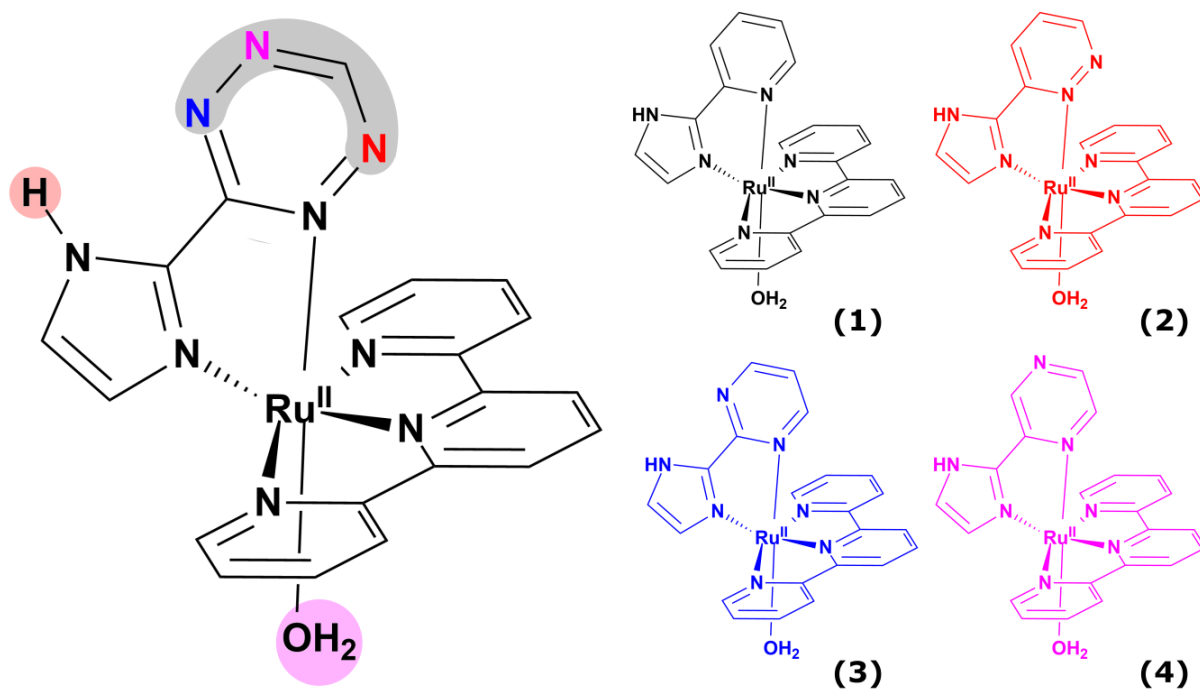


**Chart 2.** Ruthenium(II) aqua complexes containing the heteroaryl-2-imidazole ligands.  $[\text{Ru}^{\text{II}}(\text{Himpy})(\text{tpy})(\text{OH}_2)](\text{PF}_6)_2$  (1),  $[\text{Ru}^{\text{II}}(\text{Himpa})(\text{tpy})(\text{OH}_2)](\text{PF}_6)_2$  (2),  $[\text{Ru}^{\text{II}}(\text{Himpm})(\text{tpy})(\text{OH}_2)](\text{PF}_6)_2$  (3), and  $[\text{Ru}^{\text{II}}(\text{Himpz})(\text{tpy})(\text{OH}_2)](\text{PF}_6)_2$  (4).

## 2. OBJECTIVES

Evaluate the role of ionizable N–H imidazole proton on electronic properties of ruthenium complexes and their influence on catalytic performance of water oxidation.

Evaluate the modifications on position of nitrogen atom on heteroaryl moiety in the complexes on the pathways of reaction toward the catalysis of water oxidation.

## 3. EXPERIMENTAL SECTION

### 3.1 General

Ammonium hexafluorophosphate ( $\text{NH}_4\text{PF}_6$ , 99.98%, Sigma Aldrich), ascorbic acid (99%, Sigma Aldrich), buffer solutions of 4.0, 7.0 and 10.0 (Labsynth), lithium chloride (98%, Synth), potassium chloride (99%, Labsynth), potassium hydrogen phthalate ( $\text{C}_8\text{H}_5\text{O}_4\text{K}$ , 99.5%, Labsynth), ruthenium(III) chloride trihydrate

( $\text{RuCl}_3 \cdot 3\text{H}_2\text{O}$ , technical grade, Sigma-Aldrich), silica gel (pore size  $60\text{\AA}$ , 220–440 mesh particle size, 35–75  $\mu\text{m}$  particle size, for flash chromatography, Sigma-Aldrich), silver nitrate ( $\text{AgNO}_3$ ,  $\geq 99.0\%$ , Sigma-Aldrich), sodium hydroxide (97%, Dinâmica Química Contemporânea Ltda.), 2,2':6',2''-terpyridine (tpy, 98%, Sigma Aldrich) were received and used without further purification. Acetone, acetonitrile, chloroform, diethyl ether, hydrochloric acid and methanol were purchased from Labsynth. TLC plates (ALUGRAM XTRA SIL G, Macherey-Nagel) were used to assess the best eluent for column chromatography. Absolute ethanol was purchased from Merck and stored in molecular sieves. N,N'-dimethylformamide (DMF, HPLC grade,  $\geq 99.9\%$ ) for synthesis was purchased from Sigma-Aldrich. Methanol (HPLC/Spectrophotometric grade,  $\geq 99.9\%$ ) for UV-vis spectroscopic and mass spectrometry measurements was purchased from Tedia Brazil. Molecular sieves ( $4\text{\AA}$ , beads, 4–8 mesh, Sigma-Aldrich) were used for drying organic solvents for further measurements. The Ru(II) aqua complexes were synthesized as described by Cheung *et al.*<sup>52</sup> with some modifications.

### 3.2 Measurements

**NMR spectroscopy.**  $^1\text{H}$  NMR spectra were obtained from 10 mg of samples in 0.75 mL deuterated DMSO- $d_6$  and  $\text{CD}_3\text{OD}$  solvents, using Bruker Avance 250, 400 or 500 MHz spectrometers. Chemical shifts were reported in parts per million (ppm) and referenced to solvent residual peak ( $\delta(\text{DMSO-}d_6) = 2.50$  ppm,  $\delta(\text{CD}_3\text{OD}) = 3.31$  ppm). Signal multiplicities were abbreviated as s (singlet), d (doublet), t (triplet), and m (multiplet). The data were processed by using TopSpin 3.6.1 software.

**UV-visible spectroscopy.** Electronic spectra in the 200–800 nm range were acquired on an Agilent 8453 UV-vis spectrophotometer using a quartz cell with a path length of 10 mm.

**Electrochemical measurements.** Cyclic voltammetry measurements were performed on a Metrohm Autolab PGSTAT12 potentiostat, using a three-electrode system consisting of a glassy carbon working electrode (3 mm disk diameter), saturated calomel electrode (SCE) as a reference electrode and Pt wire auxiliary electrode.

The Pourbaix diagrams of the aqua compounds were obtained in 0.04 M Britton–Robinson buffer + 0.1 M  $\text{KNO}_3$  solution by titrating the compounds solutions

against 2 M KOH and recording the cyclic voltammograms (CV), differential pulse voltammogram (DPV), and square wave voltammogram (SWV) at each specific pH value.

**Determination of  $pK_a$  values.** Spectrophotometric titrations were carried out to determine the  $pK_a$  values of the compounds in 0.04 M Britton–Robinson buffer solution. The pH was recorded by using a Metrohm 827 pH meter. The solutions were titrated against 4 M aqueous NaOH solution.

**X-ray crystallography.** Crystal data were collected on a Bruker Kappa APEX II DUO diffractometer using a Mo  $K\alpha$  ( $\lambda = 0.71073 \text{ \AA}$ ) X-ray source at 150 K.

**Theoretical calculations.** Density Functional Theory (DFT) calculations were performed with the PBE0 hybrid functional and the def2-TZVP basis set for all atoms using ORCA software version 4.2.0.

**Mass spectrometry.** Electrospray ionization mass spectrometry (ESI-MS) measurements were carried out on a Waters Synapt Q-TOF mass spectrometer. The data were processed by using MassLynx V4.1 software.

**Elemental analysis.** Composition of C, H, and N of samples was acquired on an EA-1108 CHNS-O Element Analyzer.

**Conductivity measurements.** Data were obtained using a Mca-150 conductimeter.

### 3.3 Synthesis of *cis*-[Ru<sup>II</sup>(Himpy)(tpy)(OH<sub>2</sub>)](PF<sub>6</sub>)<sub>2</sub>

To a 50 mL round-bottom amber flask containing *cis*-[Ru<sup>II</sup>(Himpy)(tpy)(Cl)]PF<sub>6</sub> (66 mg, 0.1 mmol) dissolved in ethanol 30 mL under stirring and heated at 70 °C was added an aqueous solution (2 mL) of AgNO<sub>3</sub> (25 mg, 0.15 mmol). The reaction mixture was kept at 70 °C under stirring for 3 h (the reaction time for each complex was optimized by following the increasing of the chloride/aqua absorption bands ratio until no changes were observed – see Appendix, Figure S 4). After the completion of the reaction, the solution obtained was filtered to remove all the AgCl produced by using a syringe filter (Chromafil-Xtra PTFE 45/25) and the volume of the ethanol was removed and substituted with water while heating the solution at 70 °C. After removing the ethanol from the solution, ascorbic acid was added to precipitate the excess of Ag<sup>+</sup> while heating at 70 °C for 10 minutes. Finally, the solution was filtered

again and then an aqueous solution of  $\text{NH}_4\text{PF}_6$  (300 mg, 10 mL) was added to the final solution ( $V_{\text{solution}} = 30$  mL). After cooled overnight, the solution was filtered and washed with cold water to remove the remaining  $\text{NH}_4\text{PF}_6$ . Finally, the solid was placed in a desiccator under reduced pressure for drying. Mass yield: 60 mg (76%). **Elemental analysis** for  $\text{C}_{23}\text{H}_{20}\text{N}_6\text{OP}_2\text{F}_{12}\text{Ru}\cdot\text{H}_2\text{O}$ , Calculated (%): C, 34.28; H, 2.73; N, 10.43. Found (%): C, 33.95; H, 3.30; N, 11.14.  **$^1\text{H-NMR}$  (400 MHz,  $\text{DMSO-d}_6$ )**:  $\delta$ /ppm 14.47 (s, 1H), 8.84 (d, 2H,  $J = 8$  Hz), 8.71 (d, 2H,  $J = 8$  Hz), 8.26 (t, 1H,  $J = 8$  Hz), 8.22 (d, 1H,  $J = 1.3$  Hz), 8.12 (d, 1H,  $J = 1.4$  Hz), 8.10 (d, 1H,  $J = 6$  Hz), 8.06 (td, 2H,  $J = 7.8, 1.4$  Hz), 7.80 (dd, 2H,  $J = 5.4, 0.7$  Hz), 7.73 (td, 1H,  $J = 7.8, 1.3$  Hz), 7.51 (ddd, 2H,  $J = 7.8, 5.6, 1.2$  Hz), 7.09 (d, 1H,  $J = 5.6$  Hz), 6.92 (ddd, 1H,  $J = 7.8, 5.9, 1.3$  Hz), 5.54 (s, 2H). **ESI-MS (MeOH)**  $m/z$ : 249.0  $[\text{Ru}^{\text{II}}(\text{Himpy})(\text{tpy})(\text{OH}_2)]^{2+}$ , 511.0  $[\text{Ru}(\text{impy})(\text{tpy})(\text{MeOH})]^+$ . **UV-Vis** [ $\lambda_{\text{max}}$ , nm ( $\epsilon$ ,  $\text{M}^{-1} \text{cm}^{-1}$ ) in  $\text{H}_2\text{O}$ ]: 222 (sh, 24,9), 271 (24,0), 278 (sh, 21,8), 312 (32,3), 398 (4,4), 463 (5,6).

### 3.4 Synthesis of *cis*- $[\text{Ru}^{\text{II}}(\text{Himpa})(\text{tpy})(\text{OH}_2)](\text{PF}_6)_2$

To a 25 mL round-bottom amber flask containing *cis*- $[\text{Ru}^{\text{II}}(\text{Himpa})(\text{tpy})(\text{Cl})]\text{PF}_6$  (66 mg, 0.1 mmol) dissolved in acetone/water 1:3 (12 mL) under stirring was added an aqueous solution (1 mL) of  $\text{AgNO}_3$  (20 mg, 0.12 mmol). The reaction mixture was heated at 100 °C under stirring for 1 h. After the completion of the reaction, the solution was filtered under reduced pressure to remove the  $\text{AgCl}$  produced and then an aqueous solution of  $\text{NH}_4\text{PF}_6$  (80 mg, 5 mL) was added. The volume of the solvent was reduced until 5 mL (a precipitate was appearing in that moment) and the final solution was left in the refrigerator overnight. The next day, the solution was filtered to give a black solid which was washed with cold water to remove the remaining  $\text{NH}_4\text{PF}_6$ . Finally, the solid was placed in a desiccator under reduced pressure for drying. Mass yield: 18 mg (23%).  **$^1\text{H-NMR}$  (500 MHz,  $\text{DMSO-d}_6$ )**:  $\delta$  14.64 (s, 1H), 8.77 (d, 2H,  $J = 8.1$  Hz), 8.68 (d, 2H,  $J = 8.0$  Hz), 8.49 (dd, 1H,  $J = 5.0, 1.7$  Hz), 8.32 (d, 1H,  $J = 1.2$  Hz), 8.25 (t, 1H,  $J = 8.1$  Hz), 8.22 (dd, 1H,  $J = 8.3, 1.7$  Hz), 8.16 (d, 1H,  $J = 1.0$  Hz), 8.07 (td, 2H,  $J = 7.9, 1.2$  Hz), 7.79 (d, 2H,  $J = 5.4$  Hz), 7.51 (m, 3H), 5.94 (s, 2H). **ESI-MS (MeOH)**  $m/z$ : 511.9  $[\text{Ru}^{\text{II}}(\text{impa})(\text{tpy})(\text{MeOH})]^+$ , 643.9  $[\text{Ru}^{\text{II}}(\text{Himpa})(\text{tpy})(\text{OH}_2)](\text{PF}_6)^+$ . **UV-Vis** [ $\lambda_{\text{max}}$ , nm ( $\epsilon$ ,  $\text{M}^{-1} \text{cm}^{-1}$ ) in  $\text{H}_2\text{O}$ ]: 230 (sh, 21,4), 272 (23,7), 279 (sh, 21,9), 310 (34,7), 415 (5,9), 470 (9,8).

### 3.5 Synthesis of *cis*-[Ru<sup>II</sup>(Himpz)(tpy)(OH<sub>2</sub>)](PF<sub>6</sub>)<sub>2</sub>

To a 25 mL round-bottom amber flask containing *cis*-[Ru<sup>II</sup>(Himpz)(tpy)(Cl)]Cl (50 mg, 0.09 mmol) dissolved in ethanol (25 mL) was added an aqueous solution (7 mL) of AgNO<sub>3</sub> (32 mg, 0.18 mmol). The reaction mixture was heated at 80 °C under stirring for 6 h. After the completion of the reaction, the solution was filtered under reduced pressure to remove the AgCl produced and then the solvents were removed on a rotary evaporator. The solid was dissolved in water (10 mL) and left under stirring at 100 °C for 30 minutes. After that, NH<sub>4</sub>PF<sub>6</sub> (1 g) was added to the solution, which then was cooled overnight. In the next day, the solution was filtered to give a reddish-brown solid which was washed with cold water to remove the remaining NH<sub>4</sub>PF<sub>6</sub>. Finally, the solid was placed on a desiccator under reduced pressure for drying. Mass yield: 42 mg (59 %). **<sup>1</sup>H-NMR (500 MHz, DMSO-d<sub>6</sub>):** δ 14.65 (s, 1H), 9.15 (s, 1H), 8.85 (d, 2H, J = 8.1 Hz), 8.73 (d, 2H, J = 8.1 Hz), 8.32 (t, 1H, J = 8.0 Hz), 8.30 (s, 1H), 8.12 (s, 1H), 8.10 (t, 2H, J = 8.0 Hz), 7.94 (d, 1H, J = 3.2 Hz), 7.73 (d, 2H, J = 4.9 Hz), 7.52 (t, 2H, J = 6.3 Hz), 7.40 (d, 1H, J = 2.4 Hz), 5.96 (s, 2H). **UV-Vis [(λ<sub>max</sub>, nm (ε, M<sup>-1</sup> cm<sup>-1</sup>) in H<sub>2</sub>O]:** 229 (sh, 17,7), 271 (17,2), 310 (25,3), 481 (7,6), 542 (sh, 3,6).

### 3.6 Synthesis of *cis*-[Ru<sup>II</sup>(Himpm)(tpy)(OH<sub>2</sub>)](PF<sub>6</sub>)<sub>2</sub>

The synthesis procedure was like that for the *cis*-[Ru<sup>II</sup>(Himpz)(tpy)(OH<sub>2</sub>)](PF<sub>6</sub>)<sub>2</sub> complex. To a 25 mL round-bottom amber flask containing *cis*-[Ru<sup>II</sup>(Himpm)(tpy)(Cl)]Cl (50 mg, 0.09 mmol) dissolved in ethanol (25 mL) was added an aqueous solution (7 mL) of AgNO<sub>3</sub> (32 mg, 0.18 mmol). The reaction mixture was heated at 80 °C under stirring for 6 h. Mass yield: 20 mg (28 %). **<sup>1</sup>H-NMR (500 MHz, DMSO-d<sub>6</sub>):** δ 14.93 (s, 1H), 8.84 (d, 2H, J = 8.1 Hz), 8.72 (d, 2H, J = 8.1 Hz), 8.61 (d, 1H, J = 3.2 Hz), 8.27 (t, 1H, J = 8.0 Hz), 8.25 (s, 1H), 8.18 (s, 1H), 8.08 (t, 2H, J = 7.3 Hz), 7.84 (d, 2H, J = 5.2 Hz), 7.53 (m, 3H), 6.97 (t, 1H, J = 5.0 Hz), 5.67 (s, 2H). **UV-Vis [(λ<sub>max</sub>, nm (ε, M<sup>-1</sup> cm<sup>-1</sup>) in H<sub>2</sub>O]:** 229 (sh, 26,5), 272 (30,2), 278 (sh, 28,2), 310 (40,7), 405 (6,0), 473 (8,4).

## 4. RESULTS AND DISCUSSION

### 4.1 Synthesis and characterization of the ruthenium complexes

The removal of chlorido ligands from the chlorido complexes was achieved by using silver nitrate to release AgCl, as confirmed by means of molar conductivities of chlorido complexes (146 and 109 S cm<sup>2</sup> mol<sup>-1</sup> for Himpy- and Himpa-complexes, respectively), indicating 1:1 composition, and the formed aqua complexes (300 and 320 S cm<sup>2</sup> mol<sup>-1</sup> for Himpy- and Himpa-complexes, respectively), displaying 2:1 composition,<sup>48</sup> as well as by mass spectrometry, UV-visible and <sup>1</sup>H-NMR spectroscopy, and X-ray crystallography.

### 4.2 <sup>1</sup>H-NMR spectroscopy

Replacement of chlorido by a water molecule to obtain the aqua complex was confirmed by <sup>1</sup>H-NMR spectroscopy (**Figure 18**). The most downfield signal in both spectra, in the region from 14.3 to 14.6 ppm, was assigned to pyrrole-like proton H24. All the proton signals were downfield shifted regarding the chlorido complex. An additional singlet signal appeared at 5.54 ppm which belongs to the protons of the aqua ligand. Different from complexes **1** and **2**, the chemical shift of the proton H22, which is *cis* to the axial chlorido ligand, did not altered significantly after substitution by the aqua ligand following the same pattern for a related ruthenium terpyridine complex bearing an imidazole ligand.<sup>53</sup> Chemical shifts, coupling constants, multiplicities and integrations are summarized in **Table 7**.

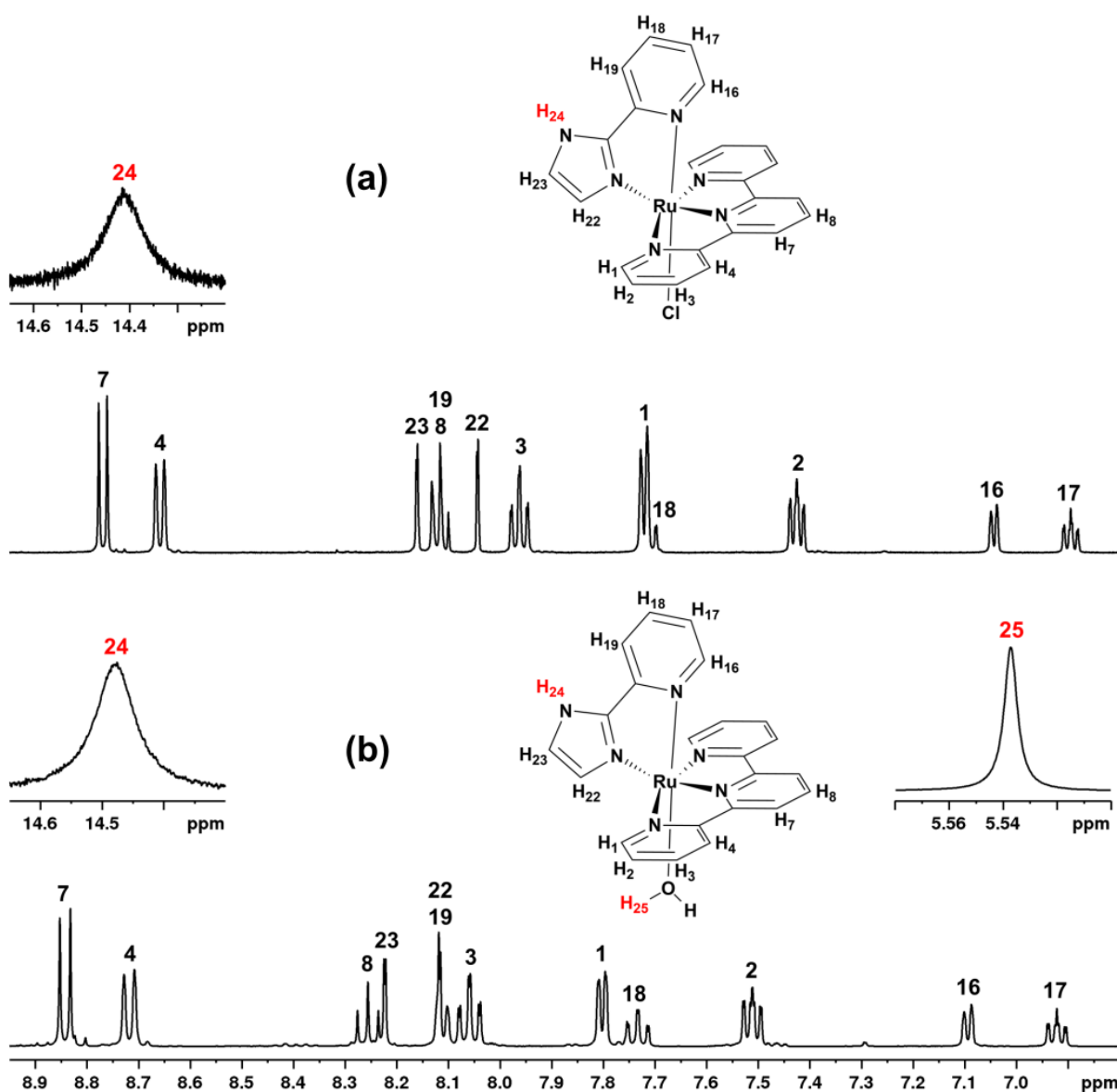


**Figure 18.**  $^1\text{H-NMR}$  spectra of (a)  $[\text{Ru}^{\text{II}}(\text{Himpy})(\text{tpy})(\text{Cl})]^+$  and (b)  $[\text{Ru}^{\text{II}}(\text{Himpy})(\text{tpy})(\text{OH}_2)]^{2+}$  complexes recorded in  $\text{DMSO-d}_6$  at 400 MHz.

**Table 7.**  $^1\text{H-NMR}$  data for  $[\text{Ru}^{\text{II}}(\text{Himpy})(\text{tpy})(\text{Cl})]^+$  and  $[\text{Ru}^{\text{II}}(\text{Himpy})(\text{tpy})(\text{OH}_2)]^{2+}$  complexes recorded in  $\text{DMSO-d}_6$ .

Compound	Hydrogen	Splitting pattern	Integration	Chemical shift (ppm)	Coupling constant (Hz)
	24	s	1	14.41	-
	7	d	2	8.77	7.8
	4	d	2	8.66	8.0
	23	d	1	8.16	1.2
	19	d	1	8.12	8.0
	8	t	1	8.11	8.0

<b>Chlorido complex</b>	22	d	1	8.04	1.2
	3	td	2	7.96	7.8, 1.4
	1	d	2	7.72	4.8
	18	td	1	7.71	7.8, 1.2
	2	ddd	2	7.43	7.7, 5.6, 1.2
	16	d	1	7.04	5.6
	17	ddd	1	6.89	7.9, 5.8, 1.2
<b>Aqua complex</b>	24	s	1	14.47	-
	7	d	2	8.84	8.0
	4	d	2	8.71	8.0
	8	t	1	8.26	8.0
	23	d	1	8.22	1.3
	22	d	1	8.12	1.4
	19	d	1	8.10	6.0
	3	td	2	8.06	7.8, 1.4
	1	dd	2	7.80	5.4, 0.7
	18	td	1	7.73	7.8, 1.3
	2	ddd	2	7.51	7.8, 5.6, 1.2
	16	d	1	7.09	5.6
	17	ddd	1	6.92	7.8, 5.9, 1.3
	25	s	2	5.54	-

Despite the apparent coordination of aqua ligand in the complex, there was not discarded the coordination of the DMSO solvent as a possibility. To confirm the presence of the aqua ligand, the  $^1\text{H-NMR}$  spectra of fresh chlorido and aqua complexes solutions were acquired. The solution containing the aqua complex was left standing for a week and its  $^1\text{H-NMR}$  spectrum was acquired again. **Figure 19** shows the signals shifts according to the axial ligand. All of them are clearly different, with the signals moving to more deshielded regions as the labilization of the axial ligand occurs. The most notorious difference among them is the peak signal at 5.9 ppm integrating for 2 hydrogens, which belongs to the aqua ligand and does not appear in the spectrum acquired after one week (Ru–DMSO), discarding the possibility of the DMSO solvent to be involved in the signals shifting of the aqua complex spectrum (red spectrum).

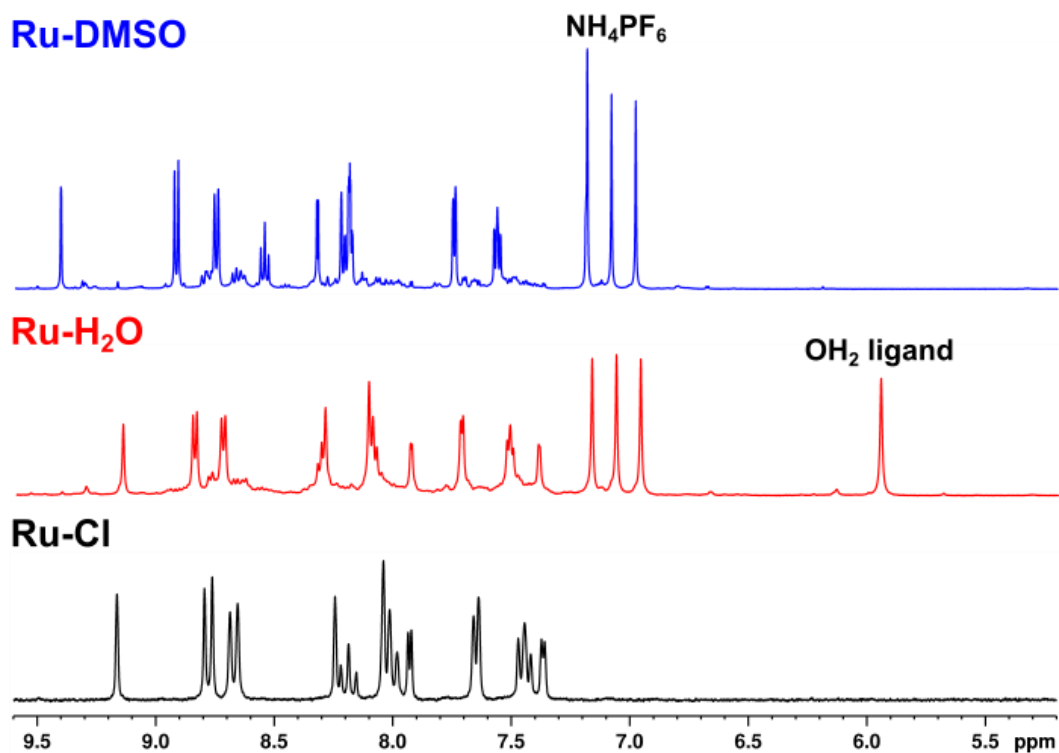


**Figure 19.**  $^1\text{H-NMR}$  spectra of fresh  $\text{cis-}[\text{Ru}^{\text{II}}(\text{Himpz})(\text{tpy})(\text{Cl})]^+$  (black) and  $\text{cis-}[\text{Ru}^{\text{II}}(\text{Himpz})(\text{tpy})(\text{OH}_2)]^{2+}$  (red) solutions, and the same aqua complex solution after standing one week (blue), all of them recorded in  $\text{DMSO-d}_6$  at 500 MHz.

The previous statement was also confirmed by acquiring the  $^1\text{H-NMR}$  spectra of fresh and one-week old solutions of a ruthenium chlorido complex (**Figure 20**), displaying the signals standing in the same chemical shifts.

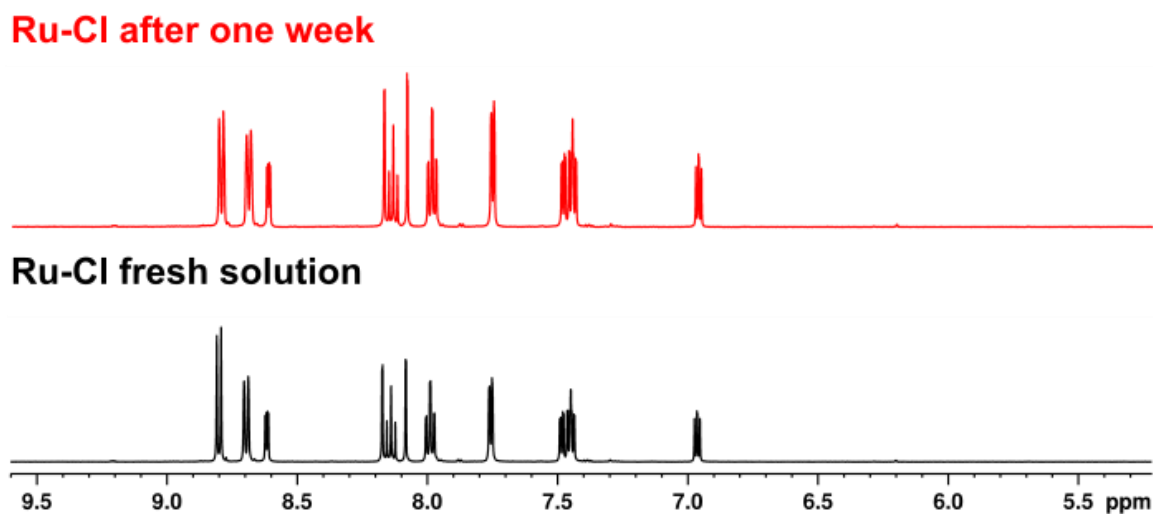


**Figure 20.**  $^1\text{H-NMR}$  spectra of fresh  $\text{cis-}[\text{Ru}^{\text{II}}(\text{Himpz})(\text{tpy})(\text{Cl})]^+$  solution (black) and the same solution after one week (red) recorded in  $\text{DMSO-d}_6$  at 500 MHz.

The  $^1\text{H-NMR}$  spectrum of the complex  $[\text{Ru}^{\text{II}}(\text{Himpa})(\text{tpy})(\text{OH}_2)](\text{PF}_6)_2$  in  $\text{DMSO-d}_6$  is shown in **Figure 21b**. Like previous aqua complex bearing the Himpy ligand, all the signals were downfield regarding the chlorido complex. The aqua protons resonance lies at 5.94 ppm as a singlet signal. Chemical shifts, coupling constants, multiplicities and integrations are summarized in **Table 8**.

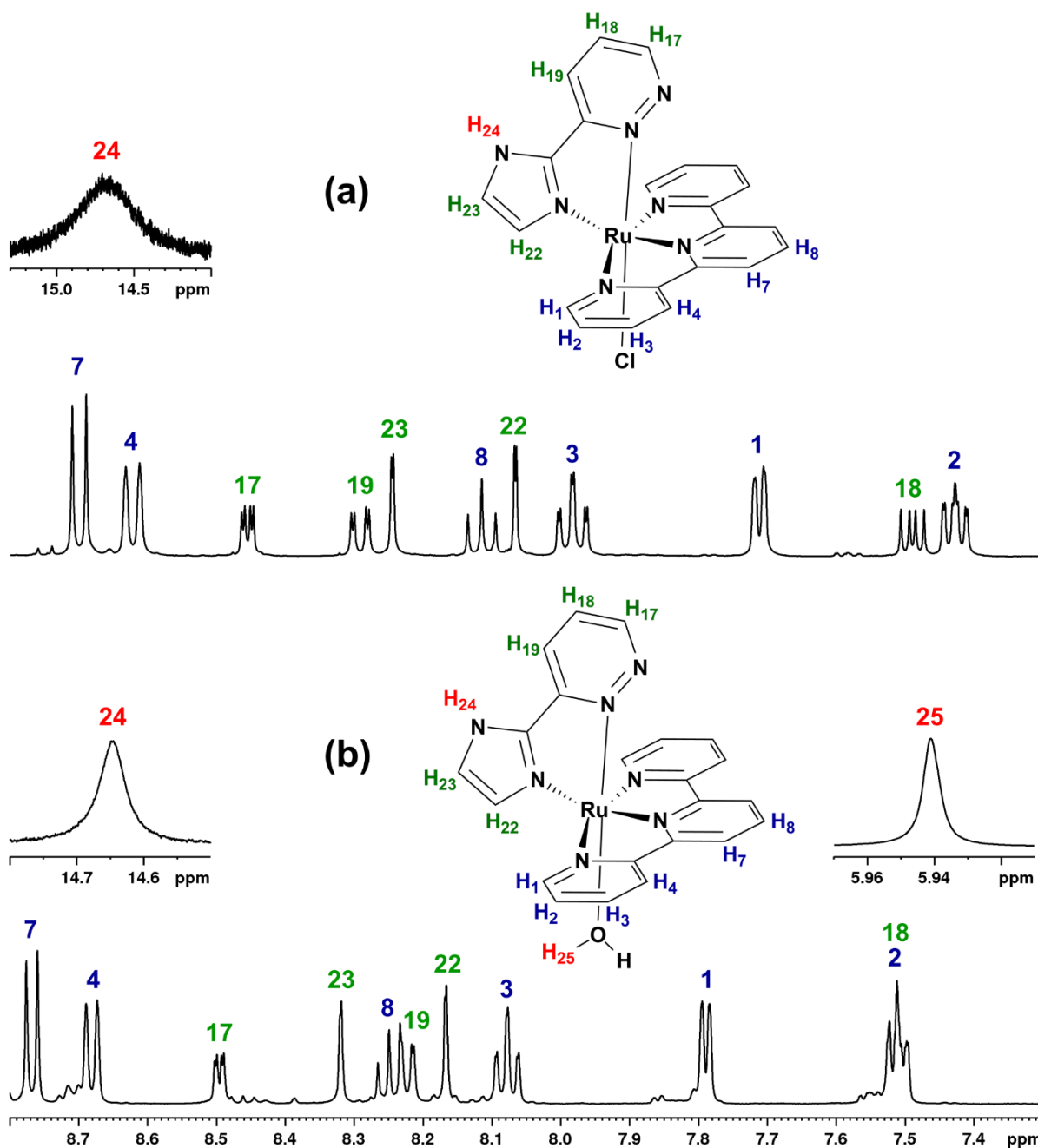


**Figure 21.**  $^1\text{H-NMR}$  spectra of (a)  $[\text{Ru}^{\text{II}}(\text{Himpa})(\text{tpy})(\text{Cl})]^+$  and (b)  $[\text{Ru}^{\text{II}}(\text{Himpa})(\text{tpy})(\text{OH}_2)]^{2+}$  complexes recorded in  $\text{DMSO-d}_6$  at 400 MHz.

**Table 8.**  $^1\text{H-NMR}$  data for  $[\text{Ru}^{\text{II}}(\text{Himpa})(\text{tpy})(\text{Cl})]^+$  and  $[\text{Ru}^{\text{II}}(\text{Himpa})(\text{tpy})(\text{OH}_2)]^{2+}$  complexes recorded in  $\text{DMSO-d}_6$ .

Compound	Hydrogen	Splitting pattern	Integration	Chemical shift (ppm)	Coupling constant (Hz)
Chlorido complex	24	s	1	14.68	-
	7	d	2	8.70	8.0
	4	d	2	8.62	8.0
	17	dd	1	8.45	5.0, 1.2
	19	dd	1	8.29	8.4, 1.8
	23	d	1	8.24	1.2
	8	t	1	8.12	8.0
	22	d	1	8.06	1.2
	3	td	2	7.98	7.8, 1.4
	1	dd	2	7.71	5.4, 0.7
	18	dd	1	7.47	8.5, 5.0
	2	ddd	2	7.43	7.9, 5.6, 1.2
Aqua complex	24	s	1	14.64	-
	7	d	2	8.77	8.1
	4	d	2	8.68	8.0
	17	dd	1	8.49	5.0, 1.7
	23	d	1	8.32	1.2
	8	t	1	8.25	8.1
	19	dd	1	8.22	8.3, 1.7
	22	d	1	8.16	1.0
	3	td	2	8.07	7.9, 1.2
	1	d	2	7.79	5.4
18, 2	m	3	7.51	-	
16	s	2	5.94	-	

### 4.3 X-ray crystallography

The structures of the *cis* and *trans* isomers of the  $[\text{Ru}^{\text{II}}(\text{Himpa})(\text{tpy})(\text{OH}_2)]^{2+}$  complex were solved by single X-ray crystallography as shown in **Figure 22** and the crystallographic data are summarized in **Table 9**. It is worth mentioning that crystals of both isomers were obtained from the attempts of synthesis of the *cis*-aqua complex because by the time the *cis*-chlorido complex was obtained in large quantity whereas some milligrams of the *trans*-chlorido complex were available. Surprisingly, crystals of the *trans* isomer were afforded after finishing the synthesis, but this event was not unexpected as the reaction, one of the first attempts in this Thesis, was started with a mixture of the *cis* and *trans* chlorido isomers to achieve the appropriate conditions to obtain the aqua complex. The overall structures were quite similar to the chlorido

complexes, with the meridional mode of bonding of the terpyridine, the Himpy ligand coordinated in perpendicular position ( $96.46^\circ$ ) regarding the terpyridine, and the aqua ligand in axial position. In all these chlorido and aqua complexes, the geometrical constraints imposed by the meridional coordinating behavior of the terpyridine are noted by the trans angles  $N_{\text{tpy}}\text{-Ru-}N'_{\text{tpy}}$  close to  $158^\circ$  whereas the trans angles  $N_{\text{tpy}}\text{-Ru-}N_{\text{Himpy}}$  are almost  $180^\circ$ . The central  $\text{Ru-}N_{\text{tpy}}$  bond lengths [ $1.946\text{-}1.958 \text{ \AA}$ ] are shorter than the corresponding terminal  $\text{Ru-}N_{\text{tpy}}$  bond lengths [ $2.056\text{-}2.073 \text{ \AA}$ ]. All these characteristics agree with reported data for related terpyridine-containing ruthenium complexes.<sup>53</sup>

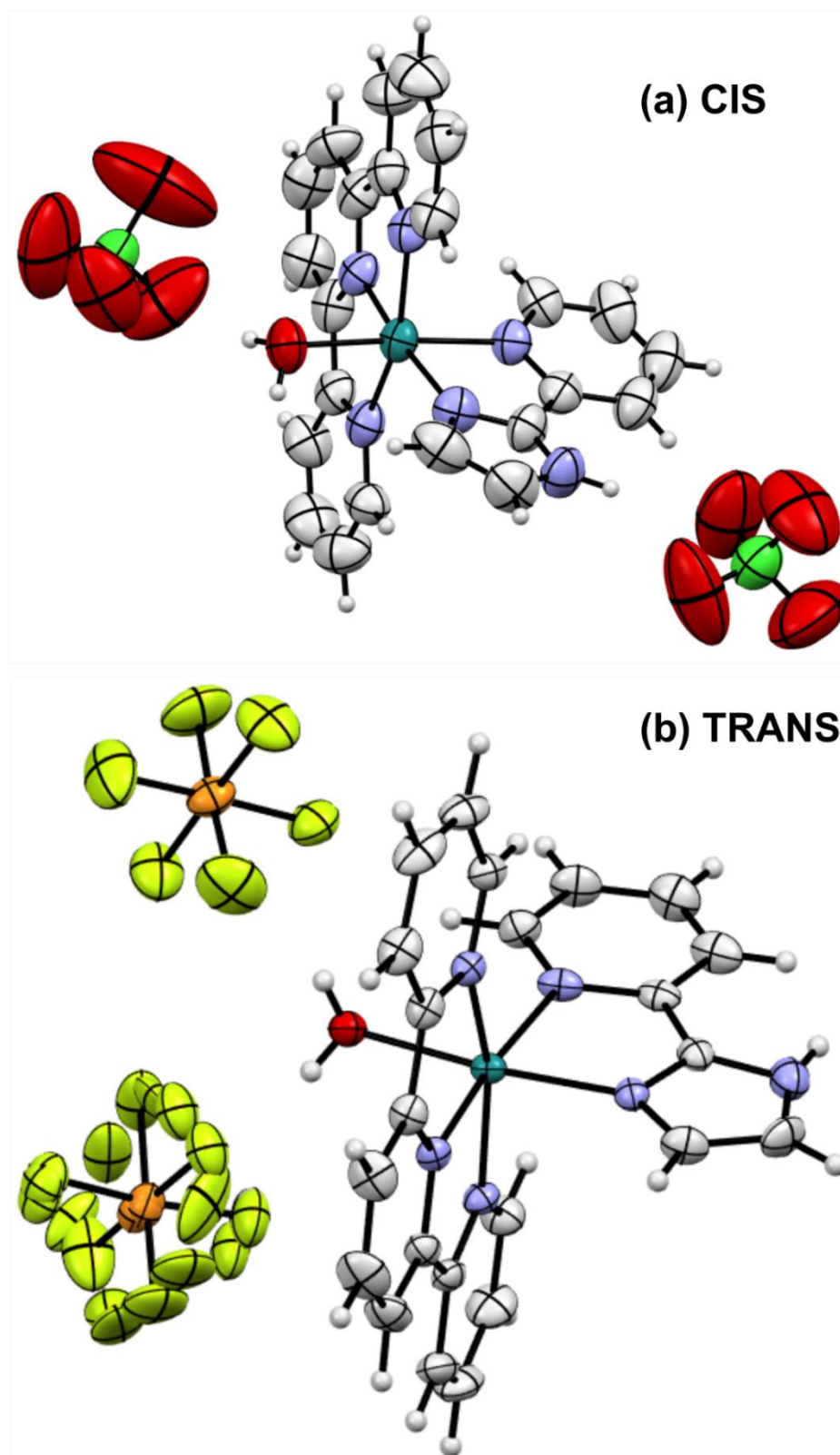


**Figure 22.** ORTEP view of the X-ray structure of *cis*- $[Ru^{II}(Himpy)(tpy)(OH_2)](ClO_4)_2$  and *trans*- $[Ru^{II}(Himpy)(tpy)(OH_2)](PF_6)_2$  at 150K. Atoms are colored as follows: Carbon (gray), nitrogen (blue), hydrogen (soft gray), oxygen (red), ruthenium (teal), phosphorous (orange), chlorine (green), fluorine (yellow).

**Table 9.** Crystallographic data for the *cis*-[Ru<sup>II</sup>(Himpy)(tpy)(OH<sub>2</sub>)](ClO<sub>4</sub>)<sub>2</sub> and *trans*-[Ru<sup>II</sup>(Himpy)(tpy)(OH<sub>2</sub>)](PF<sub>6</sub>)<sub>2</sub> complexes.

Parameter	<i>cis</i> - [Ru(Himpy)(tpy)(OH <sub>2</sub> )](ClO <sub>4</sub> ) <sub>2</sub>	<i>trans</i> - [Ru(Himpy)(tpy)(OH <sub>2</sub> )](PF <sub>6</sub> ) <sub>2</sub>
<b>Empirical formula</b>	C <sub>23</sub> H <sub>20</sub> N <sub>6</sub> Cl <sub>2</sub> O <sub>9</sub> Ru	C <sub>23</sub> H <sub>20</sub> N <sub>6</sub> OP <sub>2</sub> F <sub>12</sub> Ru
<b>Fw</b>	696.42	787.61
<b>Crystal symmetry</b>	Monoclinic	Monoclinic
<b>Space group</b>	P 21/n	P 21/n
<b>a (Å)</b>	7.9619(3)	8.0212(10)
<b>b (Å)</b>	17.5384(7)	18.133(2)
<b>c (Å)</b>	19.5693(7)	19.817(3)
<b>α (°)</b>	90	90
<b>β (°)</b>	99.881(2)	101.148(4)
<b>γ (°)</b>	90	90
<b>V (Å<sup>3</sup>)</b>	2692.10(18)	2828.0(6)
<b>Z</b>	4	4
<b>T (K)</b>	150	150

#### 4.4 UV-visible spectroscopy

The electronic properties of the ruthenium(II) aqua complexes were studied by UV-vis spectroscopy and their absorption spectra in aqueous solution are shown in **Figure 23**. Like previous ruthenium chlorido complexes, all the aqua complexes show narrow, strong absorption bands in the UV region assigned to  $\pi \rightarrow \pi^*$  ligand transitions, and the visible region is characterized by broad, weak absorption bands attributed to MLCT transitions from the  $d\pi(\text{Ru})$  orbital to the  $\pi^*$  orbital of either terpyridine or Himpx ligands.

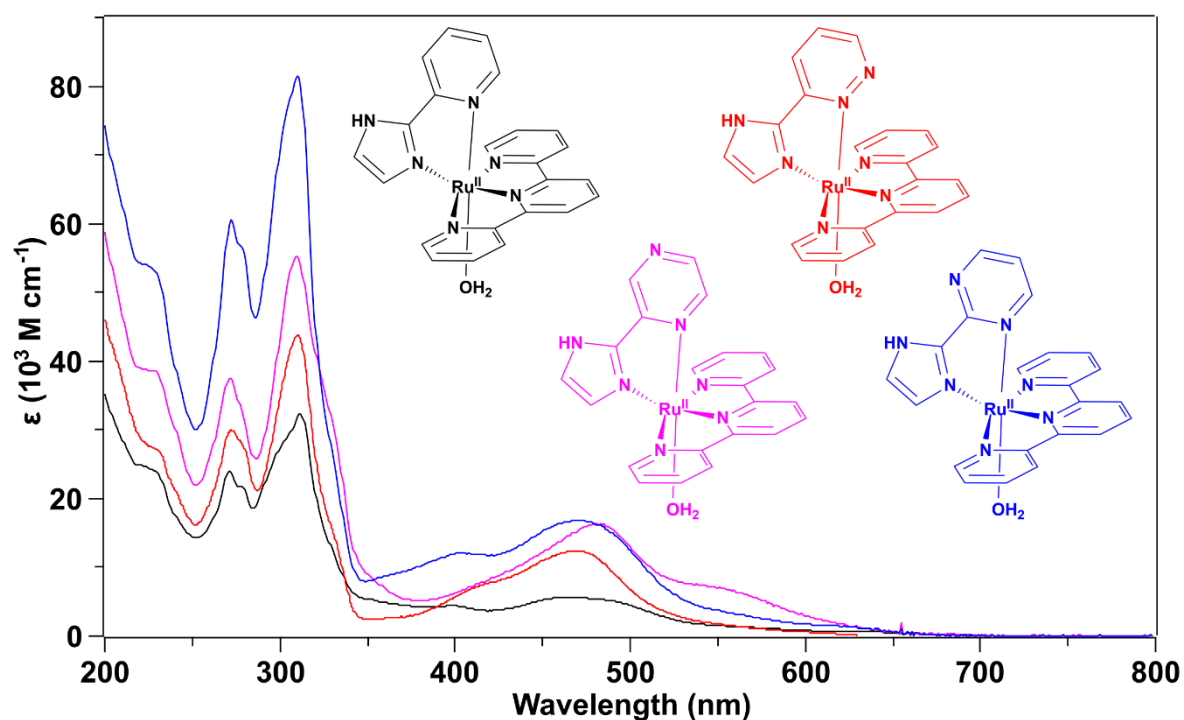


**Figure 23.** UV-visible spectra of ruthenium(II) aqua complexes in water.

In all cases, substitution of chlorido by an aqua ligand causes a blue shift of MLCT transitions in the complexes (**Figure 24**), which stem from stabilization of the  $d\pi(\text{Ru})$  orbital leading to an increase of energy demand for  $d\pi(\text{Ru}) \rightarrow \pi^*(\text{ligand})$  transition. UV vis spectra was plotted in absorbance units in “y” axis because chlorido complexes were not completely soluble in water.

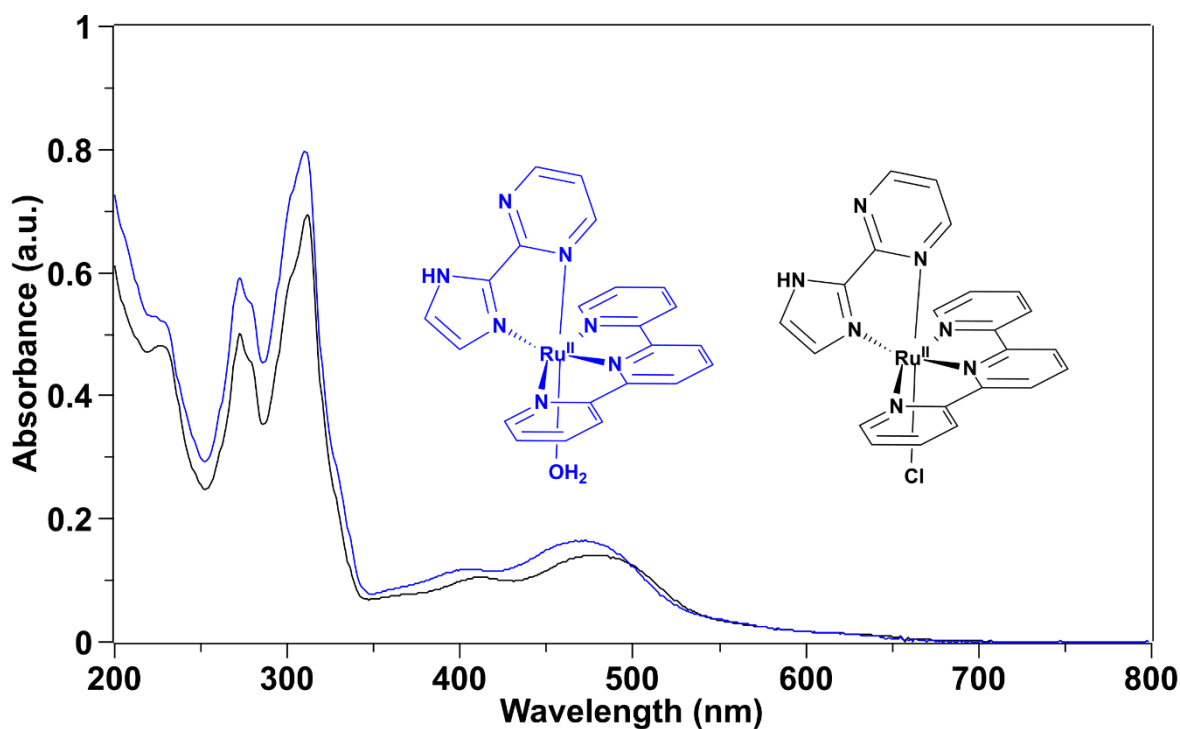


**Figure 24.** UV-visible spectra of  $[\text{Ru}^{\text{II}}(\text{Himp})(\text{tpy})(\text{Cl})]^+$  (black) and  $[\text{Ru}^{\text{II}}(\text{Himp})(\text{tpy})(\text{OH}_2)]^{2+}$  (blue) in water.

#### 4.5 $pK_a$ of $\text{Ru}(\text{II})$ aqua complexes

**Figure 25** shows the spectrophotometric curves at different pH for  $[\text{Ru}^{\text{II}}(\text{Himp})(\text{tpy})(\text{OH}_2)]^{2+}$  complex displaying four isosbestic points at 405, 443, 500 and 510 nm. The  $pK_a$  values obtained, indicated in the inset figure as 9.14 and 11.01, are well correlated with these two equilibria. According to the first case studied for the chlorido complex, the first deprotonation at  $pK_a$  9.14 should be in the Himp ligand, giving the  $[\text{Ru}^{\text{II}}(\text{imp})(\text{tpy})(\text{OH}_2)]^+$  species, and the second deprotonation is attained to the aqua ligand. Deprotonation causes a larger bathochromic shift on the MLCT bands from 464 to 525 nm compared to that of the chlorido complex, displaying the better  $\pi$ -donor properties not only of the imp $^-$  moiety but also of the  $\text{OH}^-$  ligand on the complex.

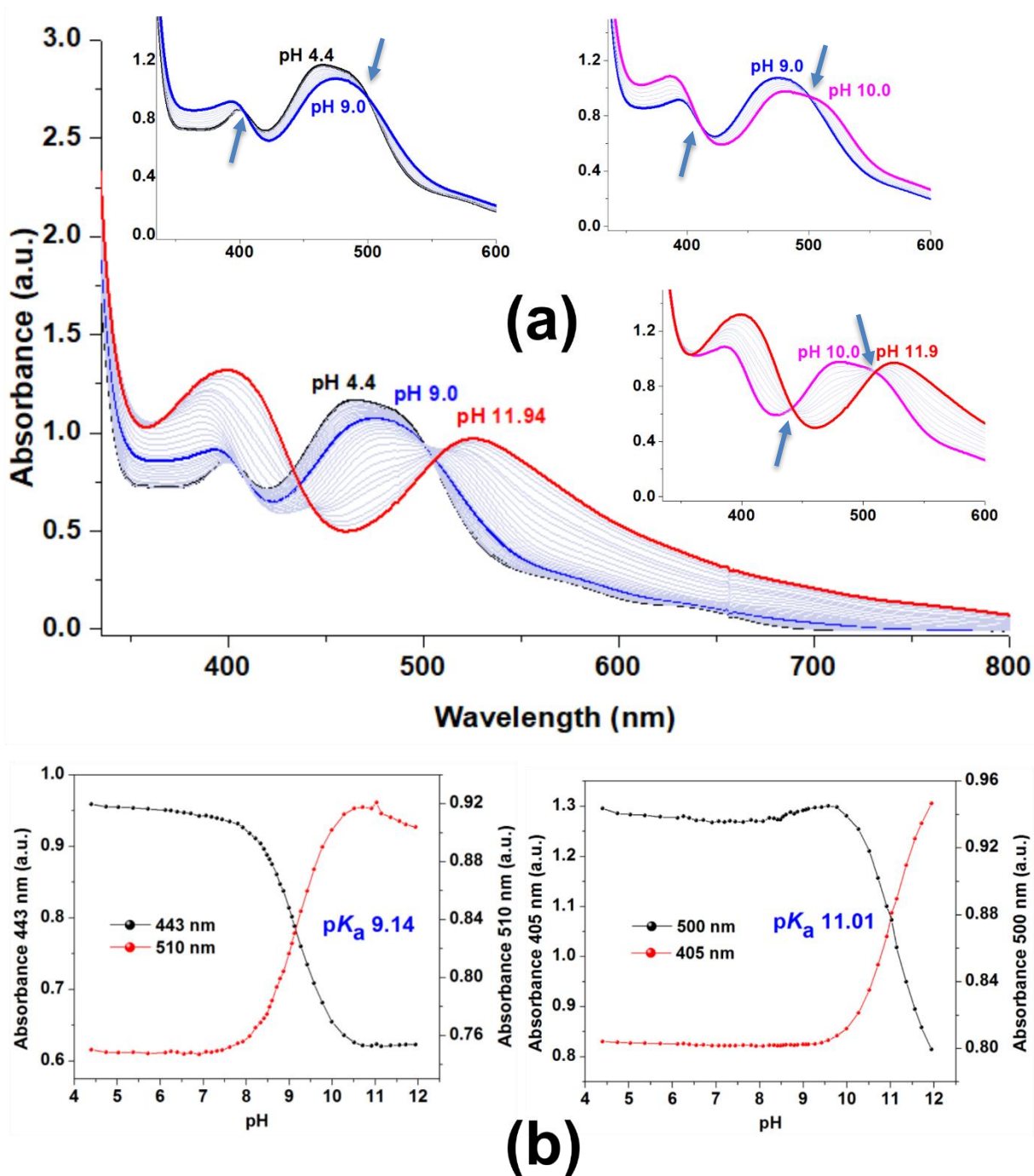


**Figure 25.** (a) Absorption bands changes of  $[\text{Ru}^{\text{II}}(\text{Himpy})(\text{tpy})(\text{OH}_2)]^{2+}$  ( $160 \mu\text{M}$ ) in  $0.04 \text{ M}$  Britton–Robinson buffer after titrating with  $4 \text{ M}$  NaOH solution in pH range from 4.4 to 11.94. Inset: Isosbestic points indicating protonated and deprotonated species in equilibrium along pH range. (b) Plot of absorbances at 405 and 500 nm versus pH.

#### 4.6 Electrochemistry of Ru(II) complexes

The choice for the aqua complexes was made based on the important role that aqua ligand plays in the catalytic process of water oxidation as it has direct involvement in the catalytic mechanism.<sup>82</sup> The chlorido complexes are not as good catalysts as the aqua complexes because the chlorido ligand does not participate directly in the O–O bonding formation like aqua ligand does. Such performance can be observed in **Figure 26**, which shows a lower onset potential (lower energy to catalyze water oxidation) as well as a higher catalytic current for the aqua complex  $[\text{Ru}^{\text{II}}(\text{Himpy})(\text{tpy})(\text{OH}_2)]^{2+}$  compared to that of the chlorido complex  $[\text{Ru}^{\text{II}}(\text{Himpy})(\text{tpy})(\text{Cl})]^+$ .

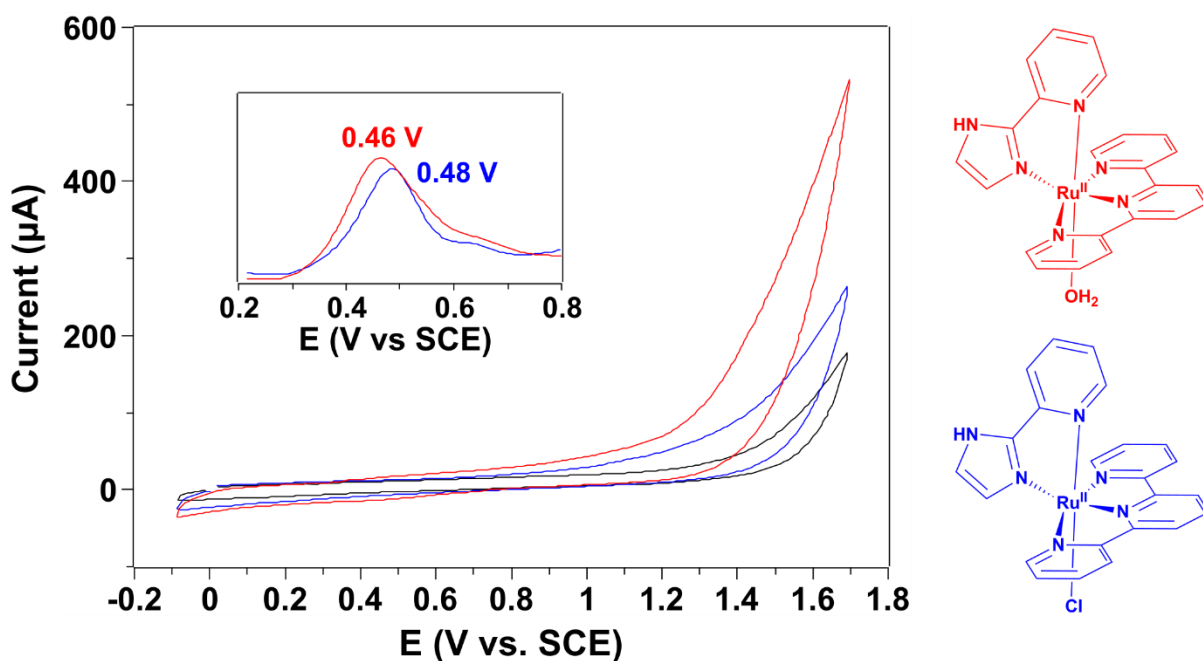


**Figure 26.** Cyclic voltammograms displaying the better performance of the aqua complex (red) over the chlorido complex (blue) at pH 8. Blank cyclic voltammogram is also displayed (black). Scan rate:  $0.1 \text{ V s}^{-1}$ . Inset plot: DPV showing the  $\text{Ru}^{\text{II}}/\text{Ru}^{\text{III}}$  redox potential for both complexes.

Cyclic voltammograms of  $[\text{Ru}^{\text{II}}(\text{Himpy})(\text{tpy})(\text{OH}_2)]^{2+}$  (**1**) and  $[\text{Ru}^{\text{II}}(\text{Himpa})(\text{tpy})(\text{OH}_2)]^{2+}$  (**2**) complexes are shown in **Figure 27**. The inset plot shows two signals appearing at 0.46 V and 0.52 V attributed to  $\text{Ru}^{\text{II}}/\text{Ru}^{\text{III}}$  process for (**1**) and (**2**) complexes, respectively. The main figure also shows the lower onset potential necessary for complex (**1**) (ca. 1.2 V vs SCE), compared to (**2**) (ca. 1.35 V vs SCE), to perform water oxidation. The lower potential value for the  $\text{Ru}^{\text{II}}/\text{Ru}^{\text{III}}$  redox process in (**1**) and its lower onset potential is associated to the higher basicity of Himpy ligand

over the Himpa ligand, which clearly shows the influence of the donor properties of Himpx ligands on electrochemical properties of the Ru<sup>II</sup> complexes.

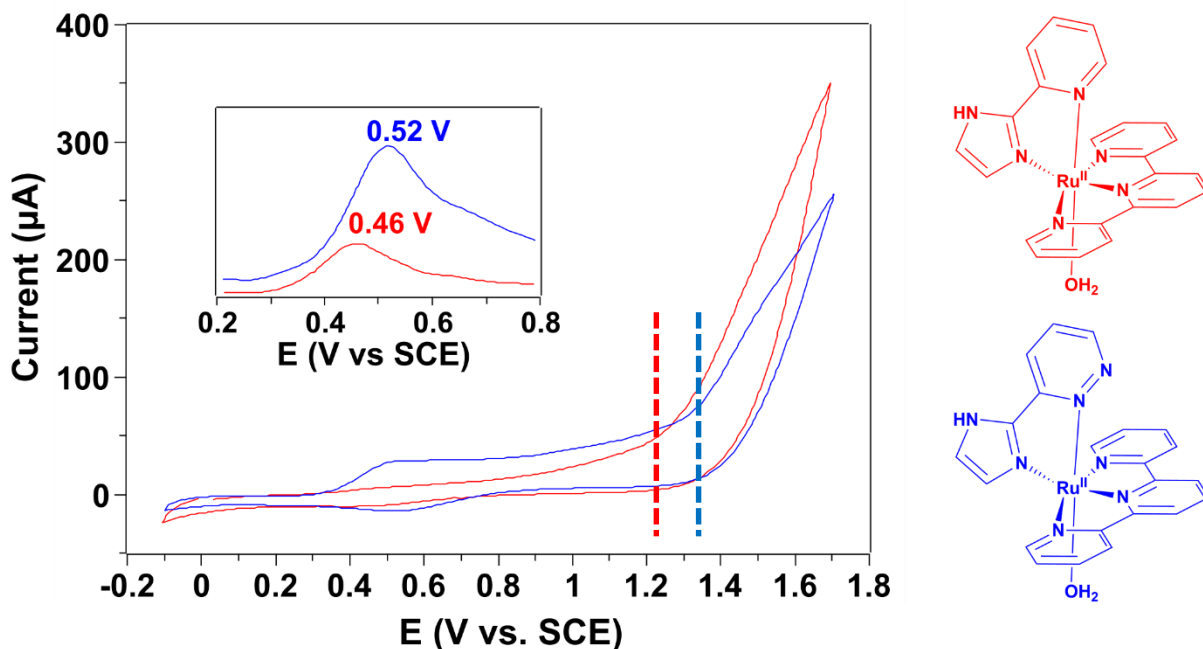


**Figure 27.** Cyclic voltammograms of  $[\text{Ru}^{\text{II}}(\text{Himpy})(\text{tpy})(\text{OH}_2)]^{2+}$  (red) and  $[\text{Ru}^{\text{II}}(\text{Himpa})(\text{tpy})(\text{OH}_2)]^{2+}$  (blue) at pH 8. Blank current was subtracted for both complexes. Dashed lines indicate the onset potential for water oxidation. Inset plot: DPV showing the Ru<sup>II</sup>/Ru<sup>III</sup> redox potential for both complexes. Scan rate 0.1 V s<sup>-1</sup>.

In order to investigate the dependence of the redox properties on pH for the ruthenium aqua complexes, differential pulse voltammograms (DPV) and square wave voltammograms (SWV) over the pH 2–10 were recorded and displayed in **Figure 28**. The first noticeable feature found in all voltammograms is the shift of peak potentials to lower energies as the pH increases, which agrees with the availability of more electronic density on ligands as deprotonation takes place. The second characteristic observed in all cases is the lower peak potential for **(1)** among the complexes, which is well correlated with the higher basicity of Himpy ligand over the Himpx ligand series. Throughout the pH range 2–10, three redox events are observed in all voltammograms. The first two peak potentials are usually assigned to Ru<sup>III</sup>/Ru<sup>II</sup> and Ru<sup>IV</sup>/Ru<sup>III</sup> couples for similar complexes.<sup>72,83,84</sup> In this Thesis, the second assignment depends on pH region and will be described later. The last redox event is not as much pronounced as the first two ones because it arises near the onset potential of water

oxidation. This third peak potential was quite often associated to oxidation of  $\text{Ru}^{\text{IV}}$  to  $\text{Ru}^{\text{V}}$  on related complexes, but it was shown on our group member-Gabriel's master work that was not the case for the complexes studied in this Thesis, and will be briefly detailed in the next paragraph. The different species involved in pH dependence-redox events are displayed in Pourbaix diagrams (**Figure 29–Figure 32**).

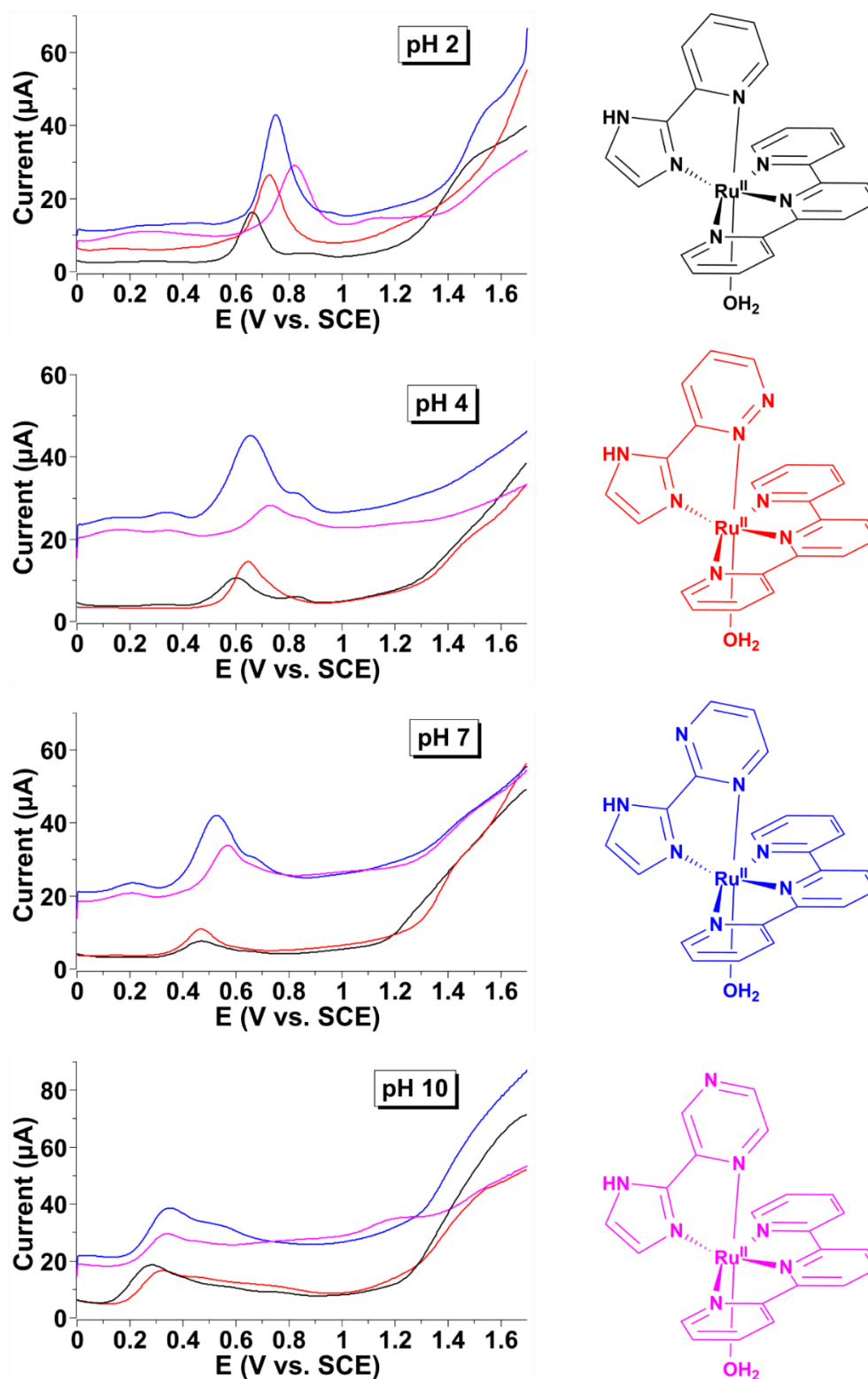


**Figure 28.** DPV of  $[\text{Ru}^{\text{II}}(\text{Himpy})(\text{tpy})(\text{OH}_2)]^{2+}$  (black) and  $[\text{Ru}^{\text{II}}(\text{Himpa})(\text{tpy})(\text{OH}_2)]^{2+}$  (red), and SWV of  $[\text{Ru}^{\text{II}}(\text{Himpm})(\text{tpy})(\text{OH}_2)]^{2+}$  (blue) and  $[\text{Ru}^{\text{II}}(\text{Himpz})(\text{tpy})(\text{OH}_2)]^{2+}$  (pink) at pH 2–10. Electrolyte: 0.04 M Britton–Robinson + 0.1 M  $\text{KNO}_3$ . WE: GCE. RE: SCE. CE: Pt.

The Pourbaix diagram of  $[\text{Ru}^{\text{II}}(\text{Himpy})(\text{tpy})(\text{OH}_2)]^{2+}$  (**1**) (**Figure 29**), which was built by plotting the potentials obtained from DPV versus pH of the solutions,

displays many redox processes dependent on pH that exhibits their proton-coupled electron transfer (PCET) properties as expected based on the acid–base characteristics of the heteroaryl imidazole ligands changing with the potential applied. The Ru<sup>II</sup>/Ru<sup>III</sup> redox potential shifted to negative potential from 0.65 to 0.15 V as the pH increased up to 11 where, according to the obtained p*K*<sub>a</sub> values of 9.14 and 11.01, two deprotonation processes took place. The p*K*<sub>a</sub> value of 9.14 is confirmed in the diagram as an inflection observed at that pH giving rise to the first deprotonated species [Ru<sup>II</sup>(impy)(tpy)(OH<sub>2</sub>)]<sup>+</sup> (Ru<sup>II</sup>LOH<sub>2</sub>).

In the pH region 0–3, contrary to expected, the oxidation process was not in the metal center (Ru<sup>III</sup>/Ru<sup>IV</sup>) but was ligand-centered. The assignment was only possible employing DFT calculations on the electron density of the complex in these conditions, showing that going further this pH region the oxidation already occurs in the metal center as its oxidation state is stabilized by the enhanced electron density of the oxo ligand. Furthermore, the oxidation still remains ligand-centered at potentials higher than 1.4 V, contrary to other related complexes, where oxidation takes place on metal center affording Ru<sup>V</sup> species.

Vertical inflections indicate the p*K*<sub>a</sub> values for a specific couple and one H<sup>+</sup> deprotonation is expected; however, a different pattern seemed to occur at pH 3 going from 0.85 to 1.4 V (**Figure 29**). After the vertical line at pH 3, the Ru<sup>III</sup>L<sup>ox</sup>OH intermediate was expected as the conjugated base from Ru<sup>III</sup>L<sup>ox</sup>OH<sub>2</sub>, but the Ru<sup>IV</sup>LO was formed instead. This issue was unraveled by DFT calculations, which showed that the p*K*<sub>a</sub> for Ru<sup>III</sup>L<sup>ox</sup>OH<sub>2</sub>/Ru<sup>III</sup>L<sup>ox</sup>OH and Ru<sup>III</sup>L<sup>ox</sup>OH/Ru<sup>IV</sup>LO couples are 3.76 and 3.67, respectively, displaying an equilibrium among those species which is reflected in that peculiar pattern.

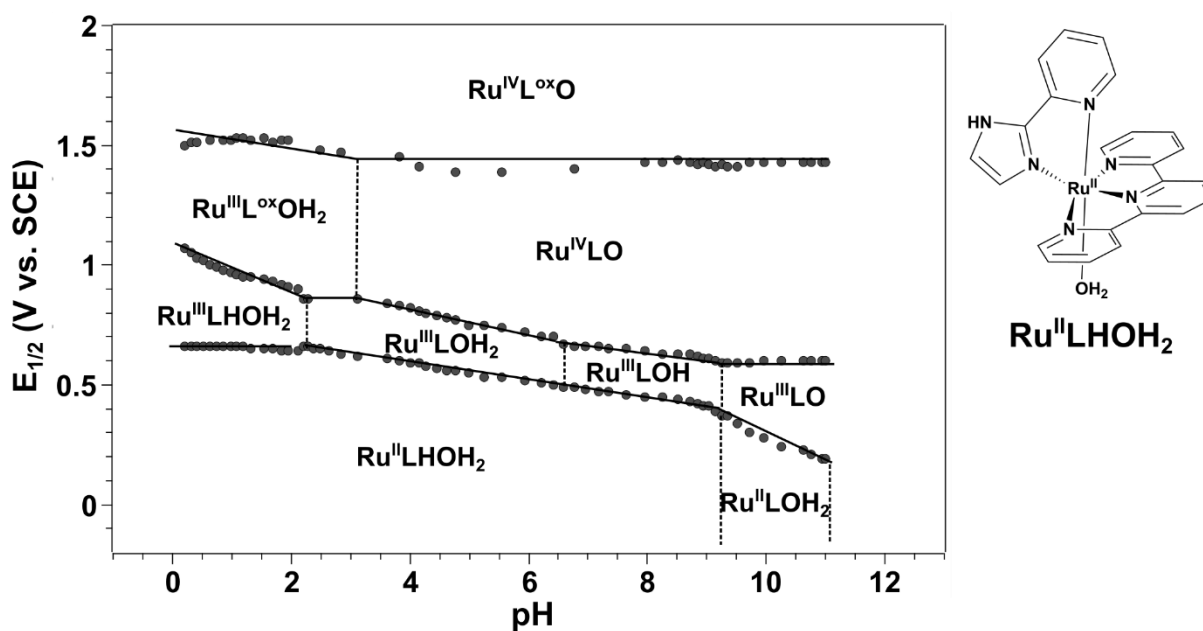


**Figure 29.** Pourbaix diagram of **(1)** (1 mM) in 0.04 M Britton–Robinson buffer + 0.1 M  $\text{KNO}_3$  solution.

The Pourbaix diagram of  $[\text{Ru}^{\text{II}}(\text{Himpa})(\text{tpy})(\text{OH}_2)]^{2+}$  **(2)** (**Figure 30**) displays some similarities to that of complex **(1)**. There are many redox processes dependent on pH, with 3 events occurring at each pH. The  $\text{p}K_{\text{a}}$  values of 9 and 11 for  $\text{Ru}^{\text{II}}$  intermediates are also close to **(1)**, as shown in section 4.5. Nevertheless, the potential for  $\text{Ru}^{\text{III}}/\text{Ru}^{\text{II}}$  redox couple is lower for complex **(1)** over the whole pH range. Additionally, in complex **(1)**, the energy necessary to reach  $\text{Ru}^{\text{IV}}$  species from  $\text{Ru}^{\text{II}}$  is  $\Delta E_{1/2} = 0.2$  V (at pH 3–9), whereas for complex **(2)** this energy is higher ( $\Delta E_{1/2} = 0.45$  V, pH 3–9), evidencing a better electron density contribution from Himpy over Himpa ligand. This last characteristic is quite important in water oxidation performance, as evidenced in **Figure 26**, where a lower onset potential for starting the catalysis is required for complex **(1)** when compared to **(2)** at pH 8, as well as a higher catalytic current produced.

The Pourbaix diagrams for  $[\text{Ru}^{\text{II}}(\text{Himpm})(\text{tpy})(\text{OH}_2)]^{2+}$  **(3)** and  $[\text{Ru}^{\text{II}}(\text{Himpz})(\text{tpy})(\text{OH}_2)]^{2+}$  **(4)** are shown in **Figure 31** and **Figure 32**, respectively. The assignments were made based on the previous diagrams for complexes **(1)** and **(2)**, as they look like similar when looking the 3 redox events and the profiles in all regions.

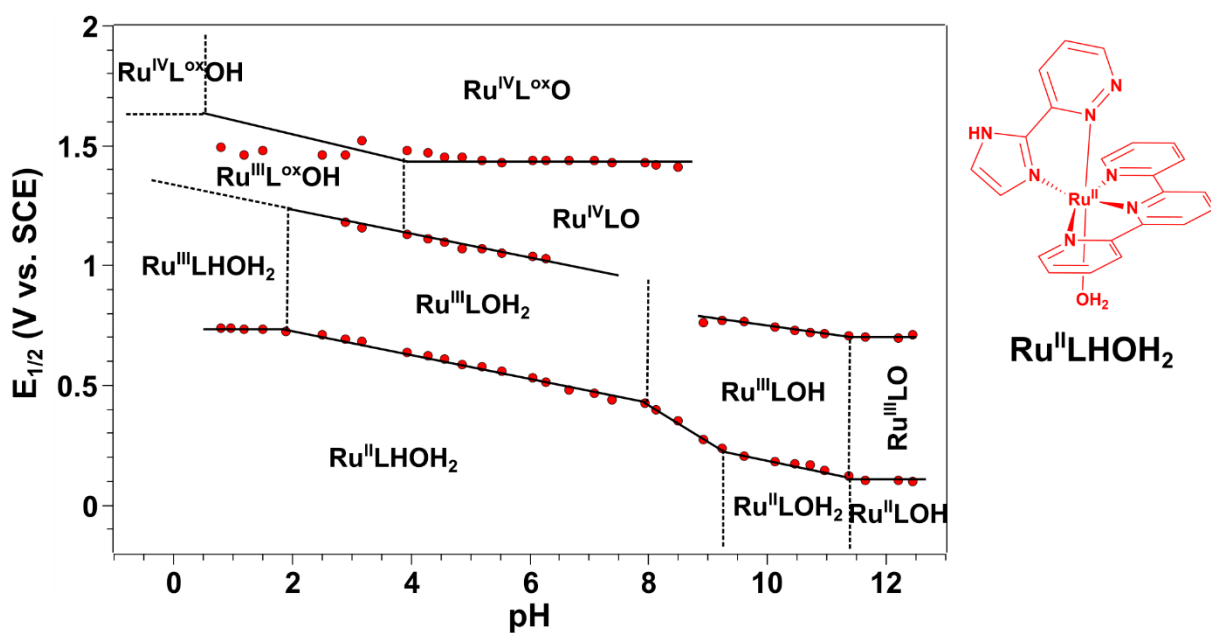


**Figure 30.** Pourbaix diagram of (2) (1 mM) in 0.04 M Britton–Robinson buffer + 0.1 M  $KNO_3$  solution.

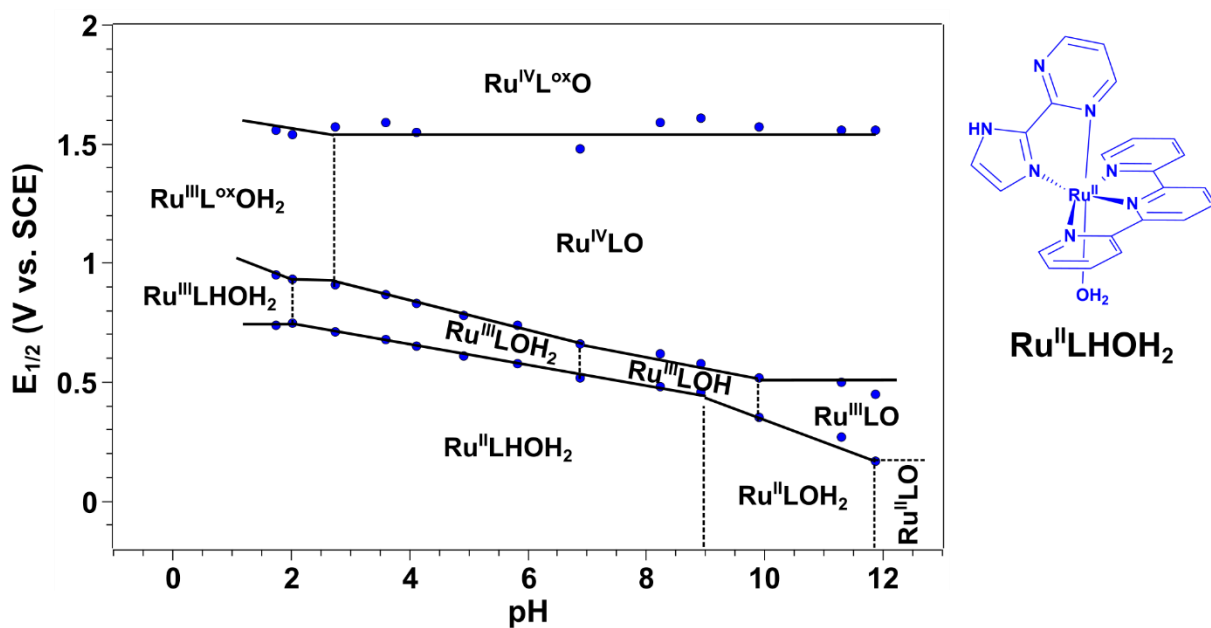


**Figure 31.** Pourbaix diagram of (3) (1 mM) in 0.04 M Britton–Robinson buffer + 0.1 M  $KNO_3$  solution.

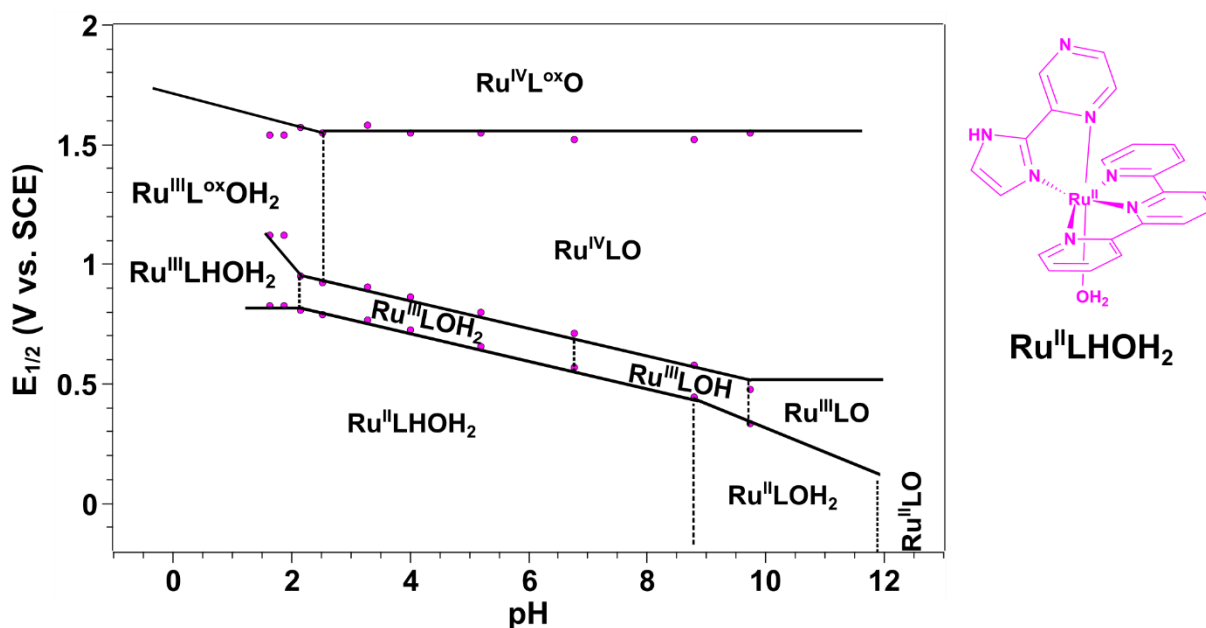


**Figure 32.** Pourbaix diagram of **(4)** (1 mM) in 0.04 M Britton–Robinson buffer + 0.1 M KNO<sub>3</sub> solution.

A comparison was performed among **(1)** and reported Ru(II) complexes containing the bipyrimidine,<sup>72</sup> bipyridine<sup>83</sup> and biimidazole<sup>53</sup> ligands, which also feature PCET properties. Some similarities and differences in Pourbaix diagrams for **(1)** and the  $[Ru^{II}(bpm)(tpy)(OH_2)]^{2+}$ ,  $[Ru^{II}(bpy)(tpy)(OH_2)]^{2+}$  and  $[Ru^{II}(H_2bim)(tpy)(OH_2)]^{2+}$  complexes were found (**Figure 33**). For instance, looking at the intermediates in the diagrams, the two-proton/two-electron process involving Ru<sup>II</sup>/Ru<sup>IV</sup> species was exclusively for  $[Ru^{II}(bpm)(tpy)(OH_2)]^{2+}$  compared to the other complexes. This characteristic was associated to the great electron acceptor behavior of bipyrimidine ligand allowing to stabilize the Ru<sup>II</sup> intermediate over Ru<sup>III</sup>, whereas Ru<sup>IV</sup> intermediate was more stable than Ru<sup>III</sup> because of the high electron donor property of O<sup>2-</sup> ligand. Those two factors influenced in a lower redox potential of Ru<sup>II</sup>/Ru<sup>IV</sup> couple compared to Ru<sup>II</sup>/Ru<sup>III</sup> couple.

The influence of the higher basicity of imidazole compared to pyridine on the electronic properties of the complexes was clearly shown by looking at the Ru<sup>II</sup>/Ru<sup>III</sup> redox potential over the whole pH range. For example, at pH 1, the Ru<sup>II</sup>/Ru<sup>III</sup> redox process was achieved at the lowest potential ( $E_{1/2}$  ca. 0.45 V vs. SCE) for  $[Ru^{II}(H_2bim)(tpy)(OH_2)]^{2+}$ , followed by **(1)** ( $E_{1/2}$  ca. 0.65 V vs. SCE), and finally  $[Ru^{II}(bpy)(tpy)(OH_2)]^{2+}$  ( $E_{1/2}$  ca. 0.80 V vs. SCE), where 2, 1 and no imidazole moieties are in their structures, respectively.

Another outstanding characteristic observed in the Pourbaix diagram was the final oxidized species among the complexes, which is the responsible for the catalytic process of water oxidation. The Ru<sup>V</sup> species was observed for [Ru<sup>II</sup>(bpm)(tpy)(OH<sub>2</sub>)]<sup>2+</sup>, whereas only the Ru<sup>IV</sup> species was achieved for **(1)**, [Ru<sup>II</sup>(bpy)(tpy)(OH<sub>2</sub>)]<sup>2+</sup>, and [Ru<sup>II</sup>(H<sub>2</sub>bim)(tpy)(OH<sub>2</sub>)]<sup>2+</sup> complexes. The complexes containing imidazole in their structure did not achieved the Ru<sup>V</sup> species, but instead obtained an intermediate containing the Ru<sup>IV</sup> species along with the oxidized imidazole ligand ([Ru<sup>IV</sup>(impy<sup>ox</sup>)(tpy)(O)]<sup>2+</sup>). This is probably correlated to a higher electron density availability of imidazole compared to bipyrimidine ligand, turning more plausible to oxidize imidazole over Ru<sup>IV</sup>. This species could have a better performance than the [Ru<sup>V</sup>(bpm)(tpy)(O)]<sup>3+</sup> species in the water oxidation catalysis due to the additional oxidized Himpy ligand that can make the oxo ligand more electrophilic, which in turn can accelerate the reaction.

The electronic properties of the ligands not only influenced in the redox potentials, but also in the p*K*<sub>a</sub> values (depicted as vertical dashed lines). The p*K*<sub>a</sub> related to water for [Ru<sup>II</sup>(Himpy)(tpy)(OH<sub>2</sub>)]<sup>2+</sup> (ca. 11) was higher than that for [Ru<sup>II</sup>(bpy)(tpy)(OH<sub>2</sub>)]<sup>2+</sup> (ca. 9.7).<sup>83</sup> This is correlated to the higher electron donor property of Himpy over bpy ligand, making a weaker Ru<sup>II</sup>–OH<sub>2</sub> bond that in turn makes the H less ionizable. This characteristic was also observed for Ru<sup>III</sup> species, where [Ru<sup>III</sup>(Himpy)(tpy)(OH<sub>2</sub>)]<sup>2+</sup> showed a p*K*<sub>a</sub> of ca. 6.5 for H–OH deprotonation, which was much higher than that for [Ru<sup>III</sup>(bpy)(tpy)(OH<sub>2</sub>)]<sup>2+</sup> (p*K*<sub>a</sub> ca. 1.7).<sup>83</sup> In this case, the p*K*<sub>a</sub> values are more acidic because Ru<sup>III</sup> is more electrophilic than Ru<sup>II</sup>, inducing a stronger bond with OH<sub>2</sub> ligand. Furthermore, the difference between these two Ru<sup>III</sup> complexes (almost 5 pH units) was higher than for Ru<sup>II</sup> complexes (approx. 1 pH unit). This is because bpy has no H ionizable, whereas Himpy does. The Himpy deprotonation occurs at pH ca. 2 (calculated by means of computational measurements and displayed in Pourbaix diagram), leaving more electron density available for Ru<sup>III</sup> that makes the H–OH quite less acidic.

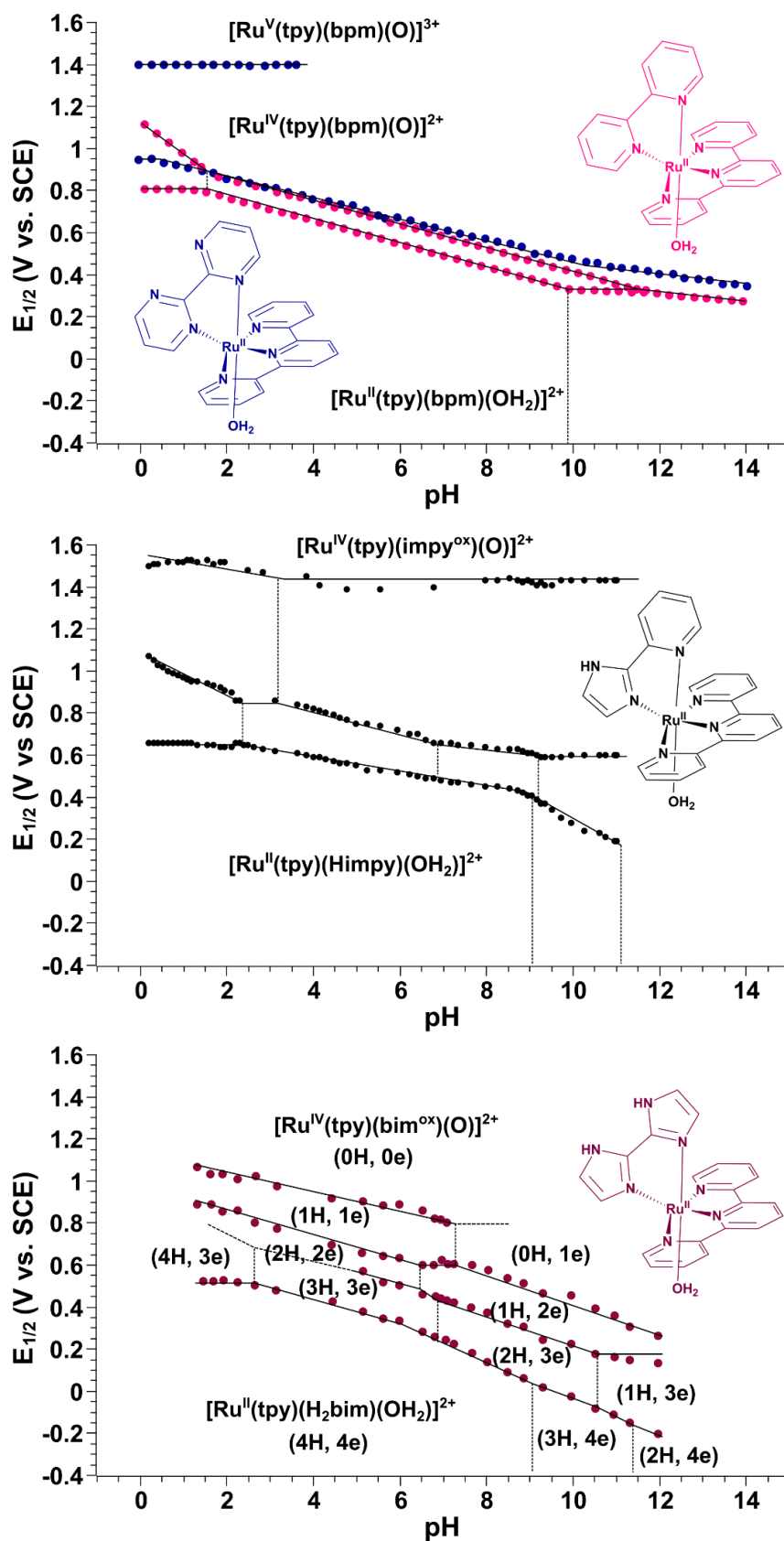


**Figure 33.** Pourbaix diagrams of  $[\text{Ru}^{\text{II}}(\text{Himpy})(\text{tpy})(\text{OH}_2)]^{2+}$ ,  $[\text{Ru}^{\text{II}}(\text{bpm})(\text{tpy})(\text{OH}_2)]^{2+}$ ,  $[\text{Ru}^{\text{II}}(\text{bpy})(\text{tpy})(\text{OH}_2)]^{2+}$  (adapted from Concepcion *et al.*<sup>72</sup>) and  $[\text{Ru}^{\text{II}}(\text{H}_2\text{bim})(\text{tpy})(\text{OH}_2)]^{2+}$  (adapted from Okamura *et al.*<sup>53</sup>) complexes.

## 4.7 Kinetic studies

Chemical water oxidation is usually carried out in presence of cerium(IV) ammonium nitrate (CAN) as the oxidizing agent under acid conditions because of its high redox potential (+1.25 V vs SCE in 0.1 M HNO<sub>3</sub>),<sup>85</sup> which allows the aqua complex to reach high oxidation states that are able to oxidize water. UV-visible spectroscopy was used to get insight into the species formed after the redox reaction of the ruthenium(II) aqua complexes with 1, 2, and 3 equivalents of CAN. Figure 34 shows the spectra of [Ru<sup>II</sup>(Himpy)(tpy)(OH<sub>2</sub>)<sup>2+</sup> [(1)<sup>2+</sup>, black] and the different species formed after reacting with CAN. A solution of (1)<sup>2+</sup> (2 mL, 25 μM) was prepared and transferred to a UV-vis cuvette. Then, 21.4 μL of 1.9 mM CAN solution (1 Eq) was added to the cuvette, and the spectra were acquired every 10 seconds (dotted curves) over 5 minutes, where the final spectrum (solid curve in red) was related to the species (1)<sup>3+</sup>. Another 1 Eq of CAN was added to the cuvette and the spectra acquired over 5 minutes until obtaining the final spectrum [blue, (1)<sup>4+</sup>]. Finally, one more equivalent of CAN was added to the cuvette, recording the spectra over 5 minutes until the final spectrum [(1)<sup>5+</sup>, pink]. After the addition of 1 equivalent of CAN to complex solution, the absorbance intensity decreased in the 290–320 nm region as well as the MLCT band was almost depleted as observed in **Figure 34**. This pronounced decreasing in the MLCT band agrees with the produced Ru<sup>III</sup> species which possess low electronic density compared to Ru<sup>II</sup> species. The appearing isosbestic points at 275 and 322 nm also confirmed the presence of a new formed species. Further addition of 1 equivalent of CAN to complex solution induced minor changes in the π → π\* ligand and MLCT absorption bands (spectrum in blue color).

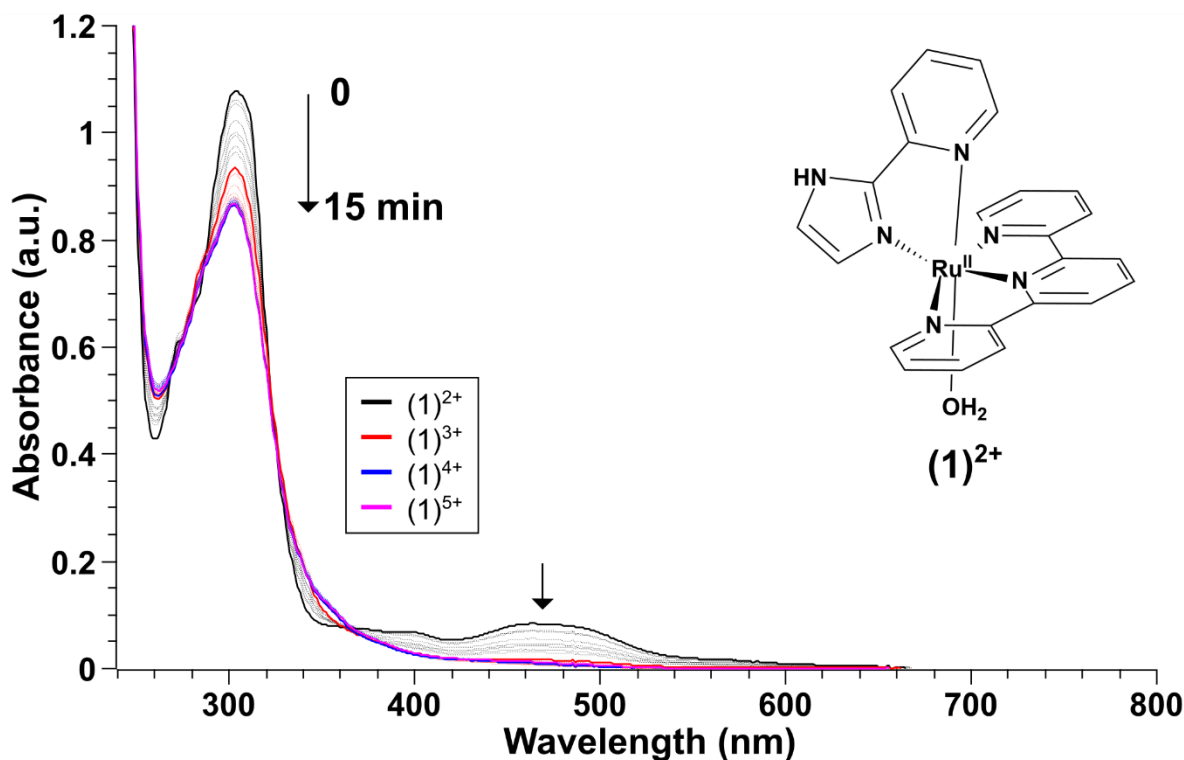


**Figure 34.** UV-visible spectral changes (10 s intervals) upon addition of 1, 2, and 3 equivalents of  $\text{Ce}^{\text{IV}}$  to  $[\text{Ru}^{\text{II}}(\text{Himpy})(\text{tpy})(\text{OH}_2)]^{2+}$  ( $25 \mu\text{M}$ ) over 15 minutes.

Despite no visible changes were observed upon addition of 1 more equivalent of CAN to complex solution, isosbestic points at 298 and 339 nm indicated that a different species was produced (**Figure 35**). The small variations in absorbance could probably be associated with a slow rate constant, which makes the reaction requiring more time to observe major changes. Another important feature is related to absorbance changes during the reaction with CAN. The continuous decreasing absorbance throughout the first 10 minutes of reaction (**Figure 35**, inset) was also observed in Concepcion's work<sup>84</sup> where a further reaction of  $[\text{Ru}^{\text{V}}(\text{tpy})(\text{bpm})(\text{O})]^{3+}$  complex with water was proposed to explain the spectral changes over 1 h of reaction followed by an increasing of absorbance at 283 nm. In this Thesis, the oxidation with 3 equivalents of CAN was not followed for such a long time to confirm the other species involved in the whole mechanism for water oxidation. Regardless of not having the whole picture, a similar trend was observed in the beginning of the experiment, allowing to propose, along with the Pourbaix diagram displayed in **Figure 29**, the redox events displayed in **Figure 36**.

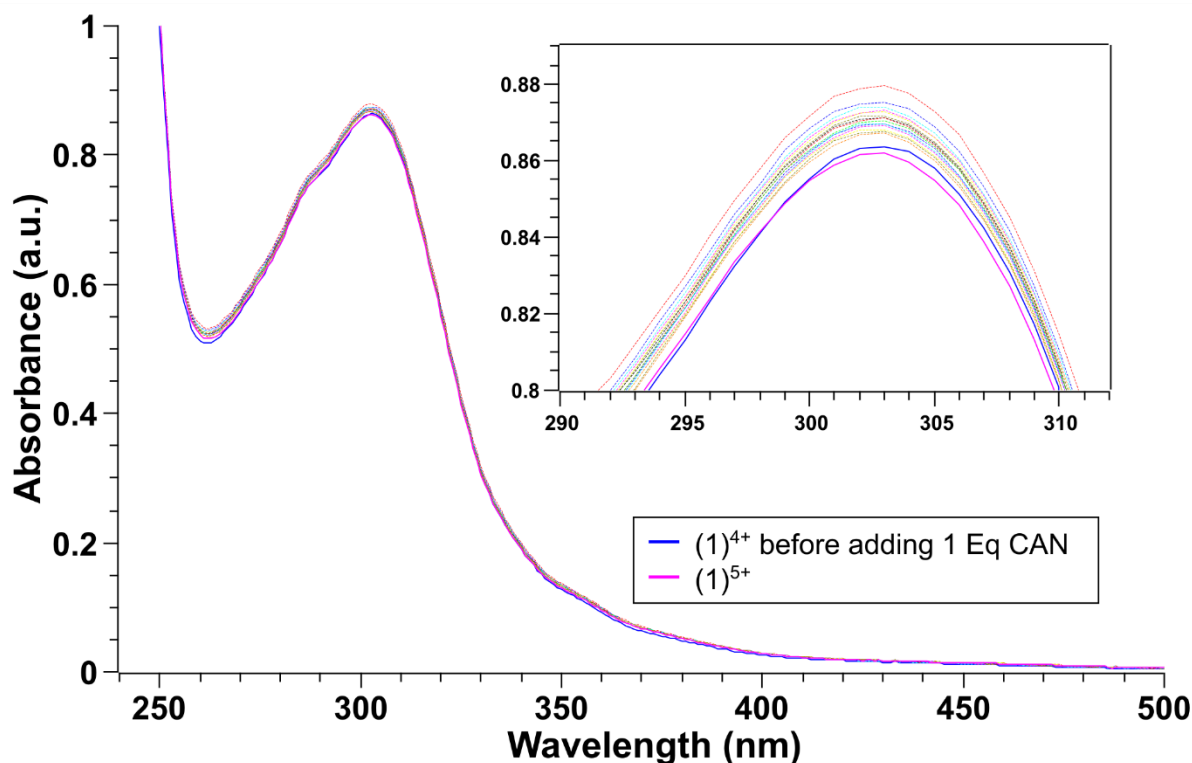


**Figure 35.** Absorbance changes after reaction between  $(1)^{4+}$  (blue) and 1 Eq of CAN. One isosbestic point is shown at 298 nm (inset).

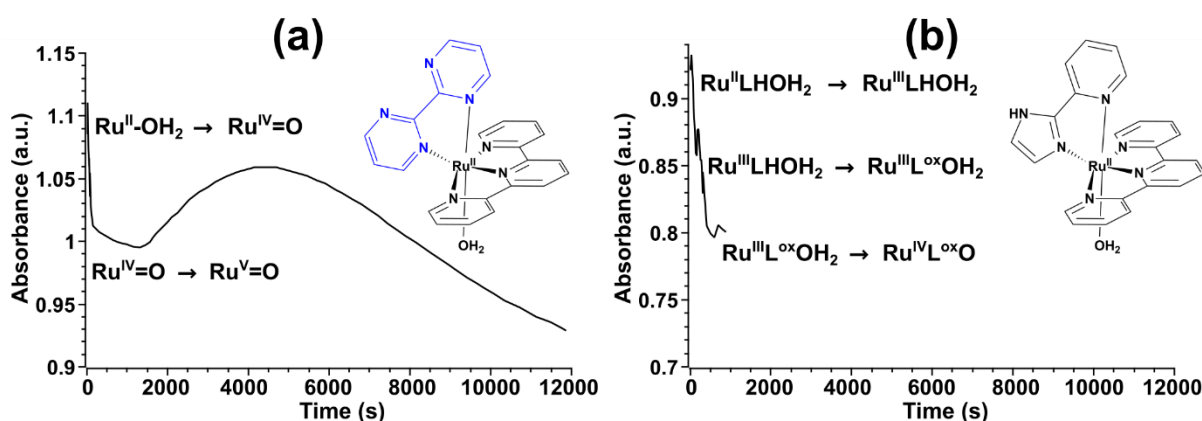


**Figure 36.** Absorbance changes along time after successive reaction of (a)  $[\text{Ru}^{\text{II}}(\text{bpm})(\text{tpy})(\text{OH}_2)]^{2+}$  and (b) **(1)** with 3 equivalents of CAN, monitored at 283 and 293 nm, respectively. Figure (a) was adapted from Concepcion *et al.*<sup>84</sup>

The chemical water oxidation with CAN was also carried out using **(2)** and **(3)** complexes to evaluate their UV-visible spectral changes. After oxidation with 1 equivalent of CAN, like **(1)**, complex **(3)** suffered a continuous decreasing of absorbance in the 280 – 320 nm region, but there was not a complete depletion in the MLCT absorption band as observed in **Figure 37**. This could lead to think about a slow

reaction to reach  $(\mathbf{3})^{3+}$ , but despite leaving the solution a longer time to observe some changes, none modification in the spectra was displayed. Another important event was also observed in the spectra along the reaction. In contrast to  $(\mathbf{1})$ , where the oxidation with CAN afforded immediately continuous spectral changes, the black spectrum of  $(\mathbf{3})^{2+}$  remained the same and only after 5 minutes turned into the red spectrum (**Figure 37**), and then no changes were observed. This small remaining MLCT band could probably be associated to a mixture of  $\text{Ru}^{\text{II}}$  and  $\text{Ru}^{\text{IV}}$  species, as a result of a more stable  $\text{Ru}^{\text{IV}}$  over the  $\text{Ru}^{\text{III}}$  species in complexes containing a pyrimidine moiety in the structure, as reported in other works,<sup>72,86</sup> where back donation to a great pi acceptor ligand (pyridimine moiety in this Thesis) and electron donation from a better electron donor (imidazole in this Thesis) favored the  $\text{Ru}^{\text{II}}$  and  $\text{Ru}^{\text{IV}}$  species, respectively, over the  $\text{Ru}^{\text{III}}$  species. Following oxidation steps were quite similar to complex  $(\mathbf{1})$ , with total bleach of MLCT band and minor changes to reach the  $(\mathbf{3})^{5+}$  species ( $[\text{Ru}^{\text{IV}}\text{L}^{\text{ox}}\text{O}]$  according to Pourbaix diagram in **Figure 31**).

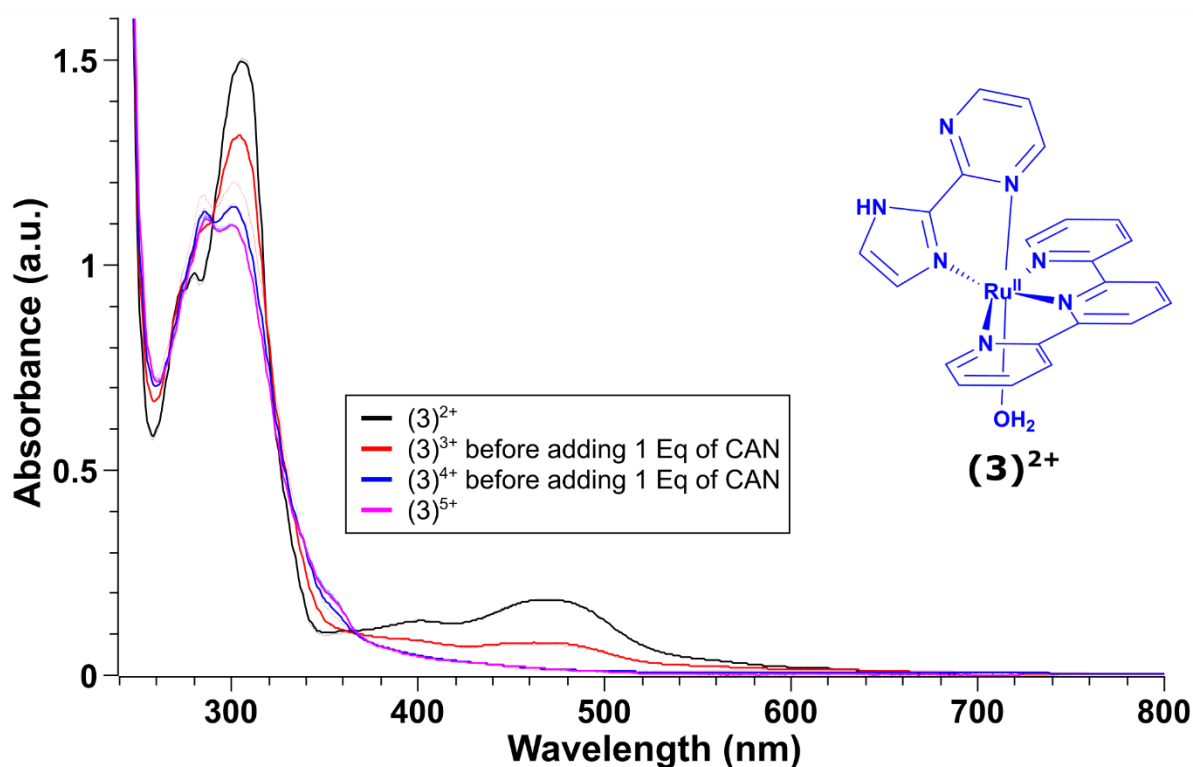


**Figure 37.** UV-visible spectral changes (30 s intervals) upon addition of 1, 2, and 3 equivalents of  $\text{Ce}^{\text{IV}}$  to  $[\text{Ru}^{\text{II}}(\text{Himpm})(\text{tpy})(\text{OH}_2)]^{2+}$  (15  $\mu\text{M}$ ).

In order to investigate the pathway that water oxidation is carried out by the aqua complexes presented in this Thesis, a reaction between **(3)** at various concentrations and excess of  $\text{Ce}^{\text{IV}}$  (30 equivalents, to assure a continuous water oxidation over time) was performed during 1800 s to identify the order of reaction related to complex. To achieve this goal, the absorbance changes at 360 nm ( $\text{Ce}^{\text{IV}}$  consumption) were recorded and displayed in **Figure 38**. This graphic displays a linear dependency between absorbance and time, affording the initial rate constants ( $k_{\text{obs}}$ ) extracted from equation  $(\text{Abs}/\epsilon b) = (K_{\text{obs}})t + \text{constant}$ , where  $\epsilon$  is molar absorptivity and  $b$  is the cuvette path length. (Concepcion, 2010) The initial rate constants ( $k_{\text{obs}}$ ) obtained from the linear fits were plotted against the concentrations of complex. Two graphics (**Figure 39** and **Figure 40**) were plotted because the initial proposal of a linear correlation between  $k_{\text{obs}}$  and  $[(3)]$  was not suitable.

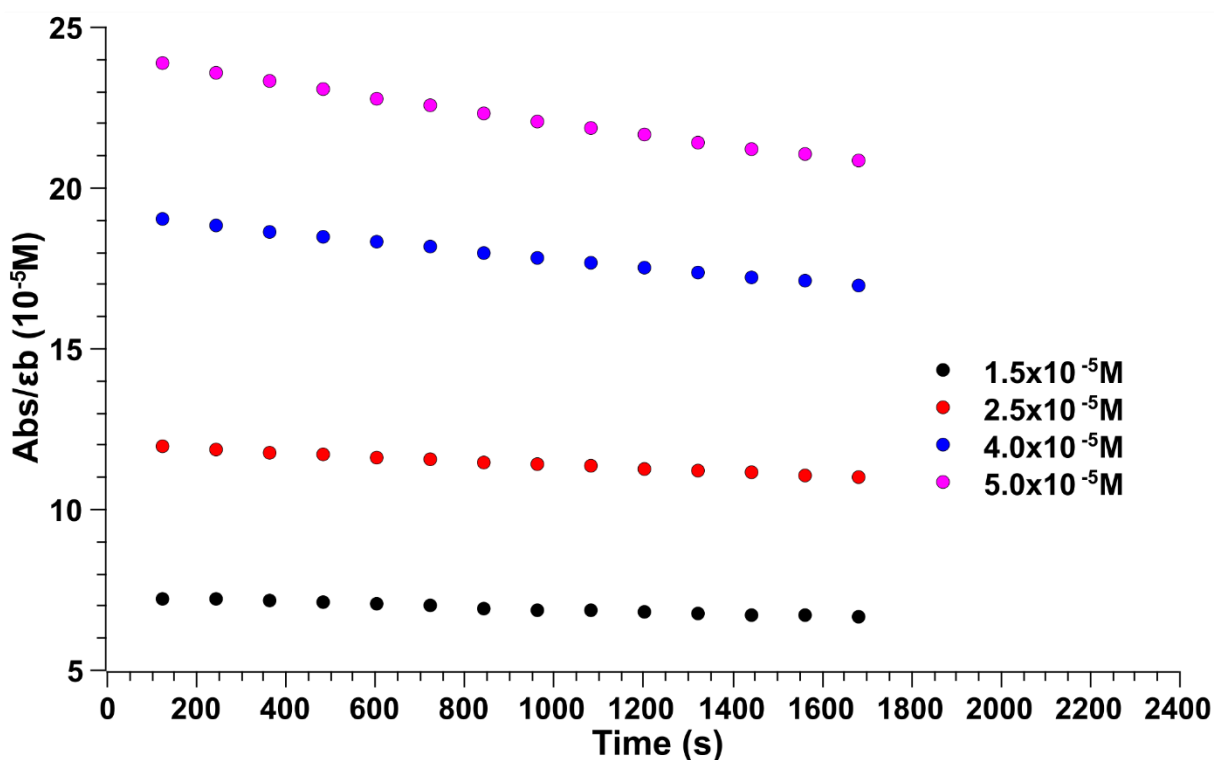


**Figure 38.**  $\text{Ce}^{\text{IV}}$  loss monitored at 360 nm upon addition of 30 equivalents of  $\text{Ce}^{\text{IV}}$  to  $[\text{Ru}^{\text{II}}(\text{Himp})_2(\text{tpy})(\text{OH}_2)_2]^{2+}$  ( $15 \mu\text{M}$ ). No data was collected during the first 10 s due to the time required for mixing complex and CAN. Each measurement was taken after 120 s.

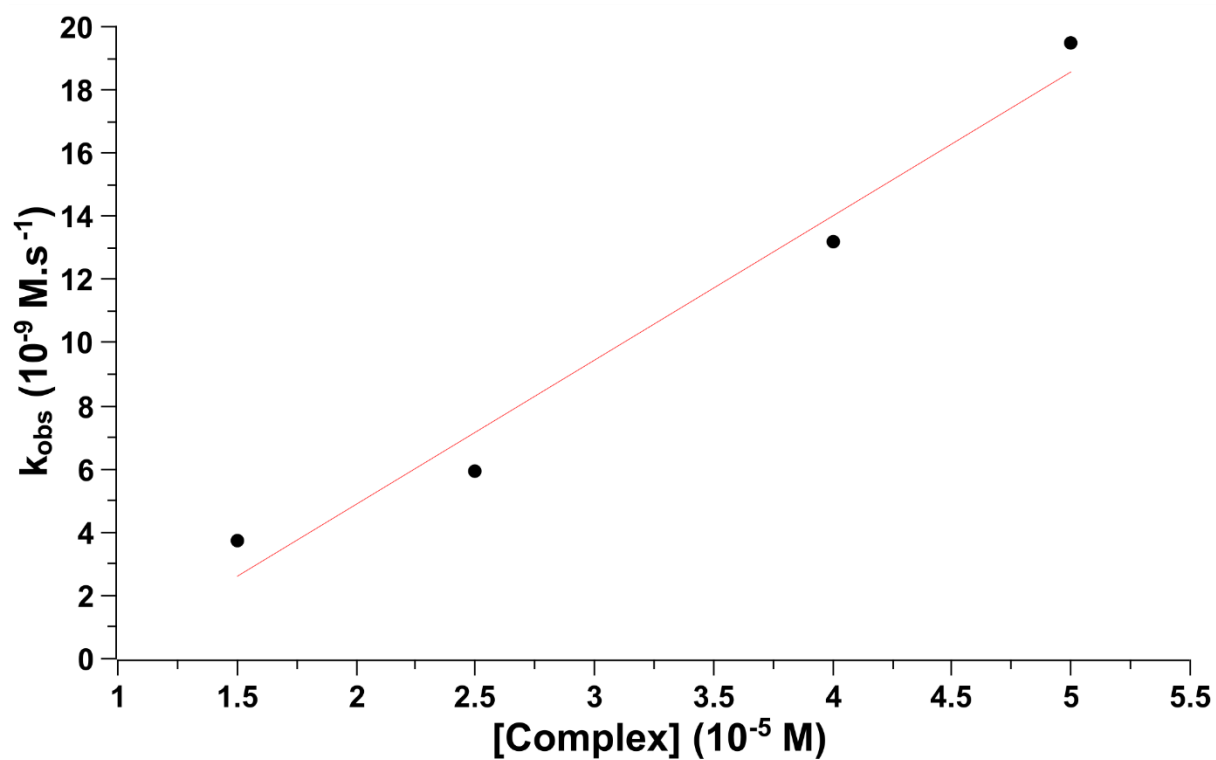


**Figure 39.** Plot of  $k_{obs}$  (values determined from plotting  $Abs(360\text{ nm})/\epsilon b$  versus time) versus concentration of complex  $[Ru^{II}(Himp)(tpy)(OH_2)]^{2+}$ . It is shown that the graphic could be better represented by a parabolic function, i.e., a second order kinetic reaction.

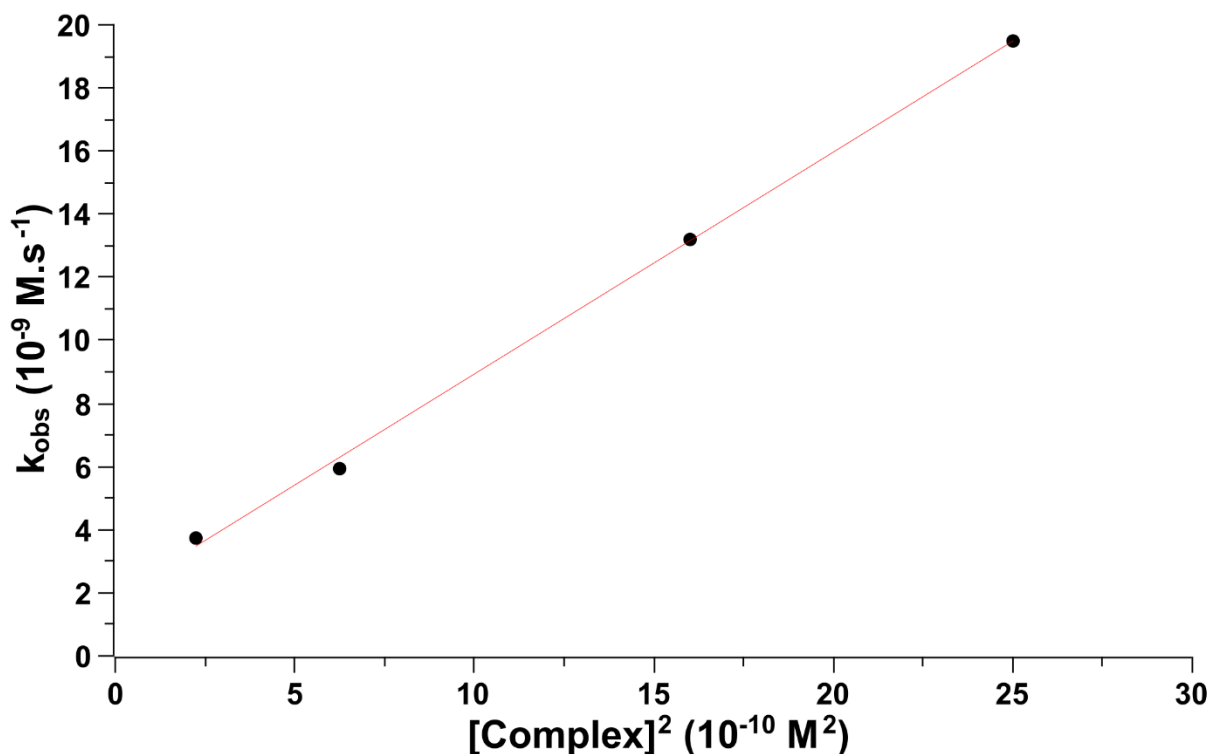


**Figure 40.** Plot of  $k_{\text{obs}}$  versus  $[\text{complex}]^2$ . The reaction is second order with respect to  $[\text{Ru}^{\text{II}}(\text{Himpm})(\text{tpy})(\text{OH}_2)]^{2+}$ .

According to these preliminary results, under excess of  $\text{Ce}^{\text{IV}}$  conditions, the water oxidation reaction by  $[\text{Ru}^{\text{II}}(\text{Himpm})(\text{tpy})(\text{OH}_2)]^{2+}$  is second order with respect to the catalyst, indicating that the mechanism involves a radical coupling reaction, a pathway which is different from the  $[\text{Ru}^{\text{II}}(\text{bpm})(\text{tpy})(\text{OH}_2)]^{2+}$  complex that catalyzes the water oxidation reaction by a nucleophilic attack from water to the catalyst.<sup>72</sup>

All of the aqua complexes follow the same Pourbaix diagrams and  $\text{Ce}^{\text{IV}}$ -mediated UV-visible changes pattern, which could lead us to think that the mechanism followed by the complexes in this Thesis could probably catalyze the water oxidation reaction by a similar radical coupling step. The main difference among the complexes seems to involve the energy necessary to reach the higher oxidation states to carry out the water oxidation, which is related to the electron-donor capacity of the Himp $x$  ligands. The greater the donor capacity, the lower the oxidation potential.

## 5. CONCLUSIONS

The synthesis of the complexes was successfully achieved and well characterized. Conductivity measurements showed a 1:1 and 2:1 composition for chlorido and aqua complexes, respectively.  $^1\text{H-NMR}$  spectroscopy showed the complete isolation of the chlorido isomers and, along with UV-visible spectroscopy and mass spectrometry, confirmed the substitution of chlorido by aqua ligand. X-ray crystallography allowed to prove the proposed structures for chlorido and aqua isomers. The electron donor–acceptor properties of the Himp $x$  ligands (Himpa, Himp $m$ , Himp $y$ , and Himp $z$ ) were studied in aqueous and organic media by electrochemical techniques showing irreversible redox processes. Cyclic voltammetry measurements for  $[\text{Ru}^{\text{II}}(\text{Himp}_x)(\text{tpy})(\text{OH}_2)](\text{PF}_6)_2$  complexes exhibited the influence of donor–acceptor properties of the Himp $x$  ligands in the electronic properties of those complexes. Pourbaix diagrams were obtained through electrochemical measurements of the aqua complexes in a broad pH range to assess the influence of the donor–acceptor properties of the Himp $x$  ligands on the mechanism of water oxidation reaction. All these results led to conclude that the ionizable N–H imidazole proton plays an important role in tuning the redox potential of the ruthenium complexes so that a ligand with a more acidic proton can increase the catalytic performance of water oxidation. The presence of heteroaryl moiety in the complexes showed how subtle modifications in its structure could lead to different pathways of reaction toward the catalysis of water oxidation compared to other reported catalysts.

## 6. PERSPECTIVES

Future work will concentrate on conclude the investigation of water oxidation performance of Ru(II) aqua complexes through kinetic studies by using CAN (cerium ammonium nitrate) and how the modification in the position of two nitrogen atoms in the ligand structure would influence on the catalytic mechanism and performance of water oxidation catalysis.

## 7. REFERENCES

- (1) Huamaní, L. E. S. C.; Tenorio, J. C.; Barrach Guerra, R.; Hideki Nakahata, D.; Bibi, N.; Bonacin, J. A.; Formiga, A. L. B. Role of Protonation and Isomerism in the Supramolecular Architectures of Heteroaryl-2-imidazole Compounds: Crystal Packing Patterns and Energetics. *Crystal Growth & Design* **2020**, *20*, 5143–5159.
- (2) Loganathan, R.; Ramakrishnan, S.; Suresh, E.; Riyasdeen, A.; Akbarsha, M. A.; Palaniandavar, M. Mixed Ligand Copper(II) Complexes of N,N-Bis(benzimidazol-2-ylmethyl)amine (BBA) with Diimine Co-Ligands: Efficient Chemical Nuclease and Protease Activities and Cytotoxicity. *Inorg. Chem.* **2012**, *51*, 5512–5532.
- (3) Vitaku, E.; Smith, D. T.; Njardarson, J. T. Analysis of the Structural Diversity, Substitution Patterns, and Frequency of Nitrogen Heterocycles among U.S. FDA Approved Pharmaceuticals. *J. Med. Chem.* **2014**, *57*, 10257–10274.
- (4) Rudd, J. A.; Brennaman, M. K.; Michaux, K. E.; Ashford, D. L.; Murray, R. W.; Meyer, Thomas. J. Synthesis, Electrochemistry, and Excited-State Properties of Three Ru(II) Quaterpyridine Complexes. *J. Phys. Chem. A* **2016**, *120*, 1845–1852.
- (5) Zhang, F.-M.; Dong, L.-Z.; Qin, J.-S.; Guan, W.; Liu, J.; Li, S.-L.; Lu, M.; Lan, Y.-Q.; Su, Z.-M.; Zhou, H.-C. Effect of Imidazole Arrangements on Proton-Conductivity in Metal–Organic Frameworks. *J. Am. Chem. Soc.* **2017**, *139*, 6183–6189.
- (6) Ratier de Arruda, E. G.; de Farias, M. A.; Venturinelli Jannuzzi, S. A.; de Almeida Gonsales, S.; Timm, R. A.; Sharma, S.; Zoppellaro, G.; Kubota, L. T.; Knobel, M.; Barboza Formiga, A. L. Synthesis, structural and magnetic characterization of a copper(II) complex of 2,6-di(1H-imidazol-2-yl)pyridine and its application in copper-mediated polymerization catalysis. *Inorg. Chim. Acta* **2017**, *466*, 456–463.
- (7) Hashizume, D.; Iegaki, M.; Yasui, M.; Iwasaki, F.; Meng, J.; Wen, Z.; Matsuura, T. Two-component molecular crystals from N-heteroaromatics and nitrobenzoic acids. *Acta Cryst.* **2001**, *C57*, 1067–1072.
- (8) B. Aakeröy, C.; Schultheiss, N.; Desper, J.; Moore, C. Balancing Hydrogen-Bond Donors and Acceptors in a Family of Bifunctional Aromatic N-Heterocycles. *Cryst. Growth Des.* **2007**, *7*, 2324–2331.
- (9) Lemmerer, A.; Adsmund, D. A.; Bernstein, J. An Investigation of the Hydrogen-Bond Preferences and Co-crystallization Behavior of Three Didonor Compounds. *Cryst. Growth Des.* **2011**, *11*, 2011–2019.
- (10) Rajewski, K. W.; Andrzejewski, M.; Katrusiak, A. Competition between Halogen and Hydrogen Bonds in Triiodoimidazole Polymorphs. *Cryst. Growth Des.* **2016**, *16*, 3869–3874.
- (11) Oswald, I. D. H.; Motherwell, W. D. S.; Parsons, S. Formation of quinol co-crystals with hydrogen-bond acceptors. *Acta Cryst.* **2005**, *B61*, 46–57.
- (12) Podsiadło, M.; Jakóbek, K.; Katrusiak, A. Density, freezing and molecular aggregation in pyridazine, pyridine and benzene. *CrystEngComm* **2010**, *12*, 2561–2567.
- (13) Serpell, C. J.; Beer, P. D. Intermolecular Interactions in Bromo-, Methyl-, and Cyanoimidazole Derivatives. *Cryst. Growth Des.* **2013**, *13*, 2866–2871.

- (14) Goswami, P. K.; Thaimattam, R.; Ramanan, A. Crystal Engineering of Multicomponent Crystal Forms of p-Aminosalicylic Acid with Pyridine Based Cofomers. *Cryst. Growth Des.* **2016**, *16*, 1268–1281.
- (15) Bibi, N.; de Arruda, E. G. R.; Domingo, A.; Oliveira, A. A.; Galuppo, C.; Phung, Q. M.; Orra, N. M.; Béron, F.; Paesano, A.; Pierloot, K.; et al. Switching the Spin-Crossover Phenomenon by Ligand Design on Imidazole–Diazineiron(II) Complexes. *Inorg. Chem.* **2018**, *57*, 14603–14616.
- (16) Zanvettor, N. T.; Nakahata, D. H.; de Paiva, R. E. F.; Ribeiro, M. A.; Cuin, A.; Corbi, P. P.; Formiga, A. L. B. Copper(II), palladium(II) and platinum(II) complexes with 2,2-thiophen-yl-imidazole: Synthesis, spectroscopic characterization, X-ray crystallographic studies and interactions with calf-thymus DNA. *Inorg. Chim. Acta* **2016**, *443*, 304–315.
- (17) Nakahata, D. H.; Ribeiro, M. A.; Corbi, P. P.; Machado, D.; Lancellotti, M.; Lustri, W. R.; da Costa Ferreira, A. M.; Formiga, A. L. B. Synthesis, characterization and preliminary antimicrobial assays of copper(II) complexes with 2-(imidazole-2-yl)heteroaryl ligands. *Inorg. Chim. Acta* **2017**, *458*, 224–232.
- (18) Bibi, N.; Guerra, R. B.; Huamaní, L. E. S. C.; Formiga, A. L. B. Crystal structure, electrochemical and spectroscopic investigation of *mer*-tris[2-(1*H*-imidazol-2-yl-κ<sup>N</sup>)pyrimidine-κ<sup>N</sup><sup>1</sup>]ruthenium(II) bis(hexafluoridophosphate) trihydrate. *Acta Cryst.* **2018**, *E74*, 874–877.
- (19) Ishida, H.; Kashino, S. Pyridinium and 1,2-diazinium salts of chloranilic acid. *Acta Cryst.* **1999**, *C55*, 1149–1152.
- (20) Ishida, H.; Kashino, S. 1:2 Complexes of chloranilic acid with pyrimidine and pyrazine. *Acta Cryst.* **1999**, *C55*, 1714–1717.
- (21) Jin, S.; Zhang, H.; Liu, H.; Wen, X.; Li, M.; Wang, D. Structure of eight molecular salts assembled from noncovalent bonding between carboxylic acids, imidazole, and benzimidazole. *J. Mol. Struct.* **2015**, *1096*, 157–170.
- (22) Andrzejewski, M.; Marciniak, J.; Rajewski, K. W.; Katrusiak, A. Halogen and Hydrogen Bond Architectures in Switchable Chains of Di- and Trihaloimidazoles. *Cryst. Growth Des.* **2015**, *15*, 1658–1665.
- (23) Shao, X.-D.; Shi, C.; Yu, C.-H.; Zhang, W. Helical structures in a lithium hexacyanocobaltate-based three-dimensional metal–cyanide framework. *Inorg. Chem. Commun.* **2014**, *47*, 1–4.
- (24) MacDonald, J. C.; Dorrestein, P. C.; Pilley, M. M. Design of Supramolecular Layers via Self-Assembly of Imidazole and Carboxylic Acids. *Cryst. Growth Des.* **2001**, *1*, 29–38.
- (25) Piecha, A.; Białońska, A.; Jakubas, R. Novel organic–inorganic hybrid ferroelectric: bis(imidazolium) pentachloroantimonate(III), (C<sub>3</sub>N<sub>2</sub>H<sub>5</sub>)<sub>2</sub>SbCl<sub>5</sub>. *J. Mater. Chem.* **2012**, *22*, 333–336.
- (26) Węclawik, M.; Gałgor, A.; Piecha, A.; Jakubas, R.; Medycki, W. Synthesis, crystal structure and phase transitions of a series of imidazolium iodides. *CrystEngComm* **2013**, *15*, 5633–5640.
- (27) Guerra, R. B.; Huamaní, L. S. C.; Tenorio, J. C.; Guimarães, W. M.; Bonacin, J. A.; Barboza Formiga, A. L. Analysis of solvent-accessible voids and proton-coupled electron transfer of 2,6-bis(1*H*-imidazol-2-yl)pyridine and its hydrochloride. *Acta Cryst.* **2019**, *C75*, 1359–1371.
- (28) Aakeröy, C. B.; Wijethunga, T. K.; Haj, M. A.; Desper, J.; Moore, C. The structural landscape of heteroaryl-2-imidazoles: competing halogen- and hydrogen-bond interactions. *CrystEngComm* **2014**, *16*, 7218–7225.

- (29) Voss, M. E.; Beer, C. M.; Mitchell, S. A.; Blomgren, P. A.; Zhichkin, P. E. A simple and convenient one-pot method for the preparation of heteroaryl-2-imidazoles from nitriles. *Tetrahedron* **2008**, *64*, 645–651.
- (30) Bruker. *SAINT*; Bruker AXS Inc.: Madison, Wisconsin, USA, 2010.
- (31) Bruker. *SADABS*; Bruker AXS Inc.: Madison, Wisconsin, USA, 2010.
- (32) Sheldrick, G. M. SHELXT - Integrated space-group and crystal-structure determination. *Acta Cryst.* **2015**, *A71*, 3–8.
- (33) Sheldrick, G. M. A short history of SHELX. *Acta Cryst.* **2008**, *A64*, 112–122.
- (34) Dolomanov, O. V.; Bourhis, L. J.; Gildea, R. J.; Howard, J. A. K.; Puschmann, H. It OLEX2: a complete structure solution, refinement and analysis program. *J. Appl. Cryst.* **2009**, *42*, 339–341.
- (35) Farrugia, L. J. ORTEP-3 for Windows - a version of ORTEP-III with a Graphical User Interface (GUI). *J. Appl. Cryst.* **1997**, *30*, 565.
- (36) Macrae, C. F.; Bruno, I. J.; Chisholm, J. A.; Edgington, P. R.; McCabe, P.; Pidcock, E.; Rodriguez-Monge, L.; Taylor, R.; van de Streek, J.; Wood, P. A. Mercury CSD 2.0 – new features for the visualization and investigation of crystal structures. *J. Appl. Cryst.* **2008**, *41*, 466–470.
- (37) Allen, F. H. The Cambridge Structural Database: a quarter of a million crystal structures and rising. *Acta Cryst.* **2002**, *B58*, 380–388.
- (38) Bruno, I. J.; Cole, J. C.; Edgington, P. R.; Kessler, M.; Macrae, C. F.; McCabe, P.; Pearson, J.; Taylor, R. New software for searching the Cambridge Structural Database and visualizing crystal structures. *Acta Cryst.* **2002**, *B58*, 389–397.
- (39) Etter, M. C. Encoding and decoding hydrogen-bond patterns of organic compounds. *Acc. Chem. Res.* **1990**, *23*, 120–126.
- (40) Zięba, S.; Dubis, A. T.; Gzella, A. K.; Ławniczak, P.; Pogorzelec-Glaser, K.; Łapiński, A. Toward a new type of proton conductor based on imidazole and aromatic acids. *Phys. Chem. Chem. Phys.* **2019**, *21*, 17152–17162.
- (41) McSkimming, A.; Bhadbhade, M.; Colbran, S. B. Hydride ion-carrier ability in Rh(I) complexes of a nicotinamide-functionalised N-heterocyclic carbene ligand. *Dalton Trans.* **2010**, *39*, 10581–10584.
- (42) Ashford, D. L.; Glasson, C. R. K.; Norris, M. R.; Concepcion, J. J.; Keinan, S.; Brennaman, M. K.; Templeton, J. L.; Meyer, T. J. Controlling Ground and Excited State Properties through Ligand Changes in Ruthenium Polypyridyl Complexes. *Inorg. Chem.* **2014**, *53*, 5637–5646.
- (43) Tseng, H.-W.; Zong, R.; Muckerman, J. T.; Thummel, R. Mononuclear Ruthenium(II) Complexes That Catalyze Water Oxidation. *Inorg. Chem.* **2008**, *47*, 11763–11773.
- (44) Masaoka, S.; Sakai, K. Clear Evidence Showing the Robustness of a Highly Active Oxygen-evolving Mononuclear Ruthenium Complex with an Aqua Ligand. *Chem. Lett.* **2009**, *38*, 182–183.
- (45) Zhong, D. K.; Zhao, S.; Polyansky, D. E.; Fujita, E. Diminished photoisomerization of active ruthenium water oxidation catalyst by anchoring to metal oxide electrodes. *Journal of Catalysis* **2013**, *307*, 140–147.
- (46) Naskar, S.; Pakhira, B.; Mishra, D.; Mitra, P.; Chattopadhyay, S. K.; Naskar, S. Synthesis, characterization and theoretical studies of the heteroleptic Ruthenium(II) complexes of 2,6-bis(benzimidazolyl)pyridine. *Polyhedron* **2015**, *100*, 170–179.
- (47) Sullivan, B. P.; Calvert, J. M.; Meyer, T. J. Cis-Trans Isomerism in (trpy)(PPh<sub>3</sub>)RuCl<sub>2</sub>. Comparisons between the Chemical and Physical Properties of a Cis-Trans Isomeric Pair. *Inorg. Chem.* **1980**, *19*, 1404–1407.

- (48) Geary, W. J. The use of conductivity measurements in organic solvents for the characterisation of coordination compounds. *Coord. Chem. Rev.* **1971**, *7*, 81–122.
- (49) Rusina, A.; Vlček, A. A. Formation of Rh(I)-Carbonyl Complex by the Reaction with Some Non-alcoholic, Oxygen-containing Solvents. *Nature* **1965**, *206*, 295–296.
- (50) Serp, P.; Hernandez, M.; Richard, B.; Kalck, P. A Facile Route to Carbonylhalogenometal Complexes (M = Rh, Ir, Ru, Pt) by Dimethylformamide Decarbonylation. *European Journal of Inorganic Chemistry* **2001**, *2001*, 2327–2336.
- (51) Constable, E. C.; Hannon, M. J. Solvent effects in the reactions of 6-phenyl-2,2'-bipyridine with ruthenium(II). *Inorganica Chimica Acta* **1993**, *211*, 101–110.
- (52) Cheung, K.-C.; Guo, P.; So, M.-H.; Zhou, Z.-Y.; Lee, L. Y. S.; Wong, K.-Y. Ruthenium Terpyridine Complexes Containing a Pyrrole-Tagged 2,2'-Dipyridylamine Ligand—Synthesis, Crystal Structure, and Electrochemistry. *Inorg. Chem.* **2012**, *51*, 6468–6475.
- (53) Okamura, M.; Yoshida, M.; Kuga, R.; Sakai, K.; Kondo, M.; Masaoka, S. A mononuclear ruthenium complex showing multiple proton-coupled electron transfer toward multi-electron transfer reactions. *Dalton Trans.* **2012**, *41*, 13081.
- (54) Jakubikova, E.; Chen, W.; Dattelbaum, D. M.; Rein, F. N.; Rocha, R. C.; Martin, R. L.; Batista, E. R. Electronic Structure and Spectroscopy of  $[\text{Ru}(\text{tpy})_2]^{2+}$ ,  $[\text{Ru}(\text{tpy})(\text{bpy})(\text{H}_2\text{O})]^{2+}$ , and  $[\text{Ru}(\text{tpy})(\text{bpy})(\text{Cl})]^+$ . *Inorg. Chem.* **2009**, *48*, 10720–10725.
- (55) Boggess, R. K.; Martin, R. Bruce. Metal ion induced pyrrole ionization in 2-(2'-pyridyl)imidazole. *Inorg. Chem.* **1974**, *13*, 1525–1527.
- (56) Haga, M.-A. Synthesis and protonation-deprotonation reactions of ruthenium(II) complexes containing 2, 2'-bibenzimidazole and related ligands. *Inorg. Chim. Acta* **1983**, *75*, 29–35.
- (57) Jones, H.; Newell, M.; Metcalfe, C.; Spey, S. E.; Adams, H.; Thomas, J. A. Deprotonation of a ruthenium (II) complex incorporating a bipyrazole ligand leading to optical and electrochemical switching. *Inorg. Chem. Commun.* **2001**, *4*, 475–477.
- (58) Meyer, T. J.; Huynh, M. H. V. The Remarkable Reactivity of High Oxidation State Ruthenium and Osmium Polypyridyl Complexes. *Inorg. Chem.* **2003**, *42*, 8140–8160.
- (59) Blakemore, J. D.; Crabtree, R. H.; Brudvig, G. W. Molecular Catalysts for Water Oxidation. *Chem. Rev.* **2015**, *115*, 12974–13005.
- (60) McEvoy, J. P.; Brudvig, G. W. Water-Splitting Chemistry of Photosystem II. *Chem. Rev.* **2006**, *106*, 4455–4483.
- (61) Fujishima, A.; Honda, K. Electrochemical Photolysis of Water at a Semiconductor Electrode. *Nature* **1972**, *238*, 37–38.
- (62) Llobet, A. Synthesis, spectral and redox properties of a new series of aqua complexes of ruthenium(II). *Inorg. Chim. Acta* **1994**, *221*, 125–131.
- (63) Kalyanasundaram, K.; Nazeeruddin, M. K. Photophysics and photoredox reactions of ligand-bridged binuclear polypyridyl complexes of ruthenium(II) and of their monomeric analogs. *Inorg. Chem.* **1990**, *29*, 1888–1897.
- (64) Rillema, D. P.; Sahai, R.; Matthews, P.; Edwards, A. K.; Shaver, R. J.; Morgan, L. Multimetallic ruthenium(II) complexes based on biimidazole and bibenzimidazole: effect of dianionic bridging ligands on redox and spectral properties. *Inorg. Chem.* **1990**, *29*, 167–175.

- (65) Huynh, M. H. V.; Dattelbaum, D. M.; Meyer, T. J. Excited state electron and energy transfer in molecular assemblies. *Coord. Chem. Rev.* **2005**, *249*, 457–483.
- (66) Young, R. C.; Meyer, T. J.; Whitten, D. G. Kinetic relaxation measurement of rapid electron transfer reactions by flash photolysis. Conversion of light energy into chemical energy using the tris(2,2'-bipyridine)ruthenium(3+)-tris(2,2'-bipyridine)ruthenium(2+\*) couple. *J. Am. Chem. Soc.* **1975**, *97*, 4781–4782.
- (67) David W. Thompson; Akitaka Ito; Thomas J. Meyer. [Ru(bpy)<sub>3</sub>]<sup>2+\*</sup> and other remarkable metal-to-ligand charge transfer (MLCT) excited states. *Pure Appl. Chem.* **2013**, *85*, 1257–1305.
- (68) Gersten, S. W.; Samuels, G. J.; Meyer, T. J. Catalytic oxidation of water by an oxo-bridged ruthenium dimer. *J. Am. Chem. Soc.* **1982**, *104*, 4029–4030.
- (69) Zong, R.; Thummel, R. P. A New Family of Ru Complexes for Water Oxidation. *J. Am. Chem. Soc.* **2005**, *127*, 12802–12803.
- (70) Sens, C.; Romero, I.; Rodríguez, M.; Llobet, A.; Parella, T.; Benet-Buchholz, J. A New Ru Complex Capable of Catalytically Oxidizing Water to Molecular Dioxygen. *J. Am. Chem. Soc.* **2004**, *126*, 7798–7799.
- (71) Xu, Y.; Åkermark, T.; Gyollai, V.; Zou, D.; Eriksson, L.; Duan, L.; Zhang, R.; Åkermark, B.; Sun, L. A New Dinuclear Ruthenium Complex as an Efficient Water Oxidation Catalyst. *Inorg. Chem.* **2009**, *48*, 2717–2719.
- (72) Concepcion, J. J.; Jurss, J. W.; Templeton, J. L.; Meyer, T. J. One Site is Enough. Catalytic Water Oxidation by [Ru(tpy)(bpm)(OH<sub>2</sub>)]<sup>2+</sup> and [Ru(tpy)(bpz)(OH<sub>2</sub>)]<sup>2+</sup>. *J. Am. Chem. Soc.* **2008**, *130*, 16462–16463.
- (73) Maity, D.; Bhaumik, C.; Mondal, D.; Baitalik, S. Ru(II) and Os(II) Complexes Based on Terpyridyl-Imidazole Ligand Rigidly Linked to Pyrene: Synthesis, Structure, Photophysics, Electrochemistry, and Anion-Sensing Studies. *Inorg. Chem.* **2013**, *52*, 13941–13955.
- (74) Bhaumik, C.; Das, S.; Saha, D.; Dutta, S.; Baitalik, S. Synthesis, Characterization, Photophysical, and Anion-Binding Studies of Luminescent Heteroleptic Bis-Tridentate Ruthenium(II) Complexes Based on 2,6-Bis(Benzimidazole-2-yl)Pyridine and 4'-Substituted 2,2':6',2'' Terpyridine Derivatives. *Inorg. Chem.* **2010**, *49*, 5049–5062.
- (75) Maity, D.; Bhaumik, C.; Karmakar, S.; Baitalik, S. Photoinduced Electron and Energy Transfer and pH-Induced Modulation of the Photophysical Properties in Homo- and Heterobimetallic Complexes of Ruthenium(II) and Rhodium(III) Based on a Heteroditopic Phenanthroline–Terpyridine Bridge. *Inorg. Chem.* **2013**, *52*, 7933–7946.
- (76) Maity, D.; Das, S.; Mardanya, S.; Baitalik, S. Synthesis, Structural Characterization, and Photophysical, Spectroelectrochemical, and Anion-Sensing Studies of Heteroleptic Ruthenium(II) Complexes Derived from 4'-Polyaromatic-Substituted Terpyridine Derivatives and 2,6-Bis(benzimidazol-2-yl)pyridine. *Inorg. Chem.* **2013**, *52*, 6820–6838.
- (77) Kitamura, N.; Kawanishi, Y.; Tazuke, S. Spectroscopic and electrochemical studies on ruthenium(II) complexes containing diazadiimine ligands. *Chem. Phys. Lett.* **1983**, *97*, 103–106.
- (78) Hage, R.; Prins, R.; Haasnoot, J. G.; Reedijk, J.; Vos, J. G. Synthesis, spectroscopic, and electrochemical properties of bis(2,2'-bipyridyl)-ruthenium compounds of some pyridyl-1,2,4-triazoles. *J. Chem. Soc., Dalton Trans.* **1987**, 1389–1395.

- (79) Rillema, D. P.; Blanton, C. B.; Shaver, R. J.; Jackman, D. C.; Boldaji, M.; Bundy, S.; Worl, L. A.; Meyer, T. J. MLCT- $\pi$  energy gap in pyridyl-pyrimidine and bis(pyridine) complexes of ruthenium(II). *Inorg. Chem.* **1992**, *31*, 1600–1606.
- (80) Gerli, A.; Reedijk, J.; Lakin, M. T.; Spek, A. L. Redox Properties and Electrocatalytic Activity of the Oxo/Aqua System  $[\text{Ru}(\text{terpy})(\text{bpz})(\text{O})]^{2+}/[\text{Ru}(\text{terpy})(\text{bpz})(\text{H}_2\text{O})]^{2+}$ . X-ray Crystal Structure of  $[\text{Ru}(\text{terpy})(\text{bpz})\text{Cl}]\text{PF}_6\cdot\text{MeCN}$  (terpy = 2,2',2''-Terpyridine; bpz = 2,2'-Bipyrazine). *Inorg. Chem.* **1995**, *34*, 1836–1843.
- (81) Fisher, K. J.; Materna, K. L.; Mercado, B. Q.; Crabtree, R. H.; Brudvig, G. W. Electrocatalytic Water Oxidation by a Copper(II) Complex of an Oxidation-Resistant Ligand. *ACS Catal.* **2017**, *7*, 3384–3387.
- (82) Fan, T.; Duan, L.; Huang, P.; Chen, H.; Daniel, Q.; Ahlquist, M. S. G.; Sun, L. The Ru-tpc Water Oxidation Catalyst and Beyond: Water Nucleophilic Attack Pathway versus Radical Coupling Pathway. *ACS Catal.* **2017**, *7*, 2956–2966.
- (83) Takeuchi, K. J.; Thompson, M. S.; Pipes, D. W.; Meyer, T. J. Redox and spectral properties of monooxo polypyridyl complexes of ruthenium and osmium in aqueous media. *Inorg. Chem.* **1984**, *23*, 1845–1851.
- (84) Concepcion, J. J.; Tsai, M.-K.; Muckerman, J. T.; Meyer, T. J. Mechanism of Water Oxidation by Single-Site Ruthenium Complex Catalysts. *J. Am. Chem. Soc.* **2010**, *132*, 1545–1557.
- (85) Wasylenko, D. J.; Ganesamoorthy, C.; Henderson, M. A.; Berlinguette, C. P. Unraveling the Roles of the Acid Medium, Experimental Probes, and Terminal Oxidant,  $(\text{NH}_4)_2[\text{Ce}(\text{NO}_3)_6]$ , in the Study of a Homogeneous Water Oxidation Catalyst. *Inorg. Chem.* **2011**, *50*, 3662–3672.
- (86) Dovletoglou, A.; Adeyemi, S. A.; Meyer, T. J. Coordination and Redox Chemistry of Substituted-Polypyridyl Complexes of Ruthenium. *Inorg. Chem.* **1996**, *35*, 4120–4127.

## 8. APPENDIX

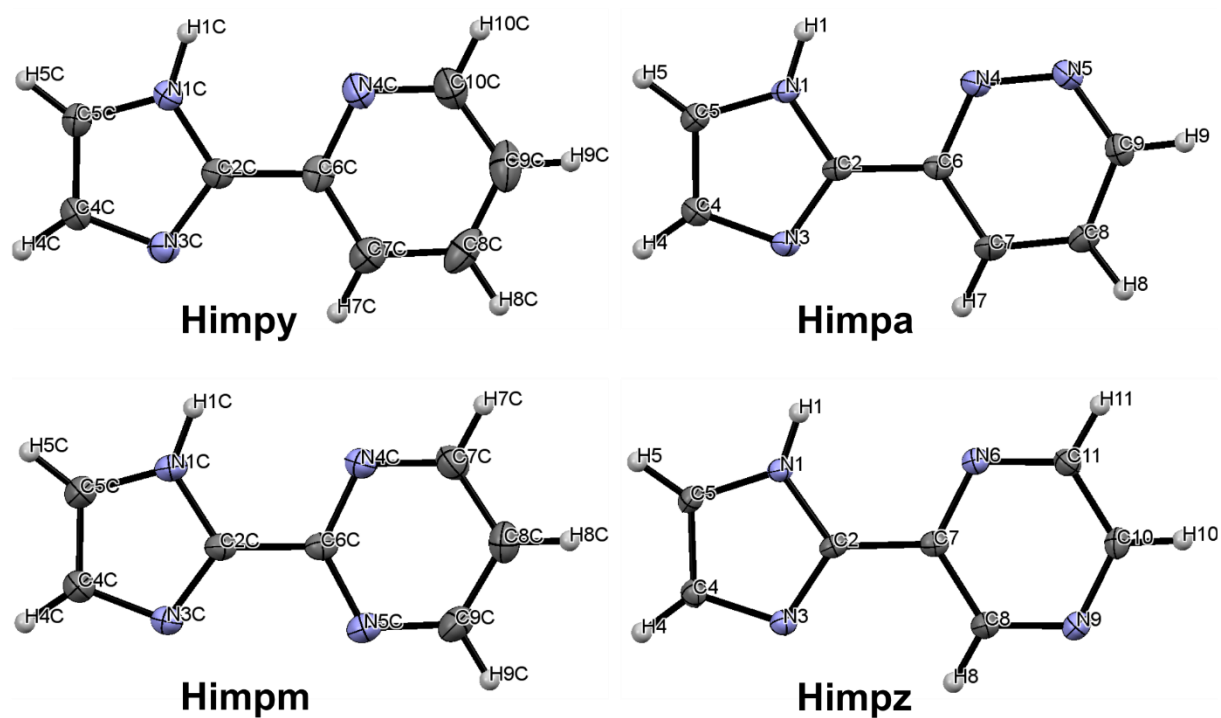


**Figure S1.** ORTEP view of the X-ray structure of Himpx ligands at 150K. Atoms are colored as follows: Carbon (gray), nitrogen (blue), hydrogen (soft gray).

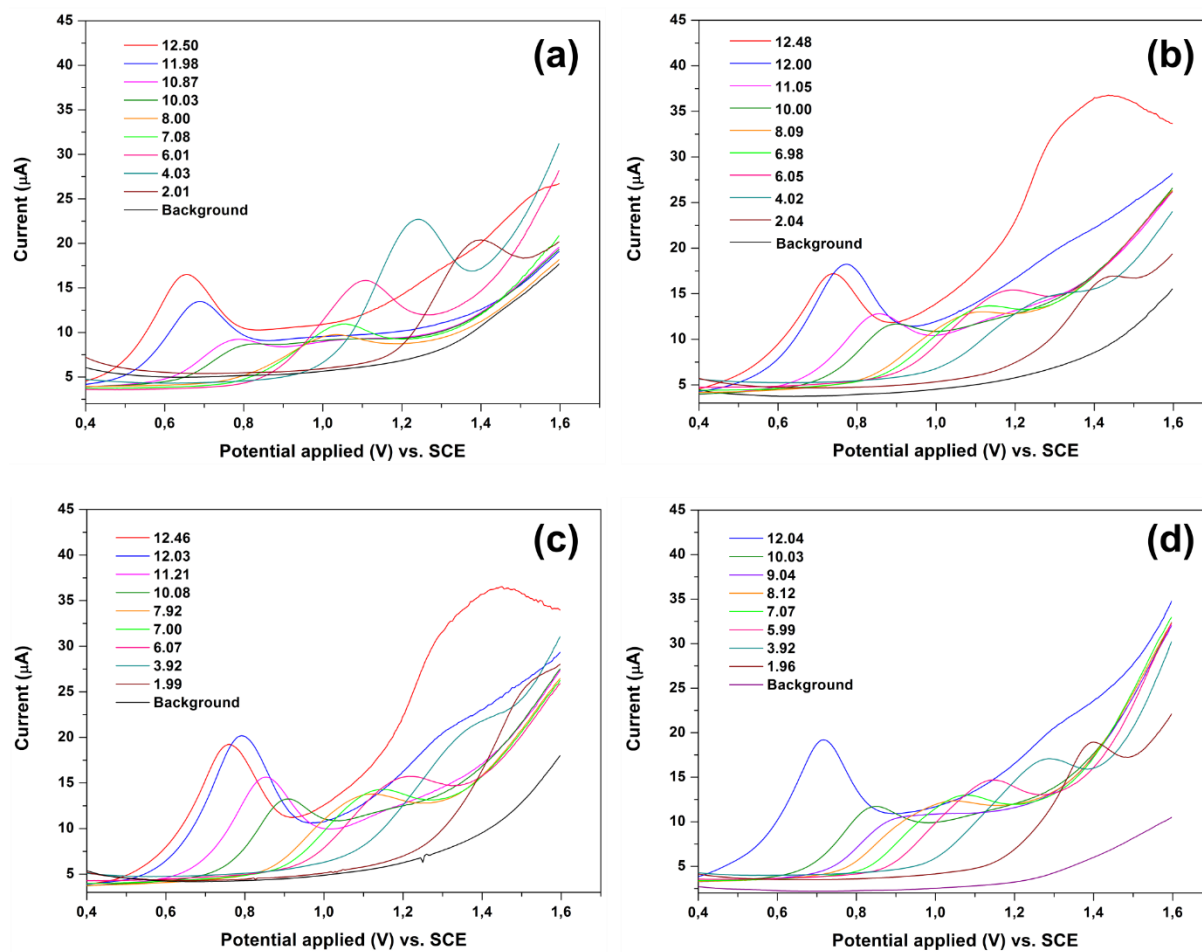


**Figure S2.** DPV of the HimpX ligands at pH 2–12. Electrolyte: 0.04 M Britton–Robinson + 0.1 M  $\text{KNO}_3$ . WE: GCE. RE: SCE. CE: Pt.

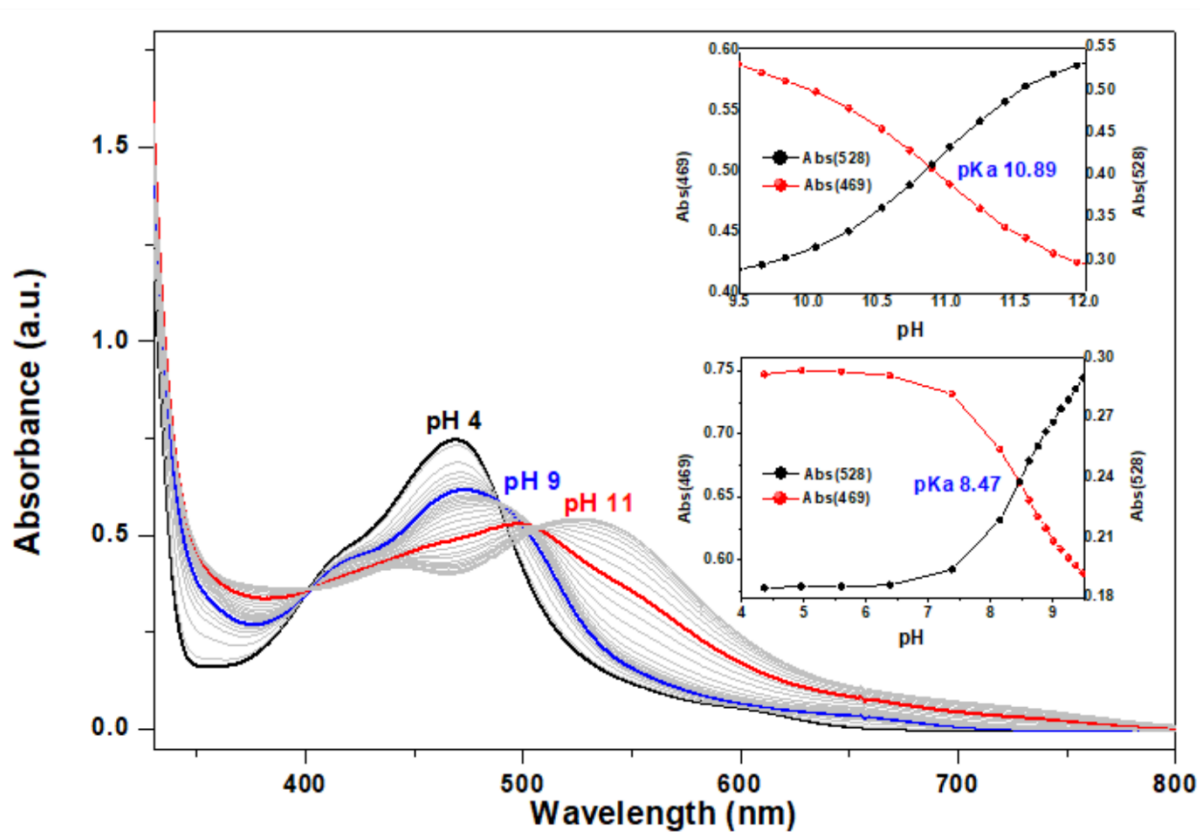


**Figure S3.** Absorption bands changes of  $[\text{Ru}^{\text{II}}(\text{Himpa})(\text{tpy})(\text{OH}_2)]^{2+}$  (160  $\mu\text{M}$ ) in 0.04 M Britton–Robinson buffer after titrating with 4 M NaOH solution in pH range from 4 to 11. Inset: Plot of absorbances at 469 and 528 nm versus pH.

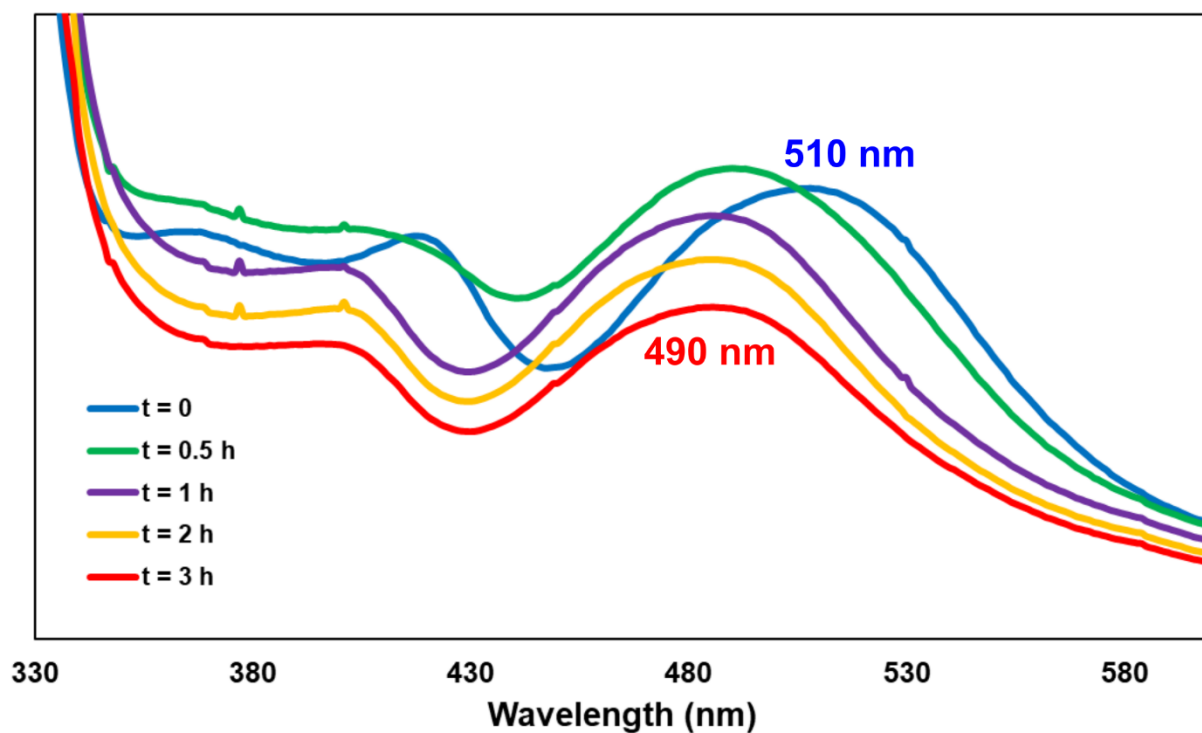


**Figure S4.** Optimizing the reaction time for synthesis of the aqua complex by monitoring the increasing ratio of the chlorido/aqua complexes absorption bands (510 nm/490 nm) in ethanol (to avoid misleading assignment of chlorido absorption band if dissolved in water). The ratio remained constant after 3 h of reaction, indicating the reaction was completed.

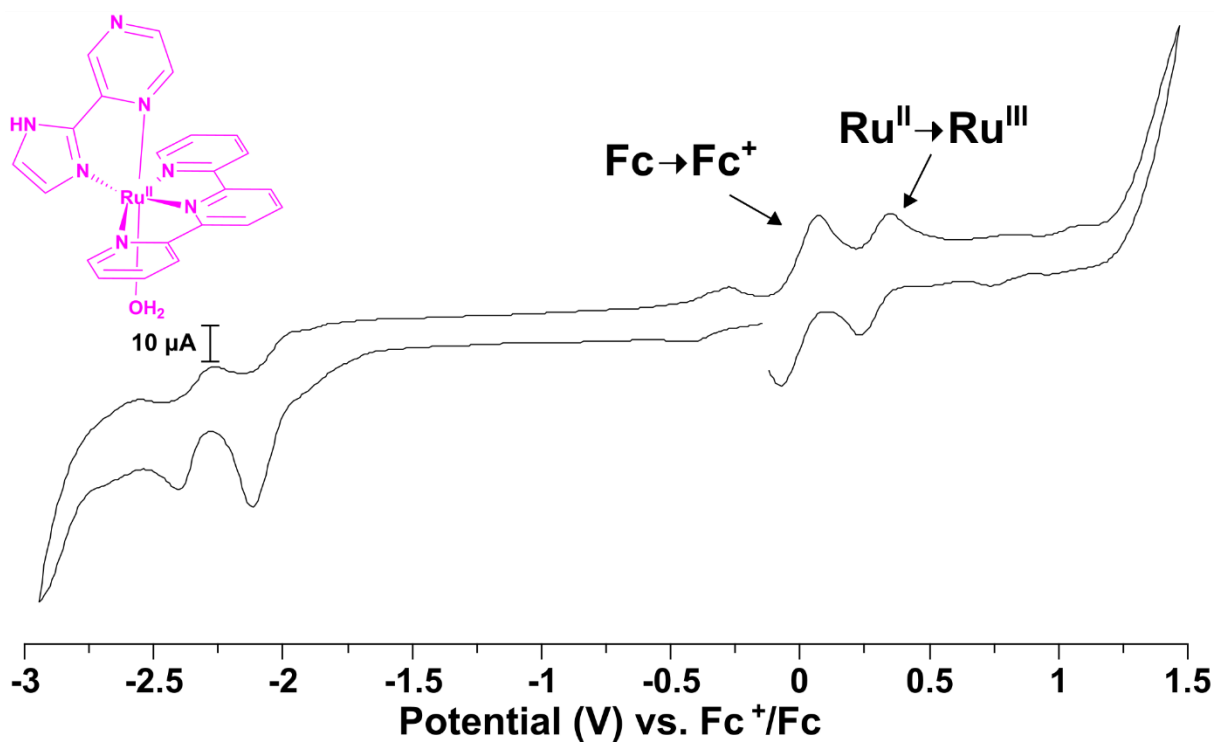


**Figure S5.** Cyclic voltammetry of  $[\text{Ru}(\text{Cl})(\text{Himpz})(\text{tpy})]^+$  recorded in acetonitrile containing 0.1 M  $\text{TBAPF}_6$  under  $\text{N}_2$ . Scan rate:  $0.1 \text{ V s}^{-1}$ . WE: Glassy carbon electrode; RE:  $\text{AgCl}/\text{Ag}$ ; CE: Pt wire. The potentials were referenced against  $\text{Fc}^+/\text{Fc}$  couple and obtained by performing the cyclic voltammetry versus reference electrode  $\text{AgCl}/\text{Ag}$  along with the  $\text{Fc}^+/\text{Fc}$  couple in solution and then subtracting the potential range from the  $\text{Fc}^+/\text{Fc}$  potential. The negative potentials region (-2 – -3 V) contains the reduction events for ligands of the complex.